

Essays on Time Series Analysis in the Context of Climate Change

Von der Wirtschaftswissenschaftlichen Fakultät der
Gottfried Wilhelm Leibniz Universität Hannover
zur Erlangung des akademischen Grades

Doktorin der Wirtschaftswissenschaften
— Doctor rerum politicarum —

genehmigte Dissertation

von

M.Sc. Teresa Flock

geboren am 08.09.1993 in Merzig

2023

Referent: Prof. Dr. Philipp Sibbertsen, Leibniz Universität Hannover

Korreferent: Prof. Dr. Arndt Reichert, Leibniz Universität Hannover

Tag der Promotion: 10.10.2023

Acknowledgments

This thesis and the completion of my PhD would not have been possible without the contribution and support of several persons. First of all, I would like to thank my supervisor and co-author Prof. Dr. Philipp Sibbertsen for the opportunity to earn my PhD degree at his chair, for his support and advice over the last five years (and before), and for many unforgettable moments at the Institute of Statistics. Further, I would like to thank Prof. Dr. Arndt Reichert for taking his time to be my second examiner, Prof. Dr. Marina Schröder for chairing my examination board, as well as Dr. Ute Lohse for advising.

I am also grateful to my other co-authors Dr. Philip Bertram, Dr. Pushpa Dissanayake, Dr. Markus Fritsch, Prof. Dr. Harry Haupt, Dr. Jun Ma, Dr. Johanna Meier, and Dr. Joachim Schnurbus, for sharing their time, experience, and fruitful ideas with me.

A special thanks goes to all my former colleagues at the Institute of Statistics, who created a working environment that was both productive and adequately distracting, and in particular to Dr. Michelle Voges, Dr. Tetie Kolaiti, Vivien Less, and Dr. Johanna Meier, who have become true friends and were always there to help me carry the heavy PhD weight on my shoulders.

Finally, I would like to thank my family and friends for their constant patience and encouragement during my studies, and especially Leon for being the best companion I could ever have imagined.

Abstract

This dissertation contains four essays on applied time series problems. Chapter 1 positions each of the essays in the broader context of climate change and introduces their main objectives and findings.

Chapter 2 deals with the clustering of extremes in oceanographic time series of significant wave heights in late 2013. While established extreme value methods are limited to independent and identically distributed observations, these data are characterized by both short- and long-range dependencies. In a two-step procedure, the dependencies are accounted for by means of an autoregressive fractionally integrated moving average process, which is followed by the application of the peaks-over-threshold approach to the approximately independent residuals. A comparison with two alternative methods for modeling extremal clustering highlights the benefits of jointly incorporating short- and long-range dependence.

Chapter 3 addresses the persistence of precipitation time series, which is subject to considerable estimation uncertainty and variability over time, climatological factors, and geographic locations. For monthly precipitation anomaly series of the United States from 1990 to 2019, a strategy for estimating their memory parameters is proposed which takes potential low-frequency contaminations and short-range ARMA noise into consideration. The variations in the estimated memory parameters are explained in a nonparametric regression that contains both spatial and climatological characteristics and binary indicators for the sources of uncertainty in the memory estimation.

In Chapter 4, the dynamics of the German energy mix and its transition towards renewable energies are analyzed. Focusing on daily power generation from its twelve energy sources and power consumption in the time period from 2016 to 2022, a detrending scheme is introduced that captures the particular seasonal patterns, long-term trends, and weekday and holiday effects of the German energy market. Building upon the detrended time series and based on semiparametric estimation together with a strategy for optimal bandwidth selection, memory parameter estimates are provided. Complemented by a correlation analysis of the detrended and fractionally differenced series, the results are linked to the roles of the renewable power sources within the energy mix.

Chapter 5 is concerned with modeling monthly real exchange rates of 17 countries from 1973 to 2019 and their relation to macroeconomic indicators. A new Markov-STAR model is introduced, which combines the Markov switching models that allow for a shifting

equilibrium rate, and the smooth transition autoregressive models that capture a nonlinear adjustment process towards that equilibrium. Together with a specification procedure for discriminating between the combined model and the individual approaches, the switching equilibrium rates and volatilities are then related to a set of macroeconomic indicators, allowing to draw conclusions on their effect on the likelihood of currency depreciation.

Keywords: Climate Econometrics · Extremal Clustering · Local Whittle Estimation · Long-Range Dependence · Nonlinear Time Series · Seasonality · Spatio-Temporal Heterogeneity · Spurious Long Memory

Contents

List of Figures	V
List of Tables	VI
1 Introduction	1
2 Modeling Short- and Long-Term Dependencies of Clustered High-Threshold Exceedances in Significant Wave Heights	6
3 Changes in US Precipitation, its Memory, and Climatological Heterogeneity	
3.1 Introduction	7
3.2 Precipitation anomalies	9
3.3 Methodology	12
3.3.1 Characterization of the memory properties of time series and long-range dependence	12
3.3.2 Identification and estimation of memory parameters and testing for spurious long memory	14
3.3.3 The variation in precipitation memory	17
3.4 Results	20
3.4.1 Identification, estimation, and inference of precipitation memory parameters	20
3.4.2 The variation in precipitation memory	23
3.5 Discussion	24
3.A Appendix	27
3.A1 Data and software	27
3.A2 Test statistics of the sup-Wald tests for level shifts	32
3.A3 Robustness checks for other regions and worldwide precipitation series	33
4 Germany's Transition Towards Renewable Energies – Empirical Evidence from a Time Series Perspective	
4.1 Introduction	38
4.2 Data description and pre-processing	41
4.3 Seasonal effects	43
4.3.1 Detrending procedure	44
4.3.2 Temporal patterns and trends	45
4.4 Fractional integration	48
4.4.1 Local Whittle estimation under optimal bandwidth selection	49
4.4.2 Memory estimates for the energy mix	51
4.4.3 Spurious long memory and ARMA noise	53

4.4.4 Implications of the memory estimates	55
4.5 Interdependencies and a multivariate perspective	57
4.6 Conclusion	59
4.A Appendix	61
5 Real Exchange Rates and Fundamentals in a New Markov-STAR Model	66
References	67

List of Figures

3.1	Median total monthly precipitation across all monitoring stations in contiguous United States from January 1960 to December 2019.	10
3.2	Top: Monitoring stations in contiguous United States and Köppen climate zones. Bottom: Precipitation anomalies.	11
3.3	Violin plots. Right part: Empirical densities of precipitation anomalies for evaluation period. Left part: Analogous densities for reference period.	12
3.4	Frequency histograms of conventional memory estimates and adjusted memory estimates for monthly precipitation anomaly series from contiguous United States 1990 to 2019.	21
3.5	Scatter plot of conventional memory estimates versus adjusted memory estimates for monthly precipitation anomaly series from contiguous United States 1990 to 2019.	22
3.6	Conventional memory estimates and adjusted memory estimates.	22
3.7	Climate zones according to Köppen classified into main climate zone, seasonal precipitation subgroup, and temperature subgroup, with locations of available monthly precipitation anomaly series.	28
3.8	Precipitation anomalies for evaluation period as median over monitoring stations in contiguous United States for main climate zones B, C, and D, respectively, separately for months January to June.	30
3.9	Precipitation anomalies for evaluation period as median over monitoring stations in contiguous United States for main climate zones B, C, and D, respectively, separately for months July to December.	31
3.10	Frequency histograms of estimated conventional memory estimates and adjusted memory estimates for 2,118 global monthly precipitation anomaly series from 1990 to 2019.	34
3.11	Scatter plot of estimated conventional memory estimates versus adjusted memory estimates for 2,118 global monthly precipitation anomaly series from 1990 to 2019.	35
4.1	Circular plots for the development of power generation and consumption over time, before detrending (pre-processed and standardized series).	43
4.2	Circular plots for the development of power generation and consumption over time, after detrending.	45
4.3	Estimated linear and cyclical components from the detrending regression.	46
4.4	Heat map of the estimated weekday and holiday coefficients from the detrending regression.	47
4.5	Local Whittle estimation for different bandwidths.	51
4.6	MSE-optimal local Whittle estimates for different resampling widths according to the bandwidth selection strategy by Arteche and Orbe (2017)	52
4.7	Bootstrap MSE of the bandwidth selection strategy by Arteche and Orbe (2017) depending on the bandwidth and resampling width.	53
4.8	Correlation coefficients for the detrended and fractionally differenced series.	58
4.9	Composition of the German energy mix in 2016 and 2022.	61
4.10	Correlation coefficients for the pre-processed series.	61
4.11	Power consumption and generation time series after pre-processing.	62
4.12	Power consumption and generation time series after detrending.	63

List of Tables

3.1	Characterization of memory property of time series into anti-persistent, short memory, and long memory and corresponding ranges of values for Hurst coefficient H , fractal dimension F , and degree of fractional differencing d	13
3.2	Absolute and relative frequencies of binary variables \mathbf{X}_B for monthly precipitation anomaly series from contiguous United States 1990 to 2019.	20
3.3	Memory estimates for monthly precipitation anomaly series from contiguous United States 1990 to 2019 supporting different memory behavior.	20
3.4	Five number summary and mean for conventional memory estimates and adjusted memory estimates for monthly precipitation anomaly series from contiguous United States 1990 to 2019.	21
3.5	Estimated bandwidths (for discrete predictors), scale factors (for continuous predictors), and model fit of nonparametric specifications NP1 and NP2.	23
3.6	Köppen climate zones given by three letter classification scheme (main climate zone, seasonal precipitation subgroup, and temperature subgroup) and number of monitoring stations in respective climate zone worldwide and in contiguous United States.	29
3.7	Name, description, type of predictors employed in empirical analysis and descriptive statistics for contiguous United States and Global.	32
3.8	Absolute and relative frequencies of the binary variables \mathbf{X}_B for 2,118 global monthly precipitation anomaly series from 1990 to 2019.	33
3.9	Five number summary and mean for estimated conventional memory estimates and adjusted memory estimates for 2,118 global monthly precipitation anomaly series from 1990 to 2019.	34
3.10	Memory parameter estimates for 2,118 global monthly precipitation anomaly series from 1990 to 2019 falling into three regions that support different memory behavior.	34
3.11	Estimated bandwidths (discrete predictors), scale factors (continuous predictors), and fit of nonparametric regressions NP1 and NP2, for the regions Global, Australia, Europe, and contiguous United States.	36
3.12	Coefficient estimate and standard error (discrete predictors) and effective degrees of freedom and p -value (smooth effect of Longitude and Latitude) for generalized additive models GAM1 and GAM2, for the regions Global, Australia, Europe, and contiguous United States.	37
3.13	p -values of model specification test of Hsiao et al. (2007) based on asymptotic test distribution.	37
4.1	Results of the MSE-optimal bandwidth selection and corresponding local Whittle estimates.	54
4.2	Classification of the power sources according to the estimated memory parameter after MSE-optimal bandwidth selection.	56
4.3	Estimated coefficients for the trend and cycle components in the detrending regression.	64
4.4	Estimated coefficients for the binary weekday and holiday indicators in the detrending regression.	65

CHAPTER 1

Introduction

In the recent decades, time series analysis has proven to be a valuable field of econometrics, allowing to capture complex dynamics and temporal dependencies in various empirical applications. When understanding the underlying processes of time series data, one is able to comprehend historical patterns, identify drivers and trends, characterize seasonal behavior, detect changing structures or anomalies, forecast future development, and thereby support decision-making processes. Besides its wide use in economics, the benefits of time series modeling have been stretched to environmental data and problems linked to climate change. The latter refers to a disruption of known long-term trends and patterns in the environment, such as an accelerated rise of global temperature and sea levels, shifting seasonal cycles and precipitation patterns, and increased frequency and intensity of extreme weather events, causing severe challenges for the human society and global economy (UN, 2023a). In this context, time series techniques allow to investigate different aspects of climate change only by inference from observed data and an approximation of the generating processes rather than depending on the accuracy of a complex global climate model (IPCC, 2013).

While the need for improved or fully new methods never abates when working with empirical data, the field of climate change imposes additional challenges on econometricians, even when not attempting to explain climate phenomena by complex multivariate systems (for overviews on a range of recently introduced models, see e.g. Castle et al., 2020; Hillebrand et al., 2020). From a univariate perspective, for instance, environmental series are often governed by pronounced long-term dependencies that require special statistical attention (amongst many others e.g. highlighted by Tyrallis et al., 2018; Yuan et al., 2019), and their analysis is additionally complicated by underlying seasonal patterns (see e.g. Vanem and Walker, 2013; Gil-Alana, 2017; Proietti and Maddanu, 2022). At the same time, the disruption of environmental circumstances and the associated adaptation of human behavior can cause structural breaks in both climate and economic data (e.g. stressed by Werner et al., 2015; Adedoyin et al., 2020), contradicting the assumptions that are needed for many established methods. In this context, the econometric view on climate change is not limited to environmental data, but also considers its impact on human society and vice versa. This includes quantifying the effects of human actions and governmental measures against climate change and their interplay on a global scale, as

well as assessing the overall economic and financial risks that arise due to the environmental transformation on the one hand, and the transition towards a greener economy on the other (Bonato et al., 2023). Addressing some of the aforementioned aspects, this dissertation consists of four independent essays that provide new perspectives and introduce novel approaches for time series problems that are in the broader sense related to climate change.

In Chapter 2, the well-established peaks-over-threshold (POT) model for extreme values is connected to time series with strong dependencies over distant observations. In its original form, the POT method was introduced by Pickands (1975) to describe the occurrence of extreme observations, i.e. observations above some high threshold u , within independent and identically distributed (iid) data. As time series are usually characterized by temporal dependencies, the iid assumption is easily violated due to short- or long-range dependence, causing a clustering of extremes. Both of these forms of dependencies are present in the considered oceanographic time series of significant wave heights measured on the Sefton coast, UK. As pointed out e.g. by Dissanayake et al. (2015), having a suitable model for this type of data is highly relevant for long-term coastal management. Being constantly aggravated by climate change, the increasing frequency and intensity of storm events and the associated coastal erosion impose difficult challenges to both the coastal societies and landscapes (Nicholls et al., 2007). Moreover, as climate change involves a general rise in weather and climate extremes (IPCC, 2023), expanding the range of suitable extreme value methods to dependent time series data is highly relevant for climate econometrics. The proposed two-step ARFIMA-POT approach contributes to an effective management of the risks inherent to extreme events in environmental data by addressing the clustering of extremes under short and long memory. In a first step, the short- and long-range dependencies are captured by the commonly used ARFIMA model (Granger and Joyeux, 1980; Hosking, 1981), which combines autoregressive and moving average short-range components with fractional integration (or so-called “long memory”). In a second step, the POT approach is applied to the approximately iid residuals, where the occurrence of extremes can be described by a homogeneous Poisson process, while their magnitude is modeled by the generalised Pareto distribution. For comparison, the improved performance of the proposed method over two alternative approaches is documented for modeling of the wave height data: the conditional POT of Chavez-Demoulin et al. (2005) and McNeil et al. (2015) for short-range dependence, and the continuous time random exceedance model of Hees et al. (2021) for long-range dependence.

Chapter 3 addresses the persistence characteristics of precipitation time series. While long-range dependence is generally accepted as a stylized fact of precipitation, it is subject to considerable estimation uncertainty and variability over time, climatological fac-

tors, and geographic locations. However, having reliable estimates for the persistence of precipitation is relevant for comprehending the intensity and frequency of global rainfall patterns, and detecting deviations caused by climate change. Even under a stable total volume, it is known that climate change causes a global reallocation of precipitation through an increasing occurrence of both heavy rainfall and droughts (Dore, 2005), which endangers food and water security around the world (IPCC, 2023). Hence, contributing to the understanding of the persistence of rainfall, monthly precipitation series recorded for the contiguous United States in the time period of 1990 to 2019 are analyzed. The distinct seasonal characteristics of each of the 1,077 monitoring stations are accounted for by considering precipitation anomalies in the form of deviations from the corresponding median precipitation of a reference period from 1960 to 1989. For these anomaly series, a thorough univariate analysis of their memory properties is performed, while accounting for uncertainties regarding the underlying data-generating processes. More precisely, starting from the well-established semiparametric local Whittle estimator for the memory parameter d (Künsch, 1987), the possibilities of so-called spurious long memory and of short-range ARMA noise components are evaluated. Spurious long memory can, for instance, be caused by level shifts, and creates the false impression of significant dependencies over distant observations, which requires a modified estimation technique such as the one proposed by Hou and Perron (2014). Short-range noise components can further bias the semiparametric estimation and call for an adjustment of the user-chosen bandwidth that is needed for both estimators. In a second step, the resulting corrected estimates d^* are evaluated in a suitable nonparametric regression (Racine and Li, 2004) on two predictor sets: first, consisting of spatial and climatological characteristics such as geographic coordinates and climate zone, and second, additionally containing binary indicators for the sources of uncertainty in the memory estimation. It is shown that both sets of variables contribute to explaining the variability of memory parameters and the discrepancies found in previous literature, which is confirmed in a robustness check based on global precipitation data and two other nonparametric regression approaches.

Moving away from environmental data towards the societal and economic implications of climate change, Chapter 4 analyzes the dynamics of the German energy mix. In Germany, energy supply alone accounts for one third of the greenhouse gas emissions, which are the main cause of climate change (UBA, 2023b). Hence, along with international endeavors to substantially reduce greenhouse gas emissions, the German “Erneuerbare-Energien-Gesetz” statutorily determines the gradual replacement of conventional power sources with renewable energies that are based on non-depletable natural sources and involve substantially lower emissions (Bundesregierung, 2022). Yet, designing a system of renewable energies that provides the same capacity, reliability, and controllability as the

current energy mix is complicated by the particular characteristics of the main renewable sources, i.e. wind and solar energy, as they depend on volatile weather determinants. Understanding the interplay and substitution possibilities of the available renewable energy sources is therefore essential for securing Germany's energy future. To shed light on the univariate dynamics and interdependencies of the German energy mix, daily time series of the power generation from its twelve energy sources and power consumption in the time period from 2016 to 2022 are analyzed. By means of a detrending scheme that is specifically tailored to the German energy market, the particular seasonal patterns, long-term trends, and weekday and holiday effects are captured and interpreted. Then, as these series feature long memory, their degree of long-range dependence is estimated via the local Whittle estimator as described above, in combination with a bandwidth selection procedure proposed by [Arteche and Orbe \(2017\)](#) to minimize the estimation uncertainty, while accounting for possible bias from structural breaks or short-range ARMA noise components. The resulting memory parameter estimates allow to divide the twelve energy sources into three groups that reflect their stability and role within the German energy mix. In a first step towards a multivariate setting, it is further discovered that the detrended and fractionally differenced power generation series from the intermittent sources are negatively correlated with the other series, which highlights their unique role in replacing the conventional energies.

Finally, Chapter 5 is concerned with modeling real exchange rates and their relation to macroeconomic indicators. Exchange rates are indirectly linked to the topic of climate change through the global nature of both the associated environmental challenges and the necessary counteractions. Exchange rate data is required whenever currencies need to be translated in a global setting, whether for comparing economic measures like the gross domestic product across nations ([Manne et al., 2005](#)), or for reaching financial agreements on international investments into environmental protection and restitution. At the same time, exchange rates are affected by the increasing possibility of rare but extreme climate disasters, leading to a general depreciation and larger fluctuations ([Farhi and Gabaix, 2016](#); [Bonato et al., 2023](#)). Being able to explain the main characteristics of exchange rate series with help of a suitable time series model does therefore contribute to understanding the economic implications of climate change. In this chapter, a new Markov-STAR model is introduced, which combines two major branches of the literature on exchange rates: the Markov switching models that allow for a shifting equilibrium rate ([Engel and Hamilton, 1990](#); [Bergman and Hansson, 2005](#)), and the smooth transition autoregressive (STAR) models that capture a nonlinear adjustment process towards that equilibrium ([Teräsvirta, 1994](#); [van Dijk et al., 2002](#)). From a statistical perspective, an exponential transition function smoothly blends an inner unit root regime with a white noise process to correct

strong deviations from the equilibrium, while its switching mean and innovation variance are defined by a latent variable that follows a Markov chain. Together with a specification procedure for discriminating between the combined model and the individual approaches (based on [Distaso, 2008](#)), the model is applied to real exchange rates of 17 countries, and the estimated equilibrium regime series are explained by different macroeconomic indicators (i.e. output gap differential, inflation differential, and economic uncertainty), which allows to draw conclusions on the likelihood of currency depreciation. While the model was initially proposed for exchange rate data, it could prove equally useful for data sets directly related to climate change. For example, [Gil-Alana et al. \(2017\)](#) found evidence for concurrent nonlinear mean-reversion and level shifts in carbon dioxide emissions from several countries. Furthermore, the need for considering the respective counterpart in applications of either Markov switching or STAR models on environmental series (e.g. [Ailliot and Monbet, 2012](#); [Ubilava and Helmers, 2013](#)) could be re-examined.

CHAPTER 2

Modeling Short- and Long-Term Dependencies of Clustered High-Threshold Exceedances in Significant Wave Heights

*Co-authored with Pushpa Dissanayake, Johanna Meier, and Philipp Sibbertsen.
Published in Mathematics (2021), 9(21), 2817.*

<https://doi.org/10.3390/math9212817>

CHAPTER 3

Changes in US Precipitation, its Memory, and Climatological Heterogeneity

Co-authored with Markus Fritsch, Harry Haupt, Joachim Schnurbus, and Philipp Sibbertsen.

3.1 Introduction

A prominent research question in hydrology originated from modeling river-runoff to support engineering practice in the design of dams and reservoirs for regulating river flows, water storage, and flood protection (Hurst, 1956; Eagleson, 1994; Sutcliffe et al., 2016; O’Connell et al., 2016). As a natural source of river-runoff (Potter, 1979) and due to its wide economic and agricultural implications (Kotz et al., 2022), developing modeling frameworks for precipitation series (for early work, see Hurst, 1957; Le Cam, 1961; Mandelbrot and Wallis, 1968) and short-term forecasting of such series and related extreme events (for recent work, see Sansó and Guenni, 2000; Berrocal et al., 2008; Kleiber et al., 2011; Bertolacci et al., 2019; Liu et al., 2019; Schlosser et al., 2019; Bacro et al., 2020; Bopp et al., 2021; Dupuis and Trapin, 2023; Richards et al., 2022) received considerable attention in the literature. While river flow and precipitation modeling has traditionally focused on small geographic areas and short-term dynamics (Eagleson, 1994), recent research on precipitation series has expanded to a global scale to examine the effects of climate change and its attribution to anthropogenic influences and/or natural phenomena (Zhang et al., 2007; Büntgen et al., 2011; Bindoff et al., 2013; O’Connell et al., 2022). Closely related issues are the relationship between precipitation and temperature (Liu et al., 2009; Allan et al., 2014), the variability of precipitation in different climates (Zhang et al., 2007; Bhend and von Storch, 2008; Tapiador, 2010; Polson et al., 2013) or the different characteristics of precipitation series at different time scales and/or geographic locations (Rocheta et al., 2014; Gehne et al., 2016; Adler et al., 2017; Tyrallis et al., 2018), and changes in the spatial distribution over time (for a review, see Dore, 2005).

Recent reports from the Intergovernmental Panel on Climate Change (IPCC) highlight substantial changes in global precipitation patterns and future projections. Globally, the variability of precipitation and the underlying uncertainty are projected to increase in the

mid 21st century – continuing the trends observed in several regions like the northern high latitudes and tropical land areas. Locally, increases in mean precipitation are projected for Asia and the Polar and Terrestrial regions, decreases for Africa and Australia, and region-specific changes for Europe and North-, Central-, and South America. With respect to heavy precipitation and aridity, increases are projected across almost all regions of the world which increases the likelihood of pluvial flooding and dry spells and creates important challenges for ecosystems, human society, and water management (IPCC, 2021, 2023). More detailed analyses at a finer resolution are provided by national agencies such as the United States Environmental Protection Agency (EPA, 2022), where changes in past rainfall patterns are documented for the contiguous United States and Alaska.

All of the aforementioned research questions and projections of climatic conditions require a deep understanding of the underlying data-generating processes and there have been vigorous debates about the memory properties of precipitation in the past (for details, see Graves et al., 2017), particularly its long-range dependence. This phenomenon, also referred to as long memory, long-term persistence, Hurst-Kolmogorov behavior, or Hurst effect (e.g., Markonis and Koutsoyiannis, 2016; O’Connell et al., 2016; Graves et al., 2017), effectively describes the decay of the autocorrelation function. A slow decay leads to high correlations over long lags, and the process is regarded to exhibit long-range dependence (Koutsoyiannis, 2003). Numerous empirical studies have investigated the properties of precipitation for different regions and on different time scales. Overall, the reported memory characteristics show considerable heterogeneity (e.g., Potter, 1979; Breslin and Belward, 1999; Longobardi and Villani, 2010; Efstathiou and Varotsos, 2012; Anghileri et al., 2014; Yaya et al., 2015; Gil-Alana et al., 2019; Paul et al., 2019; Gil-Alana et al., 2022) supporting short memory in some cases (e.g., Rao and Bhattacharya, 1999), while providing evidence for long-range dependence in others (e.g., Gil-Alana, 2012; Efstathiou and Varotsos, 2012; Fatichi et al., 2012; Yaya et al., 2015; Illiopoulou et al., 2018). This inconsistent empirical evidence from studies of the memory properties of precipitation is often attributed to a lack of long-term records, sparse spatial monitoring, and the use of different algorithms, time intervals, regions, and data pre-processing strategies (e.g., Bunde et al., 2013; O’Connell et al., 2016; Graves et al., 2017; Sun et al., 2018; Tyralis et al., 2018; Gil-Alana et al., 2022). Not surprisingly, some authors have suggested that the statistical methodology used to test these various forms of short precipitation records has sometimes been over-interpreted (e.g., Cohn and Lins, 2005; Markonis and Koutsoyiannis, 2016; Serinaldi et al., 2018).

Early concerns on this matter were voiced by Klemeš (1974) for applied hydrology, and it is now well established in time series analysis of hydrological processes (e.g., Koutsoyiannis, 2000; Diebold and Inoue, 2001; Beran and Feng, 2002; Cohn and Lins, 2005) that different insights into the memory properties may be due to spatio-temporal heterogeneity driven by level shifts, (temporary) trends, seasonality, and dry spells. We propose a care-

ful strategy for identifying and estimating memory parameters of precipitation processes that tests for the presence of these drivers. From the resulting testing and estimation procedure, based on recent advances in the statistical literature on long-memory processes, we obtain memory estimates for all regions considered and corresponding indicator variables as proxies for the drivers of spatio-temporal heterogeneity in precipitation processes. For the monthly precipitation anomalies observed in the contiguous United States from January 1960 to December 2019 at 1,077 monitoring stations, we find that precipitation patterns not only change substantially in this time span, but also that there is considerable spatial and climatologic heterogeneity underlying the memory parameters. The estimated parameters support a wide range of interpretations from long-range dependence to short-run dynamics and anti-persistent structures. In particular, the results illustrate the merits of the proposed approach by emphasizing that estimators should be chosen judiciously and encompassed in a test strategy. We show that the observed variation in the resulting memory estimates nonlinearly depends on climatological and geographic variables after controlling for the indicators derived from our diagnostic tests. Similar results hold in our complementary analysis for other large regions with different climatological patterns around the world.

The remainder of this paper is structured as follows. Section 3.2 introduces precipitation anomalies and highlights stylized facts of the data. Section 3.3 proposes a basic model which incorporates various forms of (long-range) dependence and details the steps for characterizing the memory properties of precipitation anomalies in the presence of seasonality, spatial heterogeneity, and spurious long memory. Section 3.4 summarizes the identification of the memory parameters and their properties for the contiguous United States. Section 3.5 discusses the strengths, weaknesses, and potential extensions of the proposed approach in context with related literature and concludes.

3.2 Precipitation anomalies

Figure 3.1 shows a season plot of the median total monthly precipitation (in millimeters) from January 1960 to December 2019. The blue lines represent the monthly medians over 1,077 permanent monitoring stations in the contiguous United States and the gray lines are corresponding monthly medians over the 30-year reference period from 1960 to 1989; (see, e.g., Zhang et al., 2000, 2007; Sánchez-Murillo et al., 2017). The raw data are precipitation series recorded by the weather monitoring stations of the Global Historical Climatology Network – Daily (GHCN-Daily, Version 3.26) and provided by the National Centers for Environmental Information (Menne et al., 2020). Although Figure 3.1 does not display an actual observed series, it illustrates the presence of pronounced seasonality (in levels and variation). Differences in the levels of total precipitation throughout the

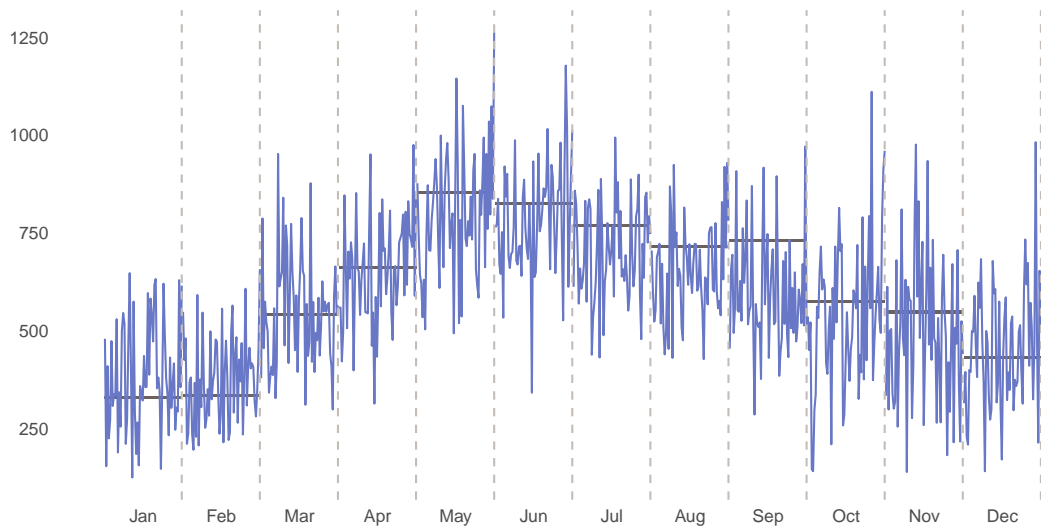


Figure 3.1: Median total monthly precipitation (in millimeters) across all monitoring stations in contiguous United States from January 1960 to December 2019. Horizontal lines represent median total monthly precipitation for reference period 1960 to 1989.

annual cycle have been documented frequently (see, e.g., Haan et al., 1976; Buishand, 1978; Efstathiou and Varotsos, 2012; Yaya et al., 2015) and are a key stylized fact of precipitation series.

In the following, we investigate precipitation anomalies of monthly frequency $A_{t,i}$ computed for each monitoring station i . The anomalies are obtained for the 30 years from 1990 to 2019 (evaluation period) by adjusting for seasonal variations by taking the differences of the total precipitation $R_{y:m,i}$ in year y and month m and the median precipitation over the 30 years from 1960 to 1989 (reference period),

$$A_{y:m,i} = R_{y:m,i} - \tilde{R}_{\bullet:m,i}, \quad (3.1)$$

where $\tilde{R}_{\bullet:m,i} := \text{med}(R_{1960:m,i}, \dots, R_{1989:m,i})$. We consider the median to appropriately capture the central tendency of the empirical distribution of monthly precipitation due to the (rare) occurrence of heavy precipitation. Figure 3.2 provides two maps of the contiguous United States. The top display illustrates the locations of monitoring stations for which precipitation series were available from January 1960 to December 2019 and is colored according to the Köppen climate zones of the respective areas. The map shows that the stations are located in the main climate zones B, C, and D. In the bottom display, the locations of the stations are colored according to the median precipitation anomalies over the 30 years from 1990 to 2019 (evaluation period)

$$\tilde{A}_{\bullet:\bullet,i} := \text{med}(A_{1990:1,i}, \dots, A_{2019:12,i}). \quad (3.2)$$

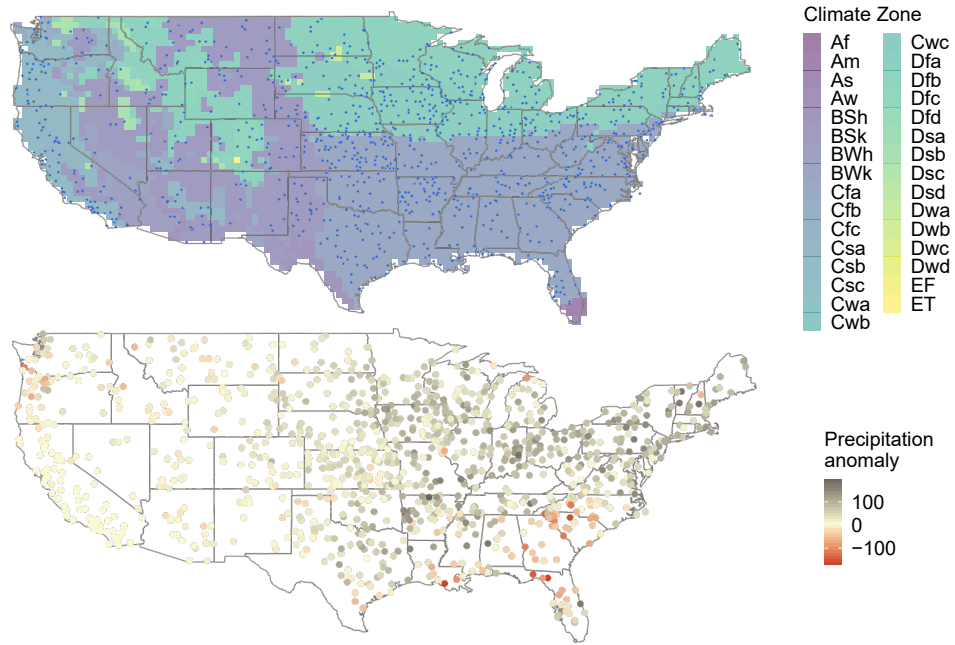


Figure 3.2: Top: Monitoring stations in contiguous United States and Köppen climate zones. Bottom: Precipitation anomalies $\tilde{A}_{\bullet, \bullet, i}$ calculated according to (3.1) and (3.2).

We observe positive median anomalies mostly in the Mid-Atlantic region and eastern parts of the South West and the Mid-West – while for the North-West and parts of the South East, the median anomalies tend to be negative or close to zero. This mirrors trends documented for mean precipitation anomalies by the United States Environmental Protection Agency (EPA, 2022) and the recent IPCC reports (IPCC, 2021, 2023).

Figure 3.3 displays the empirical densities of monthly median precipitation anomalies over the evaluation period 1990 to 2019 and stations separately for all months (right part of violin plots),

$$\tilde{A}_{\bullet, m, \bullet} = \text{med}(A_{\bullet, m, 1}, \dots, A_{\bullet, m, 1077}), \quad (3.3)$$

and analogously for the reference period 1960 to 1989 (left part of violin plots). While the median anomalies from 1990 to 2019 exceeded the medians of the reference period for all months but September and November, we observe an increased spread of the empirical distribution, as the interdecile and interquartile ranges increase from 1990 to 2019 compared to the reference period for all months but November. Further, for both considered time periods, the empirical distribution of anomalies tends to be right skewed across all months. Finally, as the differences between the means and medians increased for all months – except March, September, and November – the skewness of the empirical distribution of the anomalies increased in the evaluation period compared to the reference period. In the following, we use $A_{t, i}$ to denote the precipitation anomalies, where t is a time index.

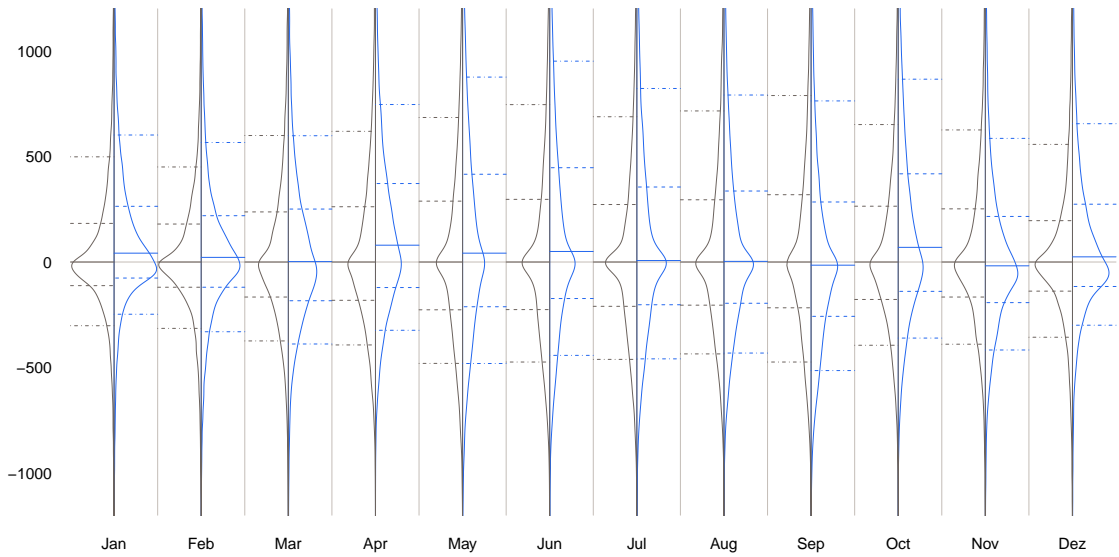


Figure 3.3: Right part of violin plots shows empirical densities of precipitation anomalies $\tilde{A}_{\bullet,m,\bullet}$ calculated according to (3.1) and (3.3) for evaluation period, left part shows analogous densities for reference period. Solid lines indicate median; dashed (dotted) lines are empirical 25%- and 75%-quantiles (10%- and 90%-deciles).

3.3 Methodology

We propose a basic model for the characterization of the memory properties of precipitation anomalies. First, commonly employed statistics are used to distinguish long memory, short memory, and anti-persistent behavior. Second, methods for identifying, estimating, and testing for spurious long memory are introduced. Then, an approach based on distribution-free regression is developed to investigate the variation in the memory properties.

3.3.1 Characterization of the memory properties of time series and long-range dependence

The properties of precipitation series are often characterized by the Hurst coefficient, the fractal dimension, and the degree of fractal differencing. Those parameters are intimately connected and we start by clarifying their relationship and interpretation. The Hurst coefficient H indicates a fractional Brownian motion (fBM) – a generalization of an ordinary Brownian motion. A key property of fBM is, that considering the process on a different time-scale results in an identical finite dimensional distribution after suitable re-scaling (Graves et al., 2017). The fractal dimension F , which can be estimated based on empiri-

cal data by box-counting, re-scaled range analysis, and the variation method (Breslin and Belward, 1999), is defined as

$$F = 2 - H. \quad (3.4)$$

Here and subsequently, we drop the subscript i and define long-range dependence as follows. A process $\{A_t\}_{t \geq 1}$ is stationary fractionally integrated of type I, if fractional differencing of degree d , where

$$d = H - 0.5, \quad (3.5)$$

leads to a stationary short-memory sequence

$$(1 - L)^d A_t = V_t \quad (3.6)$$

with continuous and bounded spectrum and infinite past (Marinucci and Robinson, 1999). For $d \in] - 0.5, 0[\cup] 0, 0.5[$, the sequence V_t satisfies

$$\begin{aligned} \gamma(k) &\sim L_\gamma(k) |k|^{2d-1} \quad \text{for } k \rightarrow \infty, \\ L_\gamma(k) &= 2G(k^{-1}) \Gamma(1 - 2d) \sin(\pi d), \end{aligned} \quad (3.7)$$

where $\gamma(k)$ is the autocovariance function evaluated at lag k , and $G(\cdot)$ is a slowly varying function in Zygmund's sense (such that for $k \rightarrow \infty$, the function is well approximated by a constant G). The fractional differencing operator is defined (via Gamma function $\Gamma(\cdot)$) by

$$(1 - L)^d = \sum_{k=0}^{\infty} \pi_k(d) L^k = \sum_{k=0}^{\infty} \frac{\Gamma(k - d)}{\Gamma(-d) \Gamma(k + 1)} L^k. \quad (3.8)$$

Table 3.1 summarizes the characterization of the memory property of a series into anti-persistent, short memory, and long memory by the Hurst coefficient H , fractal dimension F , and degree of fractional differencing d via the corresponding ranges of values.

Table 3.1: Characterization of memory property of time series into anti-persistent, short memory, and long memory and corresponding ranges of values for Hurst coefficient H , fractal dimension F , and degree of fractional differencing d .

Characterization	Hurst coef. H	Fractal dim. F	Degree of frac. diff. d
Anti-persistent	$]0, 0.5[$	$]1.5, 2[$	$] - 0.5, 0[$
Short memory	0.5	1.5	0
Long memory	$]0.5, 1[$	$]1, 1.5[$	$]0, 0.5[$

In the following, we employ the degree of fractional differencing d and refer to d as the memory parameter. Starting from the classical and most widely used local Whittle (LW) estimator for d , we propose to compute at least one additional estimator. We use an encompassing strategy based on statistical tests covering a variety of data generating processes which may differ with respect to their autocovariance functions. In particular, we test for the presence of structural breaks, smooth trends, and short-memory noise components. In all of these cases, the LW estimator can lead to incorrect conclusions. The resulting estimators for d can take four different forms: the LW estimator, the Hou-Perron (HP or modified LW) estimator, and both of these estimators with lower bandwidths when accounting for short-memory noise.

3.3.2 Identification and estimation of memory parameters and testing for spurious long memory

This subsection introduces the local Whittle estimator and its modified version, the Hou-Perron estimator. Additionally, tests and identification strategies for the presence of spurious long memory, mean breaks, and short-run dynamics are summarized.

The classical memory parameter estimator: Local Whittle

As a natural choice for estimating d , the LW estimator (Künsch, 1987) is defined as

$$\widehat{d}_{LW} = \arg \min_d R(d), \quad (3.9)$$

with

$$R(d) = \log \left(\frac{1}{J} \sum_{j=1}^J \frac{I(\lambda_j)}{\lambda_j^{-2d}} \right) + \frac{1}{J} \sum_{j=1}^J \log \lambda_j^{-2d}, \quad (3.10)$$

based on the precipitation anomalies' periodogram $I(\lambda_j) = (2\pi T)^{-1} \left| \sum_{t=1}^T A_t \exp(-it\lambda) \right|^2$ evaluated at the Fourier frequencies $\lambda_j = 2\pi j/T$ for a sample size T , where, $j = 1, \dots, J$. As bandwidth, we choose $J = \lfloor T^{0.7} \rfloor$ unless stated otherwise, where $\lfloor \cdot \rfloor$ returns the integer part of its argument. The estimator \widehat{d}_{LW} has been frequently used for studying the memory in precipitation series (see, e.g., Gil-Alana, 2012; Paul et al., 2019; Gil-Alana et al., 2022). As the following paragraphs suggest, however, \widehat{d}_{LW} may not be the optimal choice in the presence of level shifts, smooth trends, or short-run (ARMA) dynamics.

A modified local Whittle estimator: Hou-Perron

Low-frequency contaminations such as level shifts or smooth trends may falsely indicate long-range dependence. As \widehat{d}_{LW} is based on periodogram ordinates close to the origin, it

can be upward biased when spurious long memory is present. The estimator of [Hou and Perron \(2014\)](#) is a modified local Whittle estimator which includes a second component in the spectral density representing the share of low-frequency contaminations,

$$\widehat{d}_{HP} = \arg \min_{d, \theta} R(d, \theta), \quad (3.11)$$

with

$$R(d, \theta) = \log \left(\frac{1}{J} \sum_{j=1}^J \frac{I(\lambda_j)}{\lambda_j^{-2d} + \theta \lambda_j^{-2}/T} \right) + \frac{1}{J} \sum_{j=1}^J \log \left(\lambda_j^{-2d} + \theta \lambda_j^{-2}/T \right), \quad (3.12)$$

where $\theta \in]0, \infty[$ denotes the signal-to-noise ratio. According to simulation results of [Busch and Sibbertsen \(2018\)](#), the modified \widehat{d}_{HP} is the most reliable semi-parametric estimator in the presence of various types of low-frequency contaminations. To the best of our knowledge, it was not yet used for studying the memory in precipitation series.

Qu's test for spurious long memory

Stationary long-memory processes and series with spurious long memory can be distinguished by the test of [Qu \(2011\)](#). Similar to the estimators for the memory parameters, it is based on periodogram ordinates close to the origin. For the hypotheses

$$H_0 : \text{stationary process with } f(\lambda) \sim G\lambda^{-2d} \text{ as } \lambda \rightarrow 0^+ \text{ vs.}$$

$$H_1 : \text{process contaminated by level shifts or smooth trend,}$$

the test statistic is given by

$$W_{Qu} = \sup_{r \in [\epsilon, 1]} \left(\sum_{j=1}^J v_j^2 \right)^{-\frac{1}{2}} \left| \sum_{j=1}^{\lfloor Jr \rfloor} v_j \left(\frac{I(\lambda_j)}{G(\widehat{d}_{LW}) \lambda_j^{-2\widehat{d}_{LW}}} - 1 \right) \right|, \quad (3.13)$$

with $G(d) = \frac{1}{J} \sum_{j=1}^J \lambda_j^{2d} I(\lambda_j)$, $v_j = \log \lambda_j - \frac{1}{J} \sum_{j=1}^J \log \lambda_j$, and trimming parameter ϵ . In the empirical application we set $\epsilon = 0.05$. If H_0 is not rejected, there is no indication that the process is contaminated, neither by level shifts, nor by a smooth (deterministic) trend.

Pre-whitening of short-run ARMA dynamics

Whenever series exhibit short-run dynamics, the corresponding higher-frequency periodogram ordinates can bias the given memory estimators and Qu's test. Short-run dynamics can be identified using autoregressive and moving average components in an

ARFIMA(p, d, q) model, which is defined according to Granger and Joyeux (1980) and Hosking (1981) as

$$\Phi(L)(1-L)^d A_t = \Theta(L)V_t, \quad (3.14)$$

where $\Phi(z) = 1 - \sum_{h=1}^p \phi_h z^h$ and $\Theta(z) = 1 - \sum_{k=1}^q \theta_k z^k$ denote AR and MA polynomials, and $V_t \sim iid(0, \sigma_V^2)$ are independently and identically distributed innovations. Following recommendations of Qu (2011), we carry out pre-whitening according to (3.14). This involves estimating ARFIMA(p, d, q) models for $p, q \leq 1$ via exact maximum likelihood for all series and selecting one model for each series based on the Akaike information criterion. Whenever the selected model is non-stationary or non-invertible, the corresponding parameters are cut down to lie within the unit circle. The estimated parameters of the selected model are then used to fit the corresponding ARMA(p, q) model and thereof a vector of residuals is obtained for each series. Additionally, we employ a smaller bandwidth $J = \lfloor T^{0.6} \rfloor$ in the memory parameter estimation, whenever AR or MA dynamics are identified during the pre-whitening procedure. Our results for the contiguous United States and global data suggest that pre-whitening and a lower bandwidth should be considered, as roughly one third of the investigated series contained indications for short-run dynamics, which increases the variation of the memory parameter estimates and thus the uncertainty when identifying the memory properties of precipitation.

Sup-Wald tests for mean breaks

Unreported analyses have shown that the test of Qu (2011) reacts to positive skewness of the precipitation anomaly series with a negative bias, resulting in a higher type II error and fewer detections of spurious long memory. Hence, we also test for the presence of level shifts. As some series might feature such low frequency contaminations and true long memory, we use two mean break tests comprising consistent estimation of the long-run variance: The self-normalized sup-Wald test (SNSW) of Shao (2011) and the fixed- b sup-Wald test (FBSW) of Iacone et al. (2014). Both test statistics (see appendix) are reliable under short and long memory (Wenger et al., 2019) and employ a single mean shift model in which the stochastic process $\{A_t\}_{t \geq 1}$ is generated by

$$\begin{aligned} A_t &= \mu_t + \varepsilon_t, \\ \mu_t &= \mu + \beta \mathbb{1}(t \geq t^*), \quad t \geq 0, \end{aligned} \quad (3.15)$$

where the sequence of regression means μ_t is assumed to be deterministic, the coefficient β quantifies the magnitude of the possible mean shift, $\mathbb{1}(t \geq t^*)$ is an indicator function that depends on the break point location $t^* = \lfloor \tau^* T \rfloor$, and $\tau^* \in]0, 1[$ denotes the break fraction. As the error term $\{\varepsilon_t\}_{t \geq 1}$ may be stationary fractionally integrated, both tests

require prior estimation of the memory parameter. We use \widehat{d}_{LW} here, whenever necessary with lower bandwidth $J = \lfloor T^{0.6} \rfloor$ to prevent bias from short-run dynamics, and then test the null hypothesis of a constant unconditional mean against the alternative of a change-in-mean:

$$H_0 : \mu_1 = \dots = \mu_T = \mu \quad \text{vs.}$$

$$H_1 : \mu_t \neq \mu_s \text{ for some } 1 < t, s < T \text{ and } t \neq s.$$

If we cannot reject H_0 , there are no indications for level shifts.

Conventional and adjusted memory parameter estimates

From our previous analysis we have two sets of estimators:

- \widehat{d}_{LW} , the conventional memory parameter estimate.
- \widehat{d}^* , the adjusted memory parameter estimate: For short-run dynamics, the lower bandwidth $J = \lfloor T^{0.6} \rfloor$ is employed. In case of level shifts and smooth trends (if H_0 of Qu's test or one of the two mean break tests is rejected at significance level $\alpha = 10\%$), \widehat{d}_{HP} is used; in all remaining cases \widehat{d}_{LW} is used.

3.3.3 The variation in precipitation memory

In a next step we identify predictors of the variation in the estimated memory parameters. We compute both estimators for all precipitation anomaly series and use them as response in a regression. While [Tyrallis et al. \(2018\)](#) investigate whether the variation in \widehat{d}_{LW} is driven by spatial and climatological heterogeneity summarized by the established predictor set \mathbf{X}_P , we consider the set of binary predictors \mathbf{X}_B , with $\mathbf{X} = (\mathbf{X}_P, \mathbf{X}_B)$ and $P + B = K$:

- \mathbf{X}_P consists of the spatial characteristics Latitude, Longitude, and Altitude (grouped into deciles) as well as the (categorical) variables Main climate zone, Precipitation subgroup, and Temperature subgroup that reflect the Köppen climate zone classification.
- \mathbf{X}_B comprises four binary predictors constructed as follows (cf. Section 3.3.2):
 1. Qu spurious: This binary predictor is assigned a value of one if the null hypothesis of Qu's test is rejected after pre-whitening at the significance level $\alpha = 5\%$.
 2. Mean break: This binary predictor is assigned a value of one, whenever one (both) of the two long-memory-robust mean break tests SNSW and FBSW rejects the null hypothesis of a constant mean at the significance level $\alpha = 5\%$ ($\alpha = 10\%$).
 3. Contaminated: This binary predictor is assigned a value of one, when at least one of the previous tests rejects the null hypothesis at the significance level $\alpha = 10\%$. It indicates series that give no clear evidence on spurious long memory in Qu's sense or on a mean shift, but which might still be contaminated in the lower frequencies.

4. ARMA noise: This binary predictor is assigned a value of one, if any autoregressive ($p > 0$) or moving average components ($q > 0$) are selected within the ARFIMA (p, d, q) estimation. It indicates the presence of short-run dynamics, which induces a bias in the estimation of the memory parameter.

Including the predictor set \mathbf{X}_B addresses one of the shortcomings pointed out in [Tyrallis et al. \(2018\)](#) by reducing the uncertainty underlying the identification (and estimation) of the memory parameters. In their analysis of the spatial and climatological dimensions of precipitation memory, [Tyrallis et al. \(2018\)](#) employ the data-driven “black-box” procedure random forests (RF). While imposing minimal structural assumptions, RF make it difficult to provide interpretations and assess the relevance of predictor (sets) beyond comparing the predictive performance of different specifications, since the large sample properties of RF remain unknown.

Instead of RF, we employ multiple nonparametric (NP) regression for mixed continuous and discrete predictors ([Racine and Li, 2004](#); [Li and Racine, 2007](#)), and also fit generalized additive models (GAM, see [Hastie, 1990](#); [Wood, 2017](#)) as a baseline approach. The two approaches provide model interpretation and inference within the familiar regression framework, while imposing minimal structural assumptions and allow to infer whether spatial and climatological heterogeneity is still relevant after controlling for uncertainty in the identification and estimation of memory parameters. We leverage the advantages of both regression approaches to provide interpretations about the fitted models and test the empirical relevance of the binary predictors \mathbf{X}_B after controlling for \mathbf{X}_P .

We first fit the NP regression

$$Y = f(\mathbf{X}) + U, \quad (3.16)$$

where Y denotes the estimated memory parameter, \mathbf{X} the K predictors, and U is an additive error term. We assume mean independence between precipitation anomalies and the complete set of predictors, meaning that

$$\mathbb{E}(U | \mathbf{X}) = 0 \quad (3.17)$$

holds almost surely (a.s.). We fit regression (3.16) by using the local constant estimator of [Racine and Li \(2004\)](#),

$$\hat{f}(\mathbf{x}, \mathbf{b}) = \frac{1}{n} \sum_{i=1}^n \frac{\prod_{k=1}^K w_k(x_k, x_{i,k}, b_k)}{\frac{1}{n} \sum_{i=1}^n \prod_{k=1}^K w_k(x_k, x_{i,k}, b_k)} \cdot y_i, \quad (3.18)$$

with weighting function $w_k(\cdot)$, which depends on the scale level of the underlying observed predictors x_k and the corresponding smoothing parameters b_k . We estimate $\mathbf{b} = (b_1, \dots, b_K)'$ by least-squares cross-validation via

$$\widehat{\mathbf{b}} = \arg \min_{\mathbf{b}} \sum_{i=1}^n \left(y_i - \widehat{f}_{-i}(\mathbf{x}_{-i}, \mathbf{b}) \right)^2 \cdot M(\mathbf{x}_i),$$

where $\widehat{f}_{-i}(\cdot)$ is the jackknife estimator for observation i and $M(\cdot)$ is a function that controls for boundary issues of the local constant estimation. A benefit of local constant regression with bandwidths estimated by least-squares cross-validation are the insights available from the estimated smoothing parameters $\widehat{\mathbf{b}}$: Large values indicate that the underlying predictors are irrelevant, as it denotes the degree of smoothing and when it approaches one, the respective predictor is smoothed out (Hall et al., 2007). A common drawback of nonparametric approaches is the “curse of dimensionality”. However, \mathbf{X}_P contains only two continuous predictors and the number of discrete predictors in $\mathbf{X}_P, \mathbf{X}_B$ has no effect on the rate of convergence (for details, see Racine and Li, 2004; Li and Racine, 2007).

Based on the local constant estimator, it can be tested if one or more predictors have a non-zero effect on the response for discrete (Racine et al., 2006) and continuous predictors (Racine, 1997). For our purpose, this involves testing the hypotheses

$$H_0 : \mathbb{E}(Y | \mathbf{X}_P, \mathbf{X}_B) = \mathbb{E}(Y | \mathbf{X}_P) \text{ a.s., vs.}$$

$$H_1 : \mathbb{E}(Y | \mathbf{X}_P, \mathbf{X}_B) \neq \mathbb{E}(Y | \mathbf{X}_P) \text{ on a set with positive probability.}$$

If we cannot reject H_0 , there are no indications that any of the four predictors in \mathbf{X}_B has an effect on the response and the variables are not suitable for explaining the variation of the memory parameters.

As a second modeling approach, we fit a GAM, where $f(\mathbf{X})$ in (3.16) is decomposed into additively linked functionals, some of which depend on a finite dimensional set of parameters β_0 . Then, we consider $Y = g(\mathbf{X}; \beta_0) + V$, where V is an additive error term. As a check of the GAM against the proposed fully nonparametric approach, we conduct the consistent model specification test of Hsiao et al. (2007) which allows for discrete and continuous predictors. The null hypothesis of this test can be expressed as a test of the mean independence assumption $H_0 : \mathbb{E}(V | \mathbf{X}_P, \mathbf{X}_B) = 0$ a.s. (see Racine, 2019, Sec. 6.10.3, for details and application). We cannot reject the null hypothesis if the GAM residuals from a regression on \mathbf{X}_P and \mathbf{X}_B cannot be explained by an NP regression on \mathbf{X}_P and \mathbf{X}_B . In addition to the GAM, we also test the residuals of a RF in an analogous fashion.

3.4 Results

This section summarizes the results when characterizing the memory properties of the precipitation anomaly series observed in the contiguous United States. We calculate the conventional memory parameter estimates \hat{d}_{LW} and the adjusted memory parameter estimates \hat{d}^* and investigate the heterogeneity of precipitation memory as detailed in Subsection 3.3.3.

3.4.1 Identification, estimation, and inference of precipitation memory parameters

We assess the differences between conventional memory parameter estimates \hat{d}_{LW} and the carefully derived adjusted memory parameter estimates \hat{d}^* . The results differ quantitatively and qualitatively between the two estimates and suggests that further conclusions may be affected substantially by the choice of estimator. Table 3.2 shows the absolute and relative frequencies of potential contaminations of the conventional memory parameter estimates diagnosed by the tests in Subsection 3.3.2 for the US precipitation anomaly series. We find that although the null hypothesis of Qu’s test is rejected for only 4.6% of the series, a substantial fraction of the series show evidence of mean breaks (11.7%), potential contaminations (23.5%), and short-run dynamics (35.9%). Table 3.3 summarizes the number of precipitation anomaly series falling into three regions indicative of anti-persistence, short memory, and long-range dependence. We observe that the number of anomaly series labeled as anti-persistent increases and the number of series with short

Table 3.2: Absolute and relative frequencies of binary variables \mathbf{X}_B for monthly precipitation anomaly series (3.1) from contiguous United States 1990 to 2019.

	Qu spurious	Mean break	Contaminated	ARMA noise
Number of ones	50	126	253	387
Number of zeros	1027	951	824	690
Share of ones	4.6%	11.7%	23.5%	35.9%

Table 3.3: Memory estimates \hat{d}_{LW} and \hat{d}^* for monthly precipitation anomaly series (3.1) from contiguous United States 1990 to 2019 supporting different memory behavior.

Parameter range	Memory behavior	\hat{d}_{LW}	\hat{d}^*
$[-0.5, -0.1]$	Anti-persistent	32	162
$] - 0.1, 0.1[$	Short memory	870	754
$[0.1, 0.5]$	Long memory	175	161

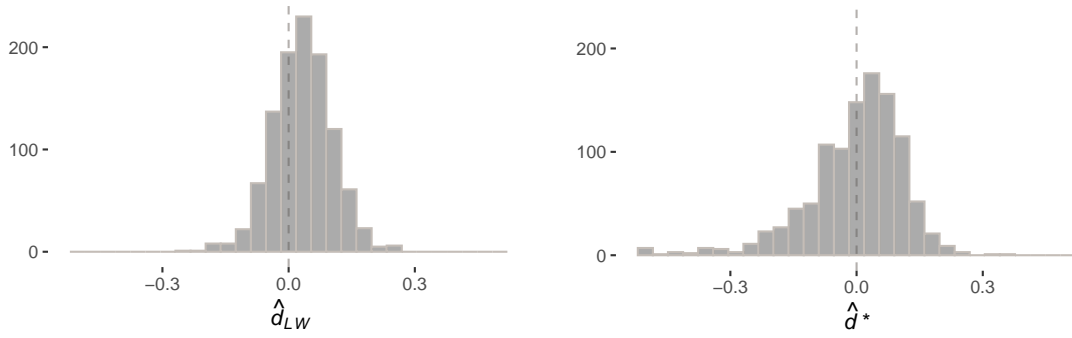


Figure 3.4: Frequency histograms of conventional memory estimates \hat{d}_{LW} (left) and adjusted memory estimates \hat{d}^* (right) for monthly precipitation anomaly series (3.1) from contiguous United States 1990 to 2019. Dashed line indicates zero.

memory decreases, whereas the number of series considered to be long-range dependent remains relatively stable.

The impact of accounting for these diagnosed sources of uncertainty in estimation and inference on the memory parameters is illustrated by the histograms in Figure 3.4. We note that the estimated average memory is lower when we consider \hat{d}^* instead of \hat{d}_{LW} , while its range increases, reflected by a 63.5% increase of the standard deviation (from 0.070 for \hat{d}_{LW} to 0.115 for \hat{d}^*). As a consequence the variation of the memory estimates is underestimated substantially by \hat{d}_{LW} . The five number summary and mean in Table 3.4 and the scatter plot displayed in Figure 3.5 confirm these findings and add further detail.

Figure 3.6 shows maps of \hat{d}_{LW} (top) and \hat{d}^* (bottom) for the contiguous United States. The maps highlight the pronounced differences between the conventional and adjusted memory parameter estimates discussed above, and are also an indication that some of these differences are region-specific: Anti-persistence appears to be more prevalent in southern California and the northern parts of the Midwest in particular for \hat{d}^* compared to \hat{d}_{LW} . Note that these were the two regions in the contiguous United States, where according to the IPCC report the assessment of an increase or decrease in heavy precipitation was difficult due to “Limited data and/or literature” and that the “Confidence in human contribution to the observed change” was “Low due to limited evidence/agreement”, IPCC (2023, p.109).

Table 3.4: Five number summary and mean for conventional memory estimates \hat{d}_{LW} and adjusted memory estimates \hat{d}^* for monthly precipitation anomaly series (3.1) from contiguous United States 1990 to 2019.

	Min.	1st Qu.	Median	Mean	3rd Qu.	Max.
\hat{d}_{LW}	-0.24	-0.01	0.03	0.03	0.08	0.26
\hat{d}^*	-0.50	-0.06	0.02	-0.00	0.07	0.35

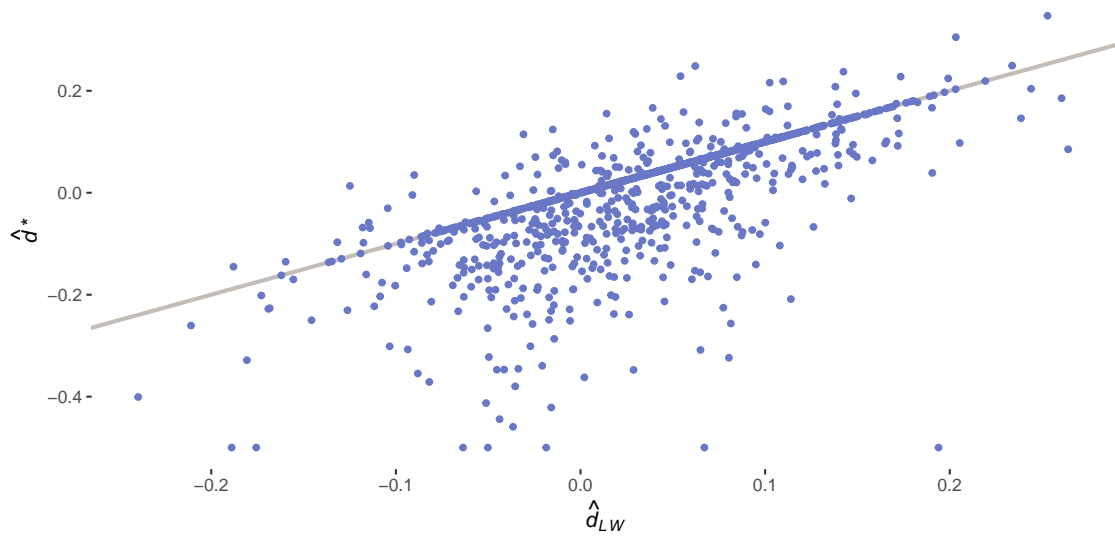


Figure 3.5: Scatter plot of conventional memory estimates \hat{d}_{LW} (abscissa) versus adjusted memory estimates \hat{d}^* (ordinate) for monthly precipitation anomaly series (3.1) from contiguous United States 1990 to 2019. Line is angle bisector.

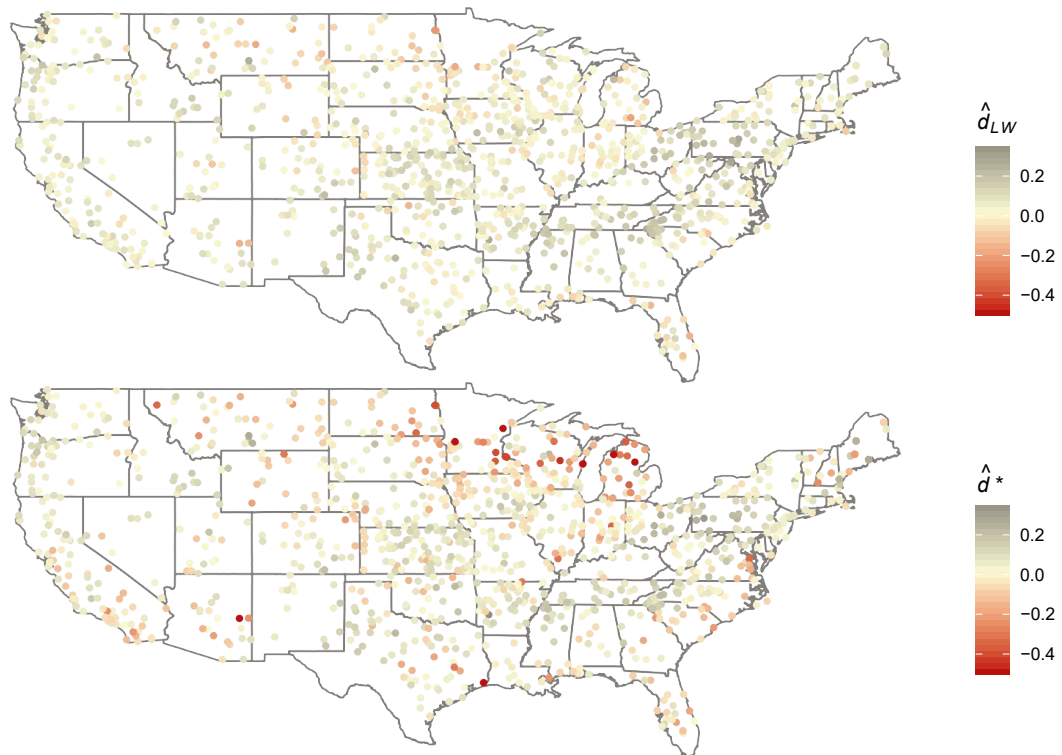


Figure 3.6: Conventional memory estimates \hat{d}_{LW} and adjusted memory estimates \hat{d}^* .

Our results indicate that the memory parameter estimator should be chosen with care and that the conventional memory parameter estimate \hat{d}_{LW} may suffer from severe distortions, as it may be prone to overestimating the degree of fractional differencing. Hence we subsequently focus on the adjusted memory parameter estimate \hat{d}^* . In the appendix, we report additional, qualitatively identical results for other large regions.

3.4.2 The variation in precipitation memory

We investigate the climatological and spatial variation of the memory parameters as previously considered by [Tyralis et al. \(2018\)](#). We extend their work in several directions, first and foremost by using the adjusted memory parameter estimates \hat{d}^* and including the predictor set \mathbf{X}_B to reduce the uncertainty underlying the identification and estimation of the memory parameters. Further, we apply a nonparametric regression framework allowing a straightforward interpretation of the effects of the predictor sets \mathbf{X}_P and \mathbf{X}_B on precipitation memory. Finally, unlike model-free approaches such as RF, the use of regression analysis provides a means for hypothesis testing.

In the context of distribution-free regression, we test not only the relevance of the predictor set \mathbf{X}_B , but also the model specification for GAM and RF versus the alternative NP. Table 3.5 shows results for two nonparametric specifications – NP1 uses predictor set \mathbf{X}_P and NP2 uses predictor set $\mathbf{X} = (\mathbf{X}_P, \mathbf{X}_B)$. We report estimated bandwidths for NP1 and NP2 for the adjusted memory parameter estimate. For continuous predictors, we list the scale factor instead of the bandwidth, since it does neither depend on the scale level of the underlying predictor nor on the number of observations and is thus comparable across predictors, specifications, and geographical regions. Details on the application and interpretation of nonparametric regression models with mixed continuous and discrete predictors can be found in [Li and Racine \(2007\)](#); [Henderson and Parmeter \(2015\)](#); [Racine \(2019\)](#).

The bandwidths and scale factors of the spatial characteristics are remarkably stable across both specifications. The larger scale factor of Latitude compared to Longitude across

Table 3.5: Estimated bandwidths (for discrete predictors), scale factors (for continuous predictors), and model fit of nonparametric specifications NP1 and NP2. Response variable is adjusted memory parameter estimate \hat{d}^* for monthly precipitation anomaly series (3.1) from contiguous United States 1990 to 2019.

	NP1	NP2
Latitude	0.396	0.670
Longitude	0.254	0.300
Altitude	0.922	1.000
Main climate zone	1.000	0.206
Precipitation subgroup	1.000	0.111
Temperature subgroup	0.411	0.501
Qu spurious		0.336
Mean break		1.000
Contaminated		0.080
ARMA noise		0.052
R^2	0.599	0.811

both specifications shows that in either specification, there is a stronger smoothing of the north-south effect than of the west-east effect. This represents more abrupt changes in memory from west to east (and vice versa) than from north to south (and vice versa), which can be linked intuitively to the climatic characteristics of the contiguous United States. Especially the higher share of desert scenery in the west (with longer stable rainfall periods) is expected to cause a very different persistence structure than the east. In contrast, the selected bandwidth values of Altitude suggest that its impact on the spatial variation of estimated memory parameters is negligible in both specifications. In general, the discrete bandwidths are bounded in $[0, 1]$, where a value approaching 0 indicates high relevance of the predictor and a value approaching 1 indicates irrelevance.

Concerning the three climatological predictors we observe the following: Temperature subgroup seems to exert a moderate effect in both specifications (selected bandwidths in between $[0.4, 0.5]$ for both specifications), Main climate zone and Precipitation subgroup are irrelevant in specification NP1, but highly relevant in specification NP2. Looking more closely at the estimated bandwidths of the climatological predictors for the NP2 specification, we find that the precipitation subgroup has the lowest bandwidth and is thus of particular importance for modeling. Thus, the combination of adjusted memory parameters and extended predictor set revealed the relevance of the climatological predictors.

For the four binary predictors \mathbf{X}_B included in specification NP2, the selected bandwidths indicate a high empirical relevance (with the exception of Mean break) after accounting for spatial and climatological characteristics. The [Racine et al. \(2006\)](#) test of joint significance of the predictors \mathbf{X}_B strongly supports this finding (p -value < 0.001).

The estimation and test results imply that the complete set of predictors included in the fully nonparametric specification NP2 is suitable for modeling the spatial and climatological variation of precipitation memory. In particular, all climatological predictors are (highly) relevant. When testing the GAM and the RF as proposed by [Tyralis et al. \(2018\)](#) against the nonparametric regression with the test of [Hsiao et al. \(2007\)](#), the p -values of 0.093 (RF) and 0.018 (GAM) point towards misspecification compared to the NP regression.

3.5 Discussion

Understanding the drivers of precipitation processes is vital for the development of physical process models and improving existing approaches for (short-term) precipitation forecasting. Especially for the latter, refining spatio-temporal correlations is an open field of research and speculated to provide substantial room for improvement for existing approaches ([Berrocal et al., 2008](#); [Kleiber et al., 2011](#); [Bacro et al., 2020](#)). Additionally, interpretations of empirical findings on (changes in) precipitation are intimately connected

with the memory properties of the underlying physical processes to alleviate misuse of statistical methodology and over-interpretation of the results, as long range dependence increases the likelihood of dry spells and wet periods, while in case of anti-persistence, it is less likely that such events are observed over a prolonged time horizon. We have presented a statistical method for obtaining memory parameter estimators adjusted for potential non-standard structures in the processes generating monthly precipitation anomalies. We build on a large literature originated by [Hurst \(1957\)](#); [Le Cam \(1961\)](#); [Mandelbrot and Wallis \(1968\)](#); [Klemeš \(1974\)](#); [Potter \(1979\)](#) on characterizing the memory properties of precipitation series by the degree of fractional differencing d and on recent contributions in the time series literature ([Qu, 2011](#); [Hou and Perron, 2014](#); [Busch and Sibbertsen, 2018](#)) investigating said structures such as level shifts, smooth trends, breaks, or short-run dynamics. The latter are well known to lead to biases in the estimators of memory parameters, making reliable inferences and interpretations impossible. Using a sequence of statistical tests ([Qu, 2011](#); [Shao, 2011](#); [Iacone et al., 2014](#)), we derived binary indicators for these structures, found in roughly one third of the 1,077 precipitation series across the contiguous United States.

Our empirical evidence for precipitation anomalies for the contiguous United States over the past 60 years shows that adjusting memory parameter estimators leads to substantially different conclusions than using conventional ones, such as the most commonly applied approach of local Whittle estimation. In particular, when comparing the adjusted estimates of the memory parameters with the conventional estimates, our results show that the latter tend to overestimate the memory parameters, whereas the former show more than 60% greater variability. Our results also confirm a recent conjecture by [Tyrallis et al. \(2018\)](#) that there is substantial uncertainty in memory parameter estimates resulting from spatio-temporal heterogeneity due to level shifts, smooth trends, and seasonality. This affects inferences about underlying memory properties, as more precipitation series exhibit anti-persistence rather than short memory.

When investigating the variability of the adjusted memory parameter estimates over the United States, we find substantial nonlinearities in the impacts exerted by spatial characteristics, climatological characteristics and the indicators for level shifts/smooth trends and short-run dynamics, supporting the findings in recent literature on changes in United States precipitation patterns ([IPCC, 2021, 2023](#)). We have shown that these results hold for other large regions (Europe, Australia, and global data) in various climate zones worldwide.

Our work also has some limitations and provides further strands of research for future work. First, our method relies on a number of pre-processing strategies, such as the component model and the related de-seasonalizing by Equation (3.1). Extending our framework to multiplicatively linked components and other seasonal decomposition methods such as the approaches outlined by [Dagum and Bianconcini \(2016\)](#) could spark useful

methodological advances. Second, we employ nonparametric regression to investigate the variation in the memory parameters, but the inclusion of additional continuous predictors (beyond the two in this study) into the model specification could add to the curse of dimensionality. In this setting, employing a random-forest-based analysis in the spirit of [Tyrallis et al. \(2018\)](#) or using generalized additive models as done in the robustness checks has specific advantages and disadvantages that need to be considered in greater detail. Third, we investigate the memory properties of precipitation anomaly series obtained from weather monitoring stations, where we aggregate daily total precipitation to monthly values and then compute monthly precipitation anomalies. A natural alternative is to consider a different frequency of the data, as the properties could also be investigated based on an intra-daily (e.g., [Poveda, 2011](#)), daily (e.g., [Yusof et al., 2013](#)), or annual time horizon (e.g., [Illiopoulou et al., 2018](#)). Fourth, additional data sources, such as satellite data or paleoclimatic reconstructions, or different spatial aggregates could be employed to investigate the robustness of the reported results. However, other data sources also have specific advantages and disadvantages that need to be weighed carefully (for a discussion, see [Tapiador et al., 2012](#)). Fifth, it may be interesting to link precipitation and river run-off by reconciling the memory properties of the underlying processes. As suggested by [Potter \(1979\)](#), precipitation is a natural starting point. Fruitful avenues to consider may be models for the physical process that causes river-runoff ([Klemeš, 1974](#)). From a methodological point of view, this involves investigating the effect of aggregating time series which exhibit particular dependence structures and relaxing the assumptions and results of [Granger and Joyeux \(1980\)](#); [Davidson and Sibbertsen \(2005\)](#); [Beran et al. \(2013\)](#). Finally, the special characteristics of precipitation series reveal the need for further research on the estimation and identification of (spurious) long memory. Unreported analyses have shown that the test of [Qu \(2011\)](#) reacts to positive skewness with a negative bias, resulting in a higher type II error and fewer detections of spurious long memory. Additionally, applying an automatic bandwidth selection procedure for the memory estimation as suggested by [Arteche and Orbe \(2017\)](#) would control for short-run dynamics in a more general way, but is yet to be derived for the case of spurious long memory. Developing and applying alternative tests and modified estimation techniques that specifically account for the particularities of precipitation series may also produce interesting new empirical evidence to characterize the underlying memory properties, as definitive conclusions regarding the memory properties of precipitation series are not possible based on empirical data ([Graves et al., 2017](#)).

3.A Appendix

Appendix with three sections: 1. Data and software, 2. Test statistics of the sup-Wald tests for level shifts, 3. Robustness checks for other regions and worldwide precipitation series. The first section provides information on data pre-processing and all employed software. Information on the Köppen climate zone classification and the covariates employed in the estimation of the nonparametric and generalized additive models and the random forests is also provided. The second section details the mean break test statistics, while the final section summarizes the results for the alternative regions Australia, Europe and Global.

3.A1 Data and software

The raw data include daily total precipitation in millimeters, maximum and minimum temperature, snowfall, and snow depth for some monitoring stations. The quality of the data is controlled by automated procedures (Menne et al., 2012). Almost all precipitation series contain a small number of missing values and we imputed the data as follows: Missing values in year t and day d were replaced by inserting the observed precipitation of year $t - 1$ and day d . For leap years, when the precipitation of February 29 was missing in year t , we inserted the value observed on February 28 in year $t - 1$. When there were missing values in the series in year $t - 1$ and day d , we imputed the observed precipitation of year $t + 1$ and day d , where, again, for leap years, February 28 was used when February 29 was missing. We conducted at most two iterations of the imputation scheme and removed all precipitation series, which still contained missing values. Subsequently, total daily precipitation was aggregated to total monthly precipitation.

All computations and visualizations were created with the statistical software R, version 4.2.2 (R Core Team, 2022) employing the packages anytime (Edelbuettel, 2020), arfima (Veenstra and McLeod, 2015), dplyr (Wickham et al., 2017), ggmap (Kahle and Wickham, 2013), ggplot2 (Wickham, 2016), gridExtra (Auguie and Antonov, 2017), LongMemoryTS (Leschinski et al., 2019), lubridate (Grolemund and Wickham, 2011), mgcv (Wood, 2017), np (Hayfield and Racine, 2008), raster (Hijmans et al., 2023), rworldmap (South, 2011), sf (Pebesma and Bivand, 2005), snowfall (Knaus, 2013), sp (Bivand et al., 2013), terra (Hijmans, Bivand, Pebesma and Sumner, 2023), usmap (Di Lorenzo, 2022), and viridis (Garnier et al., 2021).

Köppen climate zone classification

Climate in a particular region arises from the complex interplay of multiple factors such as temperature, precipitation, and other geographical characteristics (e.g., altitude; proximity to sea, rivers, and lakes, or mountains) and is intimately linked with natural habitats of plants and animals. Conventional climate zone classification is based on the three letter scheme of Köppen (1884, 1900a,b, 1918, 1936) and uses temperature and precipitation aggregates and thresholds (e.g., minimum monthly precipitation, minimum mean monthly temperature of coldest month, maximum mean monthly temperature of warmest month; for the specific thresholds, see Table 1 in Belda et al., 2014) to classify a given location into a main climate zone (first letter), a seasonal precipitation subgroup (second letter), and a temperature subgroup (third letter). Seasonal variation of precipitation may be present for climate zones A (tropical climates), C (temperate climates), and D (continental climates). For climate zone B (dry climates) annual rainfall is evenly distributed – while there are no specific requirements for zone E (polar and alpine climates).

We obtained the information on the climate zone of the monitoring stations from <https://koeppen-geiger.vu-wien.ac.at/present.htm> (Kottek et al., 2006). We removed a total of six monitoring stations for which no climate zone classification was available. Figure 3.7 shows a world map, where all land mass is colored according to its Köppen climate zone. All monitoring stations available for the empirical analysis are represented by dots. As indicated by the map, the vast majority of monitoring stations are located in the main climate zones B, C, and D. We therefore removed all stations located in climate zones A and E in the empirical analysis.

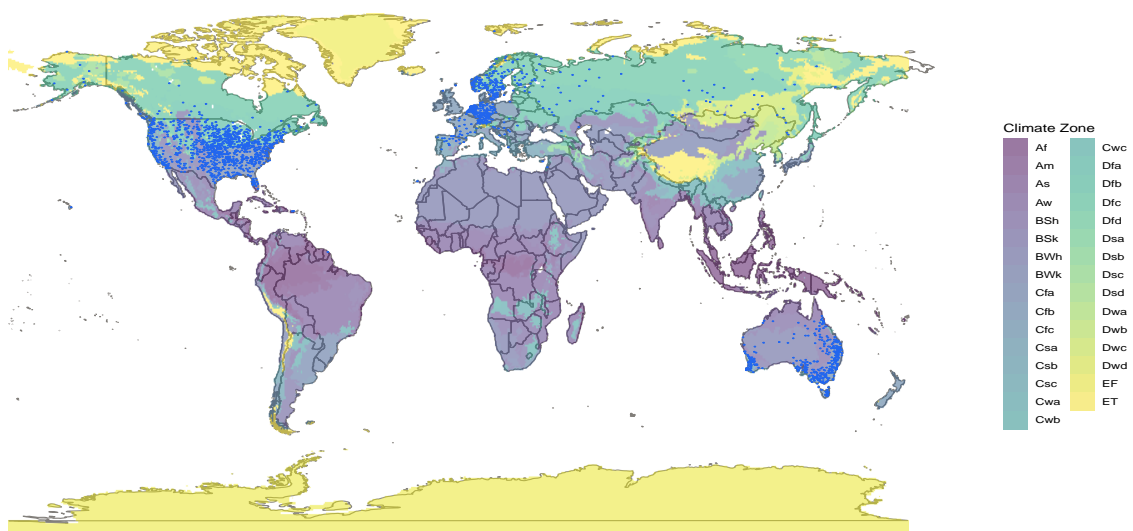


Figure 3.7: Climate zones according to Köppen classified into main climate zone (first letter), seasonal precipitation subgroup (second letter), and temperature subgroup (third letter). Dots indicate locations of available monthly precipitation anomaly series.

Table 3.6 shows the Köppen climate zones and summarizes the number of monitoring stations located in the different climate zones for the two regions “Global” and the contiguous United States. In total, 2118 (Global) and 1077 (contiguous United States) monitoring stations are available for the empirical analysis. Also note that 2009 of the 2118 worldwide monitoring stations are located in Australia, Europe, and the US.

Table 3.6: Köppen climate zones given by three letter classification scheme indicating main climate zone (first), seasonal precipitation subgroup (second), and temperature subgroup (third). Fourth and fifth columns indicate number of monitoring stations in respective climate zone worldwide and in contiguous United States.

Climate zone	Precipitation subgroup	Temperature subgroup	Global	Contig. US
A (tropical)	f (no dry season)		0	0
	w (savanna, dry winter)		0	0
	s (savanna, dry summer)		0	0
	m (monsoon)		0	0
B (dry)	W (desert)	h (hot)	30	8
		k (cold)	13	9
	S (steppe)	h (hot)	72	3
		k (cold)	199	139
C (temperate)	f (no dry season)	a (hot summer)	486	391
		b (warm summer)	504	26
		c (cold summer)	8	0
		a (hot summer)	3	0
	w (dry winter)	b (warm summer)	0	0
		c (cold summer)	0	0
		a (hot summer)	52	23
	s (dry summer)	b (warm summer)	115	74
		c (cold summer)	0	0
D (continental)	f (no dry season)	a (hot summer)	207	206
		b (warm summer)	250	180
		c (cold summer)	147	9
		d (very cold winter)	4	0
	w (dry winter)	a (hot summer)	2	2
		b (warm summer)	9	1
		c (cold summer)	9	0
		d (very cold winter)	0	0
		a (hot summer)	0	0
		b (warm summer)	6	6
	s (dry summer)	c (cold summer)	2	0
		d (very cold winter)	0	0
E (polar and alpine)	T (tundra)		0	0
	F (eternal frost; ice cap)		0	0

Figures 3.8 and 3.9 show precipitation anomalies (median over monitoring stations for main climate zones B (left), C (middle), and D (right), respectively, separately for each month (in rows)) for the evaluation period

$$\tilde{A}_{y:m,\bullet} := \text{med}(A_{y:m,1}, \dots, A_{y:m,1077}), \quad (3.19)$$

suggesting skewness due to an increase of positive precipitation anomalies (with respect to the reference period 1960 to 1989 over the monitoring stations) and pronounced differences in variability over the main climate zones.

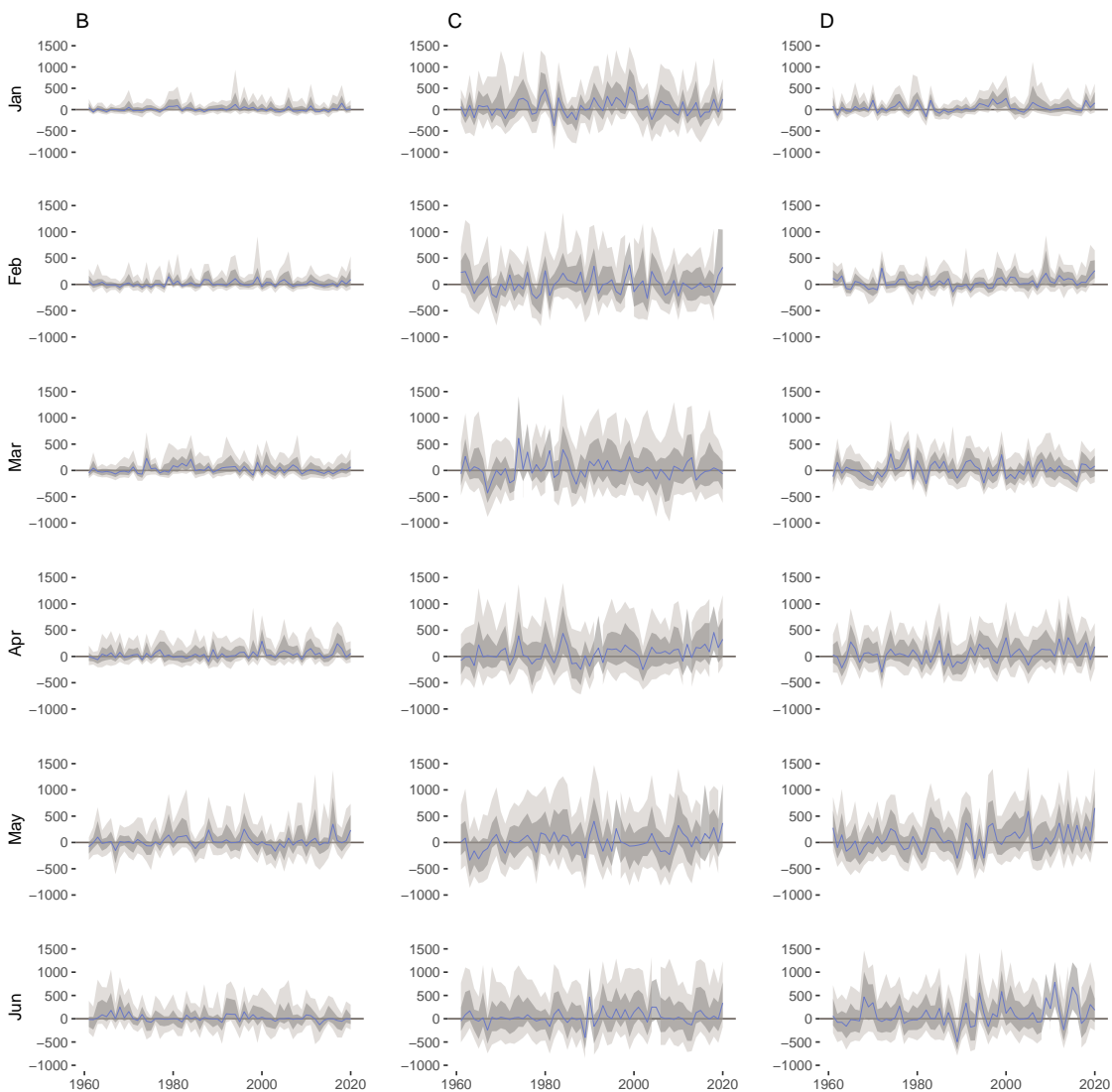


Figure 3.8: Precipitation anomalies $\tilde{A}_{y:m,\bullet}$ calculated according to (3.1) and (3.19) for evaluation period as median over monitoring stations in contiguous United States for main climate zones B (left), C (middle), and D (right), respectively, separately for months: January (top row) to June (bottom row); shaded areas indicate empirical 10%- and 90%-deciles (25%- and 75%-quantiles).

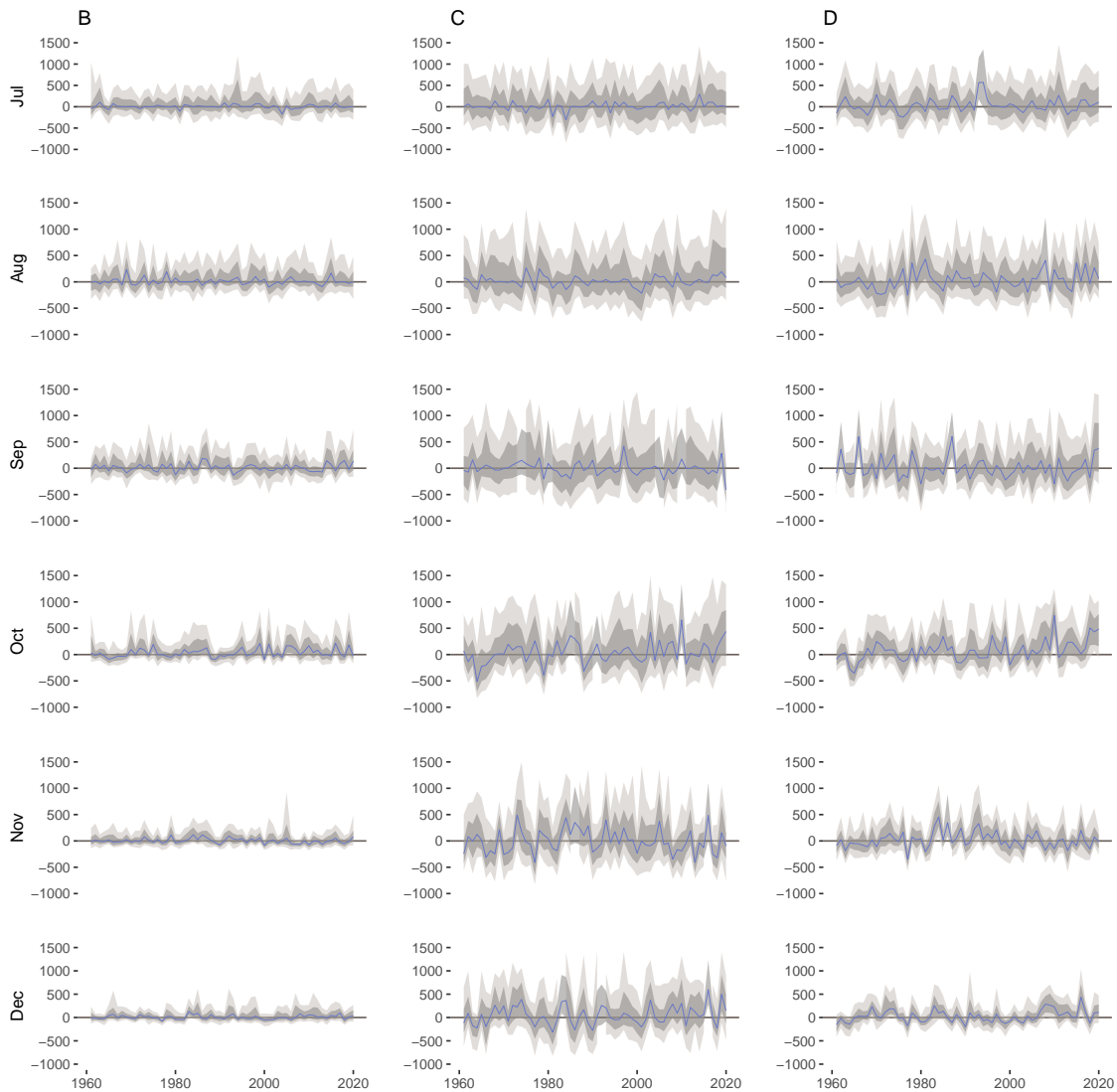


Figure 3.9: Precipitation anomalies $\tilde{A}_{y:m,\bullet}$ calculated according to (3.1) and (3.19) for evaluation period as median over monitoring stations in contiguous United States for main climate zones B (left), C (middle), and D (right), respectively, separately for months: July (top row) to December (bottom row); shaded areas indicate empirical 10%- and 90%-deciles (25%- and 75%-quantiles).

Variable description

Table 3.7 lists the names, descriptions, and variable types of all predictors employed in the empirical analysis. Additionally, some descriptive statistics for the monitoring stations located in the contiguous United States are provided, where the mean (mode) is reported for the continuous and binary (discrete) predictors. We employ two predictor sets \mathbf{X}_P and \mathbf{X} . The former consists of the spatial characteristics Latitude, Longitude, and Altitude (the latter grouped into deciles) as well as the (categorical) variables Main climate zone, Precipitation subgroup, and Temperature subgroup that reflect the three letter climate zone classification by Köppen. This set of predictors was also employed in the analysis of [Tyrallis](#)

Table 3.7: Name, description, type of predictors employed in empirical analysis and descriptive statistics for contiguous United States and Global.

Name	Description	Type	Global		Contiguous US	
			Mean/Mode	#Categ.	Mean/Mode	#Categ.
X_{lon}	Longitude	metric	-20.46		-95.88	
X_{lon}	Latitude	metric	31.12		39.34	
X_{alt}	Altitude	discrete	2	10	10	10
X_{clz}	Main climate zone	discrete	C	5	C	3
X_{prc}	Precipitation subgr.	discrete	f	7	f	5
X_{tmp}	Temperature subgr.	discrete	b	5	a	5
X_{sprs}	Qu spurious	binary	0.070	2	0.046	2
X_{mbrk}	Mean break	binary	0.105	2	0.117	2
X_{ctmd}	Contaminated	binary	0.245	2	0.227	2
X_{arma}	ARMA noise	binary	0.367	2	0.359	2

et al. (2018). The second set of predictors \mathbf{X} additionally comprises the four binary predictors Qu spurious, Mean break, Contaminated, and ARMA noise as detailed in Subsection 3.3.3.

Note that the Altitude deciles were determined based on all monitoring stations worldwide. For the contiguous United States, a total number of 187 stations was located in the tenth decile, for which the actual altitudes ranged from 906 to 2763 meters above sea level.

3.A2 Test statistics of the sup-Wald tests for level shifts

The self-normalization approach of Shao (2011) modifies the common sup-Wald test by including the self-normalizer

$$G(t^*) = \left(\frac{1}{T} \sum_{t=1}^{t^*} S_t^2(1, t^*) + \frac{1}{T} \sum_{t=t^*+1}^T S_t^2(t^* + 1, T) \right)^{1/2}$$

with $S_t(j, t^*) = \sum_{h=j}^t (A_h - \bar{A}_{j, t^*})$ and $\bar{A}_{j, t^*} = \frac{1}{t^* - j + 1} \sum_{t=j}^{t^*} A_t$, which is proportional to a consistent estimate of the long-run variance. The test statistic is then given by

$$Q_{SNSW} = \sup_{t^* \in (t_1^*, t_2^*)} \frac{|\hat{\beta}(t^*)|}{G(t^*)} \quad (3.20)$$

for OLS estimates $\hat{\beta}$.

The fixed- b modification of [Iacone et al. \(2014\)](#) uses the long-run variance estimate

$$\widehat{\sigma}_b^2(t^*) = \widehat{\gamma}_0(t^*) + 2 \sum_{j=1}^{T-1} k\left(\frac{j}{M}\right) \widehat{\gamma}_j(t^*),$$

where $\widehat{\gamma}_j(t^*) = T^{-1} \sum_{t=j+1}^T \widehat{\varepsilon}_t(t^*) \widehat{\varepsilon}_{t-j}(t^*)$ denote autocovariance estimates based on the OLS residuals $\widehat{\varepsilon}_t$ from (3.15). Further, $k(\cdot)$ is a kernel function with bandwidth M such that $M = \lfloor bT \rfloor$ for $b \in (0, 1)$. This leads to the test statistic

$$Q_{FBSW} = \sup_{t^* \in (t_1^*, \dots, t_2^*)} \frac{\widehat{\beta}(t^*)^2}{\widehat{\sigma}_b^2 c M_{AA}(t^*)^{-1} c'}, \quad (3.21)$$

where $c = (0, 1)$ and $M_{AA}(t^*) = \sum_{t=1}^T A_t(t^*) A_t(t^*)'$ for $A_t = (1, \mathbb{1}(t \geq t^*))'$. Consequently, the denominator converges to the long-run variance multiplied by a functional of a Brownian bridge. In our application, we set $(t_1^*, t_2^*) = (0.15, 0.85)$ and use the Bartlett kernel with $b = 0.1$, as suggested by [Iacone et al. \(2014\)](#).

3.A3 Robustness checks for other regions and worldwide precipitation series

We apply the proposed method to the alternative regions Global ($n = 2118$), Australia ($n = 383$), and Europe ($n = 549$) to check the robustness of our modeling framework analogous to the results of Section 3.4.

Identification, estimation, and inference of precipitation memory parameters

Table 3.8 summarizes the absolute and relative frequency of potential contaminations of the conventional memory parameter estimates for the worldwide precipitation anomalies as diagnosed by the classification scheme in Subsection 3.3.3. The results are qualitatively identical to the ones for the contiguous United States provided in Table 3.2. While the relative number of diagnosed mean breaks, potential contaminations, and short-run dynamics remain almost unchanged, the H_0 of Qu's test is rejected for a larger fraction of the investigated anomaly series.

Table 3.8: Absolute and relative frequencies of the binary variables X_B for 2,118 global monthly precipitation anomaly series (3.1) from 1990 to 2019.

	X_{sprs}	X_{mbrk}	X_{ctmd}	X_{arma}
Number of ones	141	199	497	743
Number of zeros	1878	1820	1522	1276
Share of ones	7.0%	9.9%	24.6%	36.8%

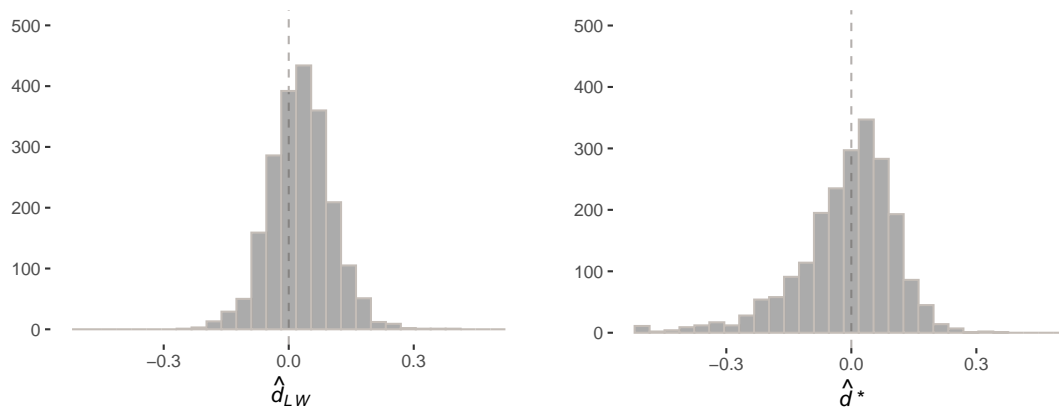


Figure 3.10: Frequency histograms of estimated conventional memory estimates \hat{d}_{LW} (left) and adjusted memory estimates \hat{d}^* (right) for 2,118 global monthly precipitation anomaly series (3.1) from 1990 to 2019. Dashed line indicates zero.

When comparing the histograms for the conventional memory parameter estimates \hat{d}_{LW} and the adjusted estimates \hat{d}^* for the precipitation anomaly series from the contiguous United States in Figure 3.4 to the ones for the global precipitation anomaly series displayed in Figure 3.10, the conclusions remain unchanged: The range of memory parameter estimates increases and the corresponding empirical standard deviation increases substantially (by 57.8% from 0.073 to 0.116). Virtually identical conclusions result when considering the materials in Tables 3.9 and 3.10 as well as Figure 3.11 with the respective materials in Section 3.4.1.

Table 3.9: Five number summary and mean for estimated conventional memory estimates \hat{d}_{LW} (first row) and adjusted memory estimates \hat{d}^* (second row) for 2,118 global monthly precipitation anomaly series (3.1) from 1990 to 2019.

	Min.	1st Qu.	Median	Mean	3rd Qu.	Max.
\hat{d}_{LW}	-0.24	-0.02	0.03	0.03	0.07	0.40
\hat{d}^*	-0.50	-0.07	0.01	-0.01	0.07	0.35

Table 3.10: Memory parameter estimates \hat{d}_{LW} and \hat{d}^* for 2,118 global monthly precipitation anomaly series (3.1) from 1990 to 2019 falling into three regions that support different memory behavior.

Parameter range	Memory behavior	\hat{d}_{LW}	\hat{d}^*
$[-0.5, -0.1]$	Anti-persistent	76	365
$] -0.1, 0.1[$	Short memory	1719	1470
$[0.1, 0.5]$	Long memory	323	283

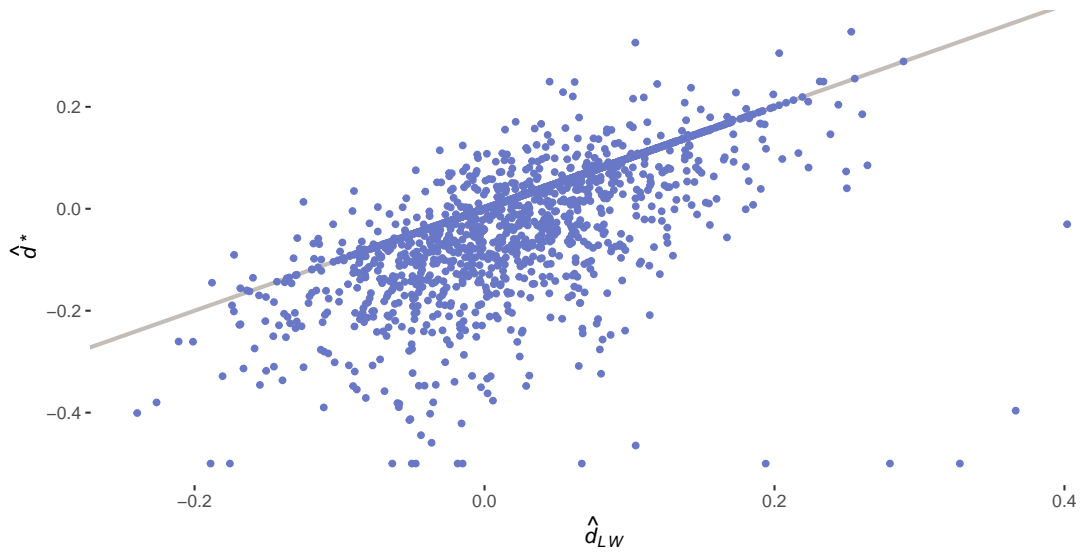


Figure 3.11: Scatter plot of estimated conventional memory estimates \hat{d}_{LW} (abscissa) versus adjusted memory estimates \hat{d}^* (ordinate) for 2,118 global monthly precipitation anomaly series (3.1) from 1990 to 2019. Line is angle bisector.

The variation in precipitation memory

The results for the different regions are shown in the columns of Table 3.11 in comparison to the results for the contiguous United States from Table 3.5 (1077 obs., columns 7 and 8). We observe the following:

- The table shows that globally, we have the identical spatial characteristics (more smoothing of Latitude than of Longitude and low relevance of Altitude) as for the contiguous United States. For Australia and Europe this is not the case and we observe less smoothing of the north-south effect than of the west-east effect for both regions. Hence, the memory parameter estimates in Australia and Europe are supposed to change more abrupt from north to south than from west to east (and vice versa). Altitude is of low relevance for all regions apart from Europe (in model NP2).
- Regarding the climatological characteristics, the bandwidth values tend to be higher for the models NP1. This indicates a lower relevance of the climatological characteristics. Conversely, we can observe lower bandwidth values in the NP2 models pointing towards a higher relevance of the climatological predictors. Hence, as for the contiguous United States this effect becomes visible when the extended predictor set is used (i.e., for NP2). Again and for all regions we obtain the smallest bandwidths of the climatological predictors for the predictor Precipitation subgroup.
- The test of [Racine et al. \(2006\)](#) for joint significance of the additional predictors yields a rejection of the null hypothesis for all regions (all p -values are below 0.001), underlining the importance of predictor set \mathbf{X}_B .

Table 3.11: Estimated bandwidths (discrete predictors), scale factors (continuous predictors), and fit of nonparametric regressions NP1 and NP2. Response variable is adjusted memory parameter estimate \hat{d}^* of precipitation anomaly series from 1990 to 2019; columns indicate regions Global, Australia, Europe, and contiguous United States.

Predictor	Global		Australia		Europe		Contiguous US	
	NP1	NP2	NP1	NP2	NP1	NP2	NP1	NP2
Latitude	0.206	0.330	0.259	0.256	0.594	0.964	0.396	0.670
Longitude	0.061	0.086	0.422	0.451	0.602	1.008	0.254	0.300
Altitude	1.000	0.815	1.000	1.000	1.000	0.385	0.922	1.000
Main climate zone	1.000	0.248	0.379	1.000	<0.001	0.145	1.000	0.206
Precipitation sub.	0.981	0.066	1.000	0.008	0.339	0.137	1.000	0.111
Temperature sub.	0.366	0.739	0.738	1.000	0.011	0.455	0.411	0.501
Qu spurious		0.805		1.000		0.247		0.336
Mean break		0.512		0.887		0.031		1.000
Contaminated		0.033		0.001		0.040		0.080
ARMA noise		0.032		0.002		0.110		0.052
R^2	0.586	0.806	0.680	0.917	0.508	0.783	0.599	0.811

Besides the nonparametric regressions, we also estimated two generalized additive models (GAM) which included the predictors \mathbf{X}_P (GAM1) and \mathbf{X} (GAM2). Table 3.12 shows the coefficient estimates and corresponding standard errors (in parentheses) for the discrete predictors and the effective degrees of freedom (edf) and the respective p -values for the two continuous predictors of GAM1 and GAM2. The edf correspond to the degrees of freedom involved in fitting the smooth effect of Longitude and Latitude and provide a measure for its complexity. Both models were fitted using the adjusted estimate \hat{d}^* as response.

We observe the following across the estimated GAMs: (i) The complexity of the smooth effect remains highly relevant (p -value < 0.001). (ii) The model fit varies widely across the regions and ranges from 0.207 (GAM1 for Australia) to 0.647 (GAM2 for Australia). (iii) The fit of the specification GAM2 always exceeds the one of GAM1. The differences in the fit range from 11.3 (Europe) to 19.7 (contiguous United States) percentage points. (iv) Wald-tests reveal that the binary predictors are empirically relevant, as the null hypothesis that their joint effect is zero is rejected for all specifications (p -values < 0.001).

We perform the test of Hsiao et al. (2007) for the generalized additive model GAM2 and a random forest analogous to Tyralis et al. (2018) for all regions. This test shows to directly compare our proposed nonparametric model NP2 to the competitors.

We can observe that for a significance level $\alpha = 0.01$, GAM2 is rejected for all regions, apart from Australia and the contiguous United States. Hence, for these two regions, the GAM seems to capture the relevant structure and interplay of all predictors adequately. Since GAM2 has similar flexibility to NP2 with respect to the two continuous predictors, this result suggests that the interplay of the discrete variables in particular is much more

Table 3.12: Coefficient estimate and standard error (discrete predictors) and effective degrees of freedom and p -value (smooth effect of Longitude and Latitude) for generalized additive models GAM1 and GAM2. Response is adjusted memory parameter estimate \hat{d}^* of precipitation anomaly series from 1990 to 2019; columns indicate regions Global, Australia, Europe, and contiguous United States.

Predictor	Global		Australia		Europe		Contiguous US	
	GAM1	GAM2	GAM1	GAM2	GAM1	GAM2	GAM1	GAM2
Qu spurious		0.650 (0.147)		-0.084 (0.011)		-0.045 (0.008)		-0.009 (0.004)
Mean break		0.260 (0.093)		-0.073 (0.095)		0.062 (0.050)		0.113 (0.063)
Contaminated		0.433 (0.104)		-0.016 (0.031)		0.028 (0.049)		0.031 (0.045)
ARMA noise		0.316 (0.072)		0.018 (0.066)		-0.027 (0.016)		-0.031 (0.006)
s(Lon, Lat)	27.354 <0.001	26.304 <0.001	21.114 <0.001	21.364 <0.001	23.334 <0.001	22.493 <0.001	24.070 <0.001	25.104 <0.001
R^2	0.207	0.392	0.474	0.647	0.362	0.475	0.262	0.459

complex than modeled by GAM2 (for all but the aforementioned regions). Of course, the GAM could be extended by parametric interaction effects of arbitrary order. However, these effects have to be specified a priori based on subject-matter knowledge. Table 3.13 shows that the random forest is rejected only for the global specification. Hence, for all other regions, the random forest seems to sufficiently capture the explanatory potential of all predictors. Note however, that we employed the asymptotic version of the test of Hsiao et al. (2007), while the authors propose that the bootstrap versions of the test will have additional power. Nevertheless, it was not our intention to overturn previous results. Instead, we wanted to underline that the nonparametric mixed kernel regression seems to be an appropriate model in this context.

Table 3.13: p -values of model specification test of Hsiao et al. (2007) based on asymptotic test distribution.

Model	Global	Australia	Europe	Contiguous US
Random Forest	0.002	0.222	0.831	0.093
Generalized Additive Model	<0.001	0.249	<0.001	0.018

Germany's Transition Towards Renewable Energies

Empirical Evidence from a Time Series Perspective

4.1 Introduction

In Germany, energy supply alone accounts for one third of the greenhouse gas emissions, which are the main cause of climate change (UBA, 2023b). Along with international endeavors to substantially reduce greenhouse gas and especially carbon dioxide emissions, a more sustainable and environmentally clean energy mix has been determined by German law in the “Erneuerbare-Energien-Gesetz” (EEG) since the year 2000. As stated in its latest version, Germany's gross energy consumption is supposed to come from 65% renewable energies until 2030, and conventional energy sources are to be fully replaced by the year 2050 (UBA, 2021). Although this includes potential imports and exports of green energy, the need for a boost of renewable power sources becomes obvious for both energy production in Germany and on an international level.

Conventional energies depend on finite fossil resources and are tied to substantial carbon dioxide emissions, whereas renewable energies are based on non-depletable natural sources and do not directly cause emissions (UN, 2023b). Additionally, renewable energy sources are shown to involve a lower levelized cost of electricity, which describes all financial expenses associated with generating and converting energy to electricity (Fraunhofer ISE, 2021). Despite of these environmental and financial benefits, the main renewable energy sources come with the difficulty of depending on volatile weather determinants such as wind speed and solar radiation, which occasionally leads to large imports of electricity whenever the intermittent energy sources (wind and photovoltaics) fail to meet Germany's energy demand (Netztransparenz.de, 2020). Complementing the intermittent energy sources, other renewable energies provide more stability and thus help replicating the benefits of the current energy mix that is still dominated by conventionals. In particular, the capacity for biomass energy was increased over the recent years, to allow a more demand-driven deployment of renewable energies and fill supply gaps due to fluctuating wind and solar energy generation (UBA, 2023a). However, biomass plants are rather inefficient compared to fossil fuels and they may have negative agricultural and

environmental impacts. Then, hydropower-based plants provide a highly efficient energy source, but in turn depend on precipitation and water availability, and come with great initial costs (Halkos and Gkampoura, 2020). Finding a system of renewable sources that provides the same capacity, reliability, and controllability as the current energy mix is therefore a major challenge in the transition towards a fully renewable energy mix. While the shortcomings of the renewable energy sources at hand suggest the need for new technologies in the long run, understanding the interplay and substitution possibilities of the already available sources is essential for securing Germany's energy future.

A large branch of literature has addressed the multiple challenges that are entailed in replacing conventional energy sources, and some examples thereof will be given in the following. A general overview on the advantages and drawbacks of existing renewable sources was given by Halkos and Gkampoura (2020), while Böhringer et al. (2020) provided an expert survey on the potential of new technologies and prerequisites for their success on the energy market. For the United States, a detailed analysis of the characteristics of both existing and future technologies and their possible interplay to mimic the conventional energy mix was given by Ramirez-Meyers et al. (2021). Rethinking the whole German energy mix from a technological point of view, scenarios for fully renewable settings were developed and reviewed by Hansen et al. (2019) and Naegler et al. (2021), amongst others. From an economic perspective, Guidolin and Guseo (2016) and Pegels and Lütkenhorst (2014) analyzed the competitiveness of intermittent energy sources in terms of costs and social effects. Turning to the financial aspects, the so-called merit order effect has been studied by many researchers, which describes the reduction of electricity prices due to an increased use of renewable energies. For instance, Paraschiv et al. (2014) built a state space model which links the electricity price to a range of fundamental variables such as commodity prices and expected demand, and more recently, Antweiler and Muesgens (2021) explained the merit order effect through a temporary adjustment to the increasing capacity of intermittent renewable energies and their disruption of established pricing mechanisms.

This work contributes to the understanding of the German energy mix by providing an in-depth analysis of its composition over time and implications for the transition towards a system that is entirely based on renewable energies. Through applying univariate time series methods to daily historical data of Germany's power generation and consumption, seasonal patterns, temporal trends, and degrees of persistence of the different energy sources are captured. On the one hand, this enables the interpretation of both seasonal peculiarities and the reliability and long-term tendency of each power source individually. On the other hand, being able to model and extract these characteristics then allows to comprehend the underlying interdependencies of the energy sources and derive general implications for the future energy mix. In particular, the obtained results highlight the unique role of the intermittent wind and solar energy sources and their deficiencies in

replicating the benefits of conventional energy sources in distinction to other established renewable energy sources.

The data set in focus consists of daily power generation from Germany's twelve energy sources and total consumption in the years 2016 to 2022. This time span does not only cover important steps on the way to a renewable energy mix, i.e. the constantly increasing capacity of renewable energies and the gradual shutdown of conventional power plants, but also captures impacts of both the Covid-19 crisis in 2020 and the Russian invasion of Ukraine in 2022 on the German energy supply and demand. As each of the power series shows a very particular seasonal structure, a detrending scheme is proposed that is specifically tailored to the German energy market and which considers long-term movements as well as weekday and holiday effects. Not accounting for seasonality and temporal trends would strongly bias the results on persistence and correlation of the series, and, additionally, the implications from the detrending estimation provide interesting insights into the dynamics of the German energy mix. For the detrended power generation and consumption series, the degree of persistence is then assessed. More precisely, each of the series exhibits so-called long memory (or long-range dependence), which refers to significant dependencies of time series observations across large time lags and can be interpreted as a measure of stability or reliability of the respective energy source. For estimation of the degree of long-range dependence, i.e. the memory parameter or fractional integration order $0 < d < 1$, the local Whittle estimator by [Künsch \(1987\)](#) is used in combination with the bandwidth selection procedure by [Arteche and Orbe \(2017\)](#). Possible bias from structural breaks or short-range noise components is ruled out with help of the test of [Qu \(2011\)](#) for spurious long memory in order to reduce the uncertainty involved in the estimation. The resulting memory parameter estimates allow to divide the twelve energy sources into three groups: the intermittent renewable energy sources with a low degree of persistence ($0 < d < 0.2$), the base load and peak load sources that reflect the typical characteristics of a conventional energy mix ($0.2 < d < 0.5$), and the rarely adjustable base load or aggregated power sources with nonstationary long memory ($0.5 < d < 0.7$). Looking beyond the univariate seasons, trends, and fractional integration then allows to make a first step in the multivariate direction, where the interdependencies of the twelve energy sources are explained based on simple correlations of the detrended and differenced series. Tying in with previous results, the power generation from the intermittent energy sources are found to be negatively correlated with the other series, again confirming their unique status in replacing the conventional power sources.

The remainder of this paper is structured as follows. Section 4.2 introduces the underlying data set and reports basic pre-processing steps that were applied to remove obvious outliers and level shifts from the series. Section 4.3 proposes the detrending scheme and provides an interpretation of the obtained trends and cycles. In Section 4.4, the theoretical background of long memory and the local Whittle estimation under optimal bandwidth

selection are presented, the possibilities of spurious long memory and ARMA noise are investigated, and memory estimates are obtained and interpreted. Finally, Section 4.5 relates previous findings to multivariate interdependencies of the detrended and fractionally differenced series, and Section 4.6 concludes.

4.2 Data description and pre-processing

In the following, the data set on Germany's energy generation and consumption as the main subject of this paper is described, and pre-processing steps with respect to obvious outliers and level shifts are reported. The data set under consideration is taken from the German Bundesnetzagentur (SMARD.de) and describes net electricity in MWh generated by the different plant types contributing to the German energy market, as well as energy consumption in Germany.¹ All series are available in 15 minute intervals and are aggregated to daily frequency in the range from 01-01-2016 to 31-12-2022 (CET), leading to $T = 2557$ observations in each series.²

In general, the power sources are divided into six conventionals and six renewables:

- *Nuclear.Energy, Brown.Coal, Hard.Coal, Natural.Gas, Pumped.Storage*, and *Other.Conventionals* (including mineral oil or by-products from coal extraction and industry),
- *Biomass, Hydropower, Wind.Offshore, Wind.Onshore, Photovoltaics*, and *Other.Renewables* (including geothermal energy, biological by-products that are not included in the strict definition of biomass, and firedamp).

To further analyze the course of the overall generation from conventional and renewable sources, aggregated series are considered for both groups (*All.Conventional, All.Renewable*), as well as the total power generation (*All*). In addition, the German energy consumption is considered (*Total.Load*).

As dictated by EEG regulations, the importance of these twelve energy sources in the German energy mix has shifted over the years (a visualization thereof is given in Figure 4.9 of the appendix). In general, the share of power generation from renewable energy sources has increased from about 31.6% to 46.1% of the total energy production since 2016, which

¹ According to SMARD.de, the net electricity volume excludes power generation that is not available to the market, i.e. energy directly used for operating the power plants or being part of self-contained industrial power grids as, e.g., provided by the German railway company.

² Data would be available starting at 01-01-2015. However, thorough inspection of the data revealed special challenges during 2015, caused by the fact that renewable sources were just emerging as relevant contributors to the market. This caused outliers and breaks in trend or other structural breaks within 2015. To generally enable stationarity of the considered time series and a consistent definition of the twelve energy sources, data prior to 2016 is omitted.

is mainly driven by the rise of wind and solar energy production. Coming from an energy mix dominated by conventional energy sources, this transformation challenges a reliable and secure energy supply. So far, the nuclear and coal-based energy sources provided a base load supply that satisfied the ground level of energy demand, whereas the energy from natural gas was used more flexibly (peak load) to balance demand fluctuations, and pumped storage served as a general balancing instrument of power supply and demand (IRENA, 2015; SMARD.de, 2023). Due to implementation of the EEG, however, the use of nuclear energy has decreased substantially and is in fact fully shutdown since April 2023. Similarly, a decline of coal-based energy was initiated, although this was occasionally outbalanced by an increase in power supply from natural gas. As the intermittent wind and solar energy sources provide a rather unsteady and unpredictable supply, biomass plant capacity was generally increased to handle demand peaks, while the potential for expanding hydropower capacity is widely exhausted (UBA, 2023a).

Before turning to the detrending procedure in Section 4.3, four series are cleaned from obvious outliers and level shifts, which are either induced by a planned shutdown procedure, or presumably stem from recording errors or an official redefinition of the energy source. First, the shutdown of three major plants of *Nuclear.Energy* at the end of 2021 is addressed by replacing the mean after the break point with the mean of the two previous years. Similarly, the series *Other.Conventionals* is updated with respect to a mean break at the early beginning of 2018. In the *Biomass* series, one week of outliers in September 2017 is mean-corrected with the average of the two surrounding observations. And last, one outlier at late October 2022 in the series *Other.Renewables* is replaced by the mean of its neighboring values. All other particular characteristics of the data are assumed to reflect either seasonal features or variations in the production of the corresponding power type, indicating changing importance in the energy mix, and are thus left within the data. Regarding the power consumption, no pre-processing is required.

To allow for better comparability of results, all series are further standardized to zero mean and unit standard deviation. The resulting time series are displayed in the appendix in Figure 4.11. Particular for the power series is the strong seasonal pattern that drives all energy sources and the consumption, and which will be analyzed in detail in Section 4.3. When looking beyond the seasonal patterns, different degrees of persistence in the series become apparent, which is subject of Section 4.4.

4.3 Seasonal effects

All generation and consumption series feature nonstationarity in form of seasonal patterns and trends. In this setting, a reliable estimation of the persistence of the series is not possible. Therefore, a detailed detrending scheme is applied that is tailored to the particular characteristics of the German electricity market, removing major trends and seasonal effects from the data: a linear temporal trend, annual and semi-annual cycles with possibly changing amplitude, influence of the different week days on power generation and consumption, and the impact of public holidays. Before turning to the detrending scheme and its results in Sections 4.3.1 and 4.3.2, respectively, a visualization of the series' development in the considered time period is given in Figure 4.1.

The circular plots allow to compare the annual dynamics of the time series across the considered years. Without any trends, seasonality, or breaks within the data, one could see stationary movement around a well-centered and properly round circle. In contrast, a temporal trend is reflected by a shift of the circle over time, such that the two colors representing start and end time are separately visible (e.g., as for the *Brown.Coal* series). If there is a pronounced annual season, the circle becomes off-centered or even gets a non-circular shape (e.g., as for *Biomass*). And further, an annual cutout in the circle can be led back to holiday effects (e.g., as for *Hard.Coal*). As the depicted circular plots all deviate from well-centered and properly round circles, they allow first insights on the German energy mix and its seasonality and overall dynamics, while at the same time stressing the need for thorough detrending of the power generation and consumption series.

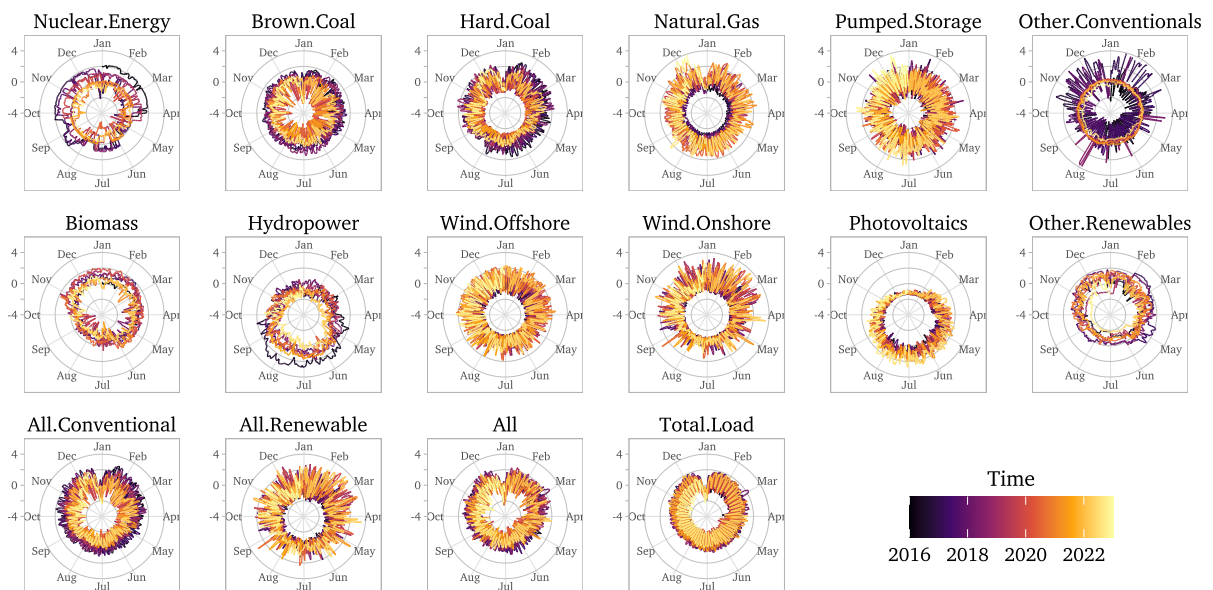


Figure 4.1: Circular plots for the development of power generation and consumption over time, before detrending (pre-processed and standardized series).

4.3.1 Detrending procedure

In order to capture trends and seasonality, a flexible regression model is built which contains different trends, cycles, and dummy variables that proved relevant for the German energy market. Its full formula for any observation at time $t = 1, \dots, T$ is given by

$$\begin{aligned}
 y_t = & \beta_0 + \beta_1 t \\
 & + \sum_{i=1,2} \sin\left(\frac{2\pi t}{\omega_i}\right) \cdot (\alpha_{\sin,i} + t \cdot \gamma_{\sin,i}) + \cos\left(\frac{2\pi t}{\omega_i}\right) \cdot (\alpha_{\cos,i} + t \cdot \gamma_{\cos,i}) \\
 & + \sum_{i=1,\dots,6} \delta_i D_{it} + \sum_{i=1,\dots,19} \eta_i H_{it} \\
 & + x_t
 \end{aligned} \tag{4.1}$$

with a total of $p = 34$ possible regressors for detrending. The first two terms refer to demeaning and linear detrending of the data. The trigonometric components then reflect both an annual and semi-annual cycle ($\omega_1 = 365.25$, $\omega_2 = \frac{365.25}{2}$) which are flexibly shifted in phase by adding up sine and cosine elements. The corresponding coefficients $\alpha_{\sin,i}$, $\alpha_{\cos,i}$ define the amplitude of the sine and cosine waves, while the trend interaction terms with coefficients $\gamma_{\sin,i}$, $\gamma_{\cos,i}$ allow for a shifting amplitude over time. The variables D_{it} provide binary indicators for the week days from Tuesday to Sunday, as varying labor input unequivocally has an effect on power generation in at least some of the plant types and on the overall demand. Similarly, 19 dummy variables H_{it} catch the effect of major public holidays in Germany, plus the days around Christmas and the turn of the year.³ The error term x_t then includes all dynamics that are not captured by the given trends, seasonal effects, or weekend or holiday effects.

As will be shown in Section 4.4, the power generation and consumption series, and consequently also the error term x_t from this regression setup, are long-range dependent. Under long memory errors, the variance of the OLS estimator converges more slowly to zero than under independent short-range errors (Beran, 1994; Yajima, 1988).⁴ Rather than relying on possibly over-estimated t -statistics and under-estimated p -values, the most suitable detrending mix from the regression model in equation (4.1) is therefore obtained individually via best subset selection. There, the best model (in terms of minimal residual sum of squares, RSS) containing k regressors for $k = 1, \dots, p$ is estimated with OLS (as,

³ More precisely, only those holidays are considered that have a nationwide scope or that apply to a larger part of Germany, such as Fronleichnam, Reformationstag, and Allerheiligen. At late December, power generation and consumption on 23rd and from 27th to 30th proved to be affected by the surrounding holidays.

⁴ In general, if the regressors have no pole at the origin of the spectral density, as is the case in the given detrending scenario, OLS still is asymptotically efficient. However, for finite samples it is reasonable to find a strategy that circumvents any possible bias induced by long memory errors.

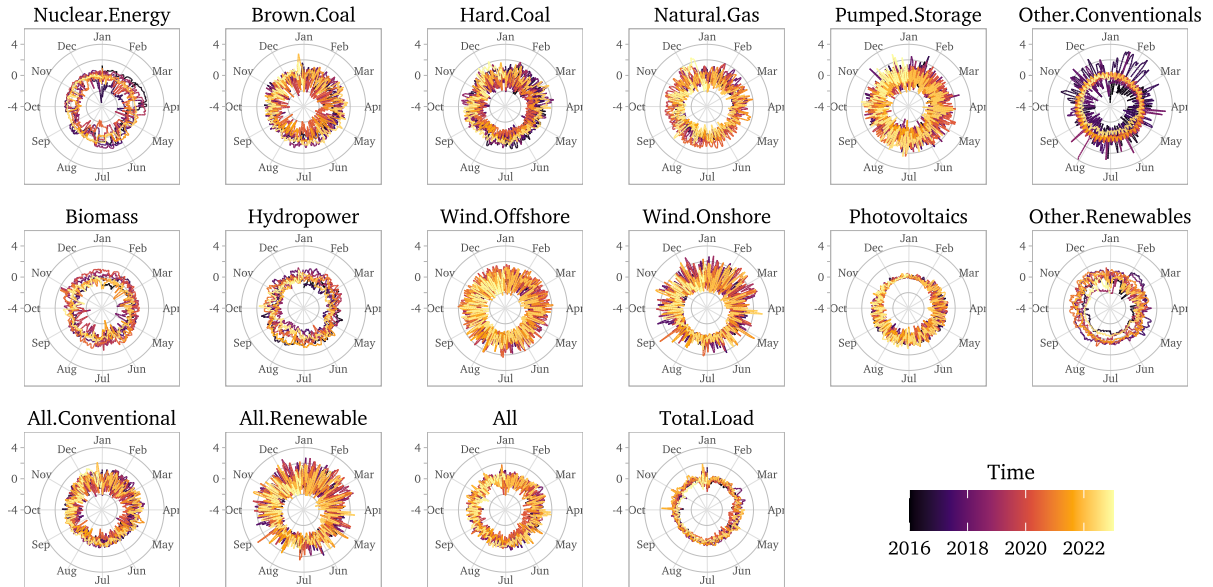


Figure 4.2: Circular plots for the development of power generation and consumption over time, after detrending.

e.g., outlined by [James et al., 2013](#)). Amongst all k values, the final detrending model for each series is chosen such that the Bayesian Information Criterion (defined in terms of RSS as, e.g., by [Greene, 2012](#)) is minimized, in order to ensure the sparsest regression setup possible for each series, while capturing its relevant detrending components.

The corresponding estimated x_t are then used as the detrended series, and again visualized in a circular plot in [Figure 4.2](#). In comparison to [Figure 4.1](#), the circles are generally closer to the desired centered circular shape, suggesting mostly stationary series and thus a reasonable base for analyzing their persistence in [Section 4.4](#). Before proceeding with the statistical analysis, however, light is shed on how the different trend and cycle patterns drive each of the series.

4.3.2 Temporal patterns and trends

While [Tables 4.3](#) and [4.4](#) in the appendix contain a full summary of the estimated coefficients from the regression model in [equation \(4.1\)](#), [Figure 4.3](#) visualizes the estimated linear and cyclical components of the detrending system for all series, without the weekday and holiday effects. The top plot refers to the aggregated generation and the consumption series, and thus highlights the general transition of the German energy market (although it has to be noted that the standardization mentioned in [Section 4.2](#) prevents direct comparison of the trends' levels and ranges). In terms of periodicity, a clear summer-winter pattern is observable in the electricity demand, which is generally matched by the conventional energy sources, but is gradually being replicated by the renewables. Regarding the temporal trends, this insight can be confirmed by the overall decrease of power gen-

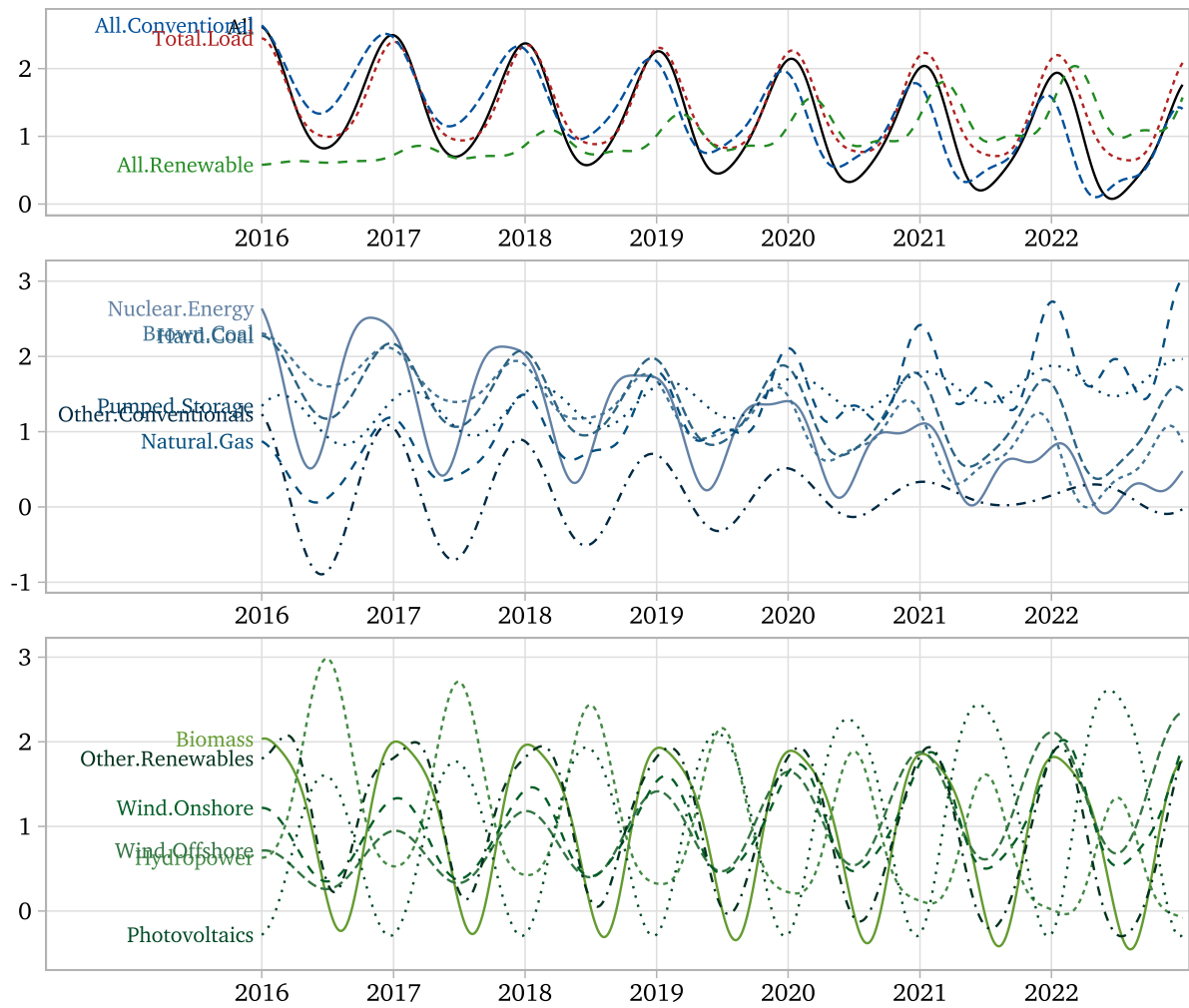


Figure 4.3: Estimated trends and cyclical components from the detrending regression (4.1). Top: Aggregated power generation and consumption. Middle: Conventional energy sources. Bottom: Renewable energy sources.

eration from the conventionals and increase of the renewable sources. In general, energy consumption has rather only decreased during summer and remains relatively stable over winter seasons. With both the original and detrended time series in view (see Figures 4.11 and 4.12 in the appendix), however, this observation can likely be explained by two external factors: the Covid-19 crisis that caused a nationwide shutdown of society and industry in spring and summer 2020 (Buechler et al., 2022), and the Russian invasion of Ukraine in 2022 which was followed by a general appeal to save energy (Bundesregierung, 2023). In comparison, the negative trend in total power generation presents itself as more credible, judged by the appearance of the corresponding original and detrended time series.

Considering the separate conventional and renewable sources as displayed in the center and bottom graphs of Figure 4.3, it becomes apparent that the relevance of the summer-winter pattern strongly depends on the respective energy source, as does the position of the seasonal peaks. For instance, the intermittent *Photovoltaics* generation has an anti-cyclic role in comparison to other renewable and the conventional energies, as it strongly

depends on the seasonally varying intensity of solar radiation. At the same time, *Natural.Gas* shows a shift towards a bimodal pattern, which can possibly be interpreted as a confirmation of its peak load role within the energy mix that applies in phases of high demand or low supply from the other energy sources, and further a pronounced positive trend reflecting its role as a bridge technology during the transition from conventionals to renewables. In contrast, the distinct negative trend of *Nuclear.Energy* and its flattening of seasonal peaks mirrors the gradual shutdown of nuclear plants and their decreasing importance in the energy mix. Similarly, a negative trend is apparent for *Hard.Coal* and *Brown.Coal*, which matches the patterns observed from the aggregated series. Regarding the general development of the renewables, the power generation from the intermittent energy sources *Wind.Offshore*, *Wind.Onshore*, and *Photovoltaics* has increased accordingly, while the other renewable sources have remained stable or slightly decreased over time.

Turning to the weekday and holiday effect represented by the binary variables D_{it} and H_{it} in equation (4.1), Figure 4.4 visualizes their estimated coefficients in form of a heat map. There, colored tiles represent deviations from the base volume on Mondays or on non-holidays, respectively. It becomes directly apparent that renewable energies do generally not depend on weekday and holiday effects, whereas the conventional energy production and the consumption have a strong seasonality in this sense. Whenever a

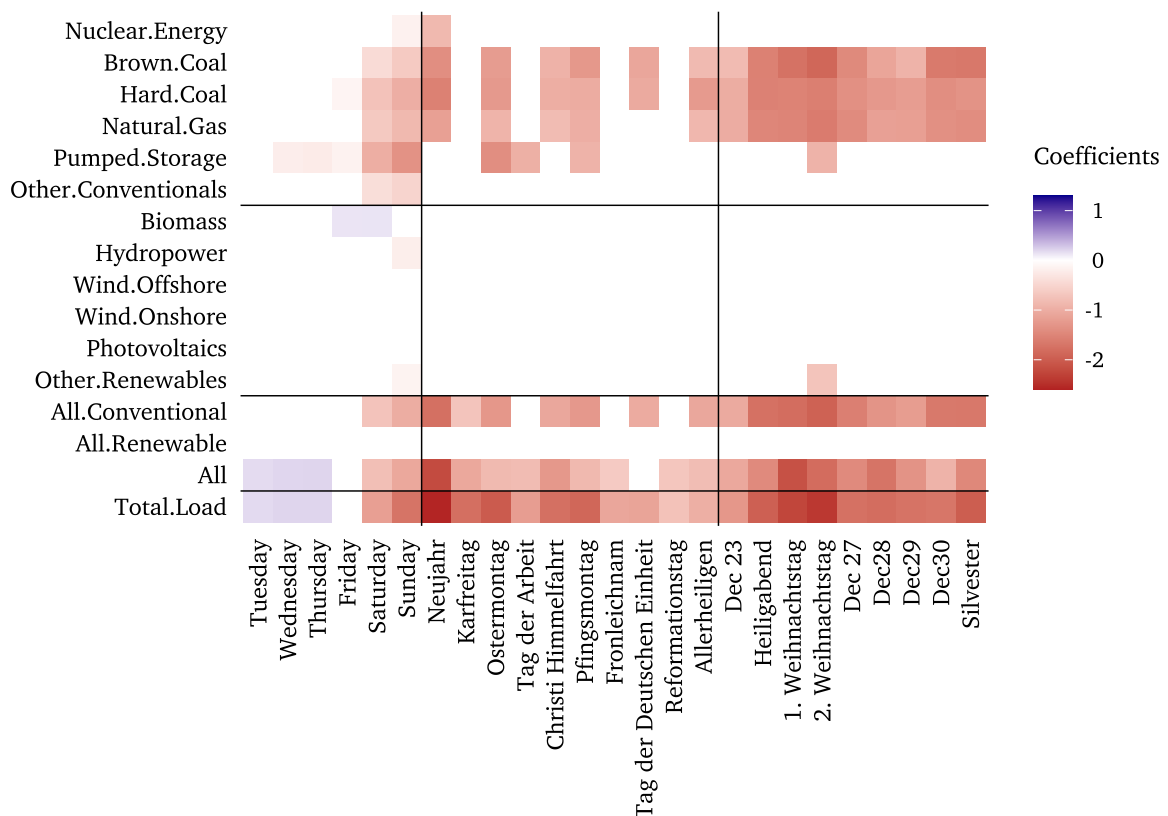


Figure 4.4: Heat map of the estimated weekday and holiday coefficients from the detrending regression (4.1).

weekday effect exists, the generic pattern is a lower power generation and consumption on the weekend, which is intensified for the total generation and consumption by an increased volume from Tuesdays to Thursdays, highlighting the overall weekday effect that drives the German electricity market. Deviations from the generic weekday effect can be found in the following series: *Nuclear.Energy* is barely reduced on the weekends, confirming its past role as a base load energy source that is not easily adjusted to demand peaks or generation shortages. *Pumped.Storage* is additionally reduced from Wednesdays to Fridays, which matches its purpose as a balancing instrument when power supply and demand deviate on the short-run. In contrast to the conventionals, the renewable sources show basically no weekday effect, although some coefficients were inexplicably estimated to be significantly different from 0: The use of *Biomass* is increased on Fridays and Saturdays, while *Hydropower* and *Other.Renewables* are slightly reduced on Sundays. Presumably, these peculiarities are related to nonstationarity properties of these series, as will be discussed in Section 4.4. As for the holiday effect, a similar pattern emerges, leaving the renewables with generally no dependence upon holidays, while the generation of most conventional sources and the consumption are strongly decreased compared to regular working days, especially around Christmas and New Year's Eve. However, for *Nuclear.Energy* and *Pumped.Storage* (and *Other.Conventionals*), this effect is negligible to non-existent, which can be attributed to their respective roles as either a base load source or a demand balancing instrument.

4.4 Fractional integration

After removing nonstationarity in form of linear and seasonal trends from the data, it is possible to analyze the power generation and consumption series univariately with respect to other nonstationarities and long-range dependence. The need for a model including fractional integration becomes apparent when applying common tests for stationarity and unit roots (Kwiatkowski et al., 1992; Dickey and Fuller, 1981), as both the $I(0)$ and the $I(1)$ null hypothesis, respectively, are rejected for all series at least at the 10% level (1% for most series). This section covers thorough estimation of the fractional order of integration $0 < d < 1$ and its interpretation for the German energy mix. More specifically, the commonly used local Whittle estimator is applied with a strategy for optimal bandwidth selection, and the possibilities of short-range dependent noise components and spurious long memory are investigated to minimize estimation uncertainty. Finally, a classification of the energy sources according to their memory parameter is provided.

4.4.1 Local Whittle estimation under optimal bandwidth selection

Long memory or long-range dependence refers to significant dependencies of time series observations across large time lags. The strength of the long-range dependence is described by the memory parameter d : For $d < 1/2$, the process is said to have stationary long memory, $d \geq 1/2$ describes nonstationary long memory, anti-persistence is given for $-1/2 < d < 0$, and $d = 0$ reduces to the case of a weakly dependent short memory process. A process is then defined to be fractionally integrated of type I if

$$x_t = (1 - L)^{-d} v_t, \quad (4.2)$$

where v_t is a stationary short memory sequence with continuous and bounded spectrum and infinite past (Marinucci and Robinson, 1999). Accordingly, the series x_t becomes $I(0)$ after fractional differencing of order d , where the fractional differencing operator is defined as

$$(1 - L)^d = \sum_{k=0}^{\infty} \pi_k(d) L^k = \sum_{k=0}^{\infty} \frac{\Gamma(k - d)}{\Gamma(-d)\Gamma(k + 1)} L^k \quad (4.3)$$

based on the Gamma function $\Gamma(\cdot)$. A stationary long memory process is characterized by a hyperbolic decay of the autocorrelation function $\gamma_x(k)$, $k \in \mathbb{Z}$, or, equivalently, a pole at the origin of the spectral density $f_x(\lambda) = \frac{1}{2\pi} \sum_{k=-\infty}^{\infty} \gamma_x(k) \exp(-ik\lambda)$, $\lambda \in [-\pi, \pi]$, of the underlying data generating process, formally described as

$$\begin{aligned} \gamma_x(k) &\sim L_\gamma(k) |k|^{2d-1} \quad \text{as } k \rightarrow \infty, \\ f_x(\lambda) &\sim L_f(\lambda) |\lambda|^{-2d} \quad \text{as } \lambda \rightarrow 0 \end{aligned} \quad (4.4)$$

with slowly varying functions $L_\gamma(k)$, $L_f(\lambda)$ (for details, see, e.g., the overview of Beran et al., 2013).

For estimation of the memory parameter d , a natural choice is the local Whittle estimator by Künsch (1987), which compares the periodogram I_x around the origin to the theoretical spectral density under long memory as stated in (4.4). It is defined as

$$\hat{d} = \arg \min_d R(d) \quad \text{for } R(d) = \log \left(\frac{1}{m} \sum_{j=1}^m \frac{I_x(\lambda_j)}{\lambda_j^{-2d}} \right) + \frac{1}{m} \sum_{j=1}^m \log \lambda_j^{-2d}, \quad (4.5)$$

based on $I_x(\lambda_j) = (2\pi T)^{-1} \left| \sum_{t=1}^T x_t \exp(-it\lambda) \right|^2$ evaluated at the Fourier frequencies $\lambda_j = \frac{2\pi j}{T}$ for the sample size T , where $j = 1, \dots, m$. In particular, the bandwidth m defines the degree of focus on the origin in the periodogram. Depending on the nature of the underlying stationary process v_t , the choice of bandwidth might largely affect the resulting

estimate of the memory parameter, as will be shown for the power series in Section 4.4.2. For instance, whenever higher-frequent short-range noise components are present, meaning v_t can be described as an ARMA(p, q) model with

$$\Phi(L)v_t = \Theta(L)\varepsilon_t, \quad (4.6)$$

where $\Phi(z) = 1 - \sum_{i=1}^p \phi_i z^i$ and $\Theta(z) = 1 - \sum_{j=1}^q \theta_j z^j$ and $\varepsilon_t \sim iid(0, \sigma_\varepsilon^2)$, the local Whittle estimate can be biased because the underlying long memory spectral density does not account for effects on these higher frequencies. Using a lower bandwidth for the estimation would reduce the bias from ARMA noise, but at the same time increase the variance due to the limited amount of information used in the estimation (Baillie and Kapetanios, 2009; Arteche and Orbe, 2017).

Instead of choosing a fixed bandwidth, it is therefore reasonable to apply a data-driven procedure for the bandwidth selection of each series.⁵ Arteche and Orbe (2017) propose such a technique, where a bootstrap approximation of the estimation mean squared error (MSE) is minimized to find the best bandwidth m^* and its corresponding local Whittle estimate \hat{d}^* . Starting from an initial low-bandwidth estimate of the memory parameter \hat{d} , the procedure is based on the locally standardized periodogram

$$\hat{v}(\lambda_j) = I_x(\lambda_j)\lambda_j^{2\hat{d}}. \quad (4.7)$$

There, the impact of possible long memory on the original periodogram ordinates is removed, in order to weaken the strong dependence structure that would contradict an application of any bootstrap method, and to make it resemble the periodogram of a weakly dependent series. Additionally, instead of applying the bootstrap to the scaled periodogram globally, the remaining weak dependence structure is accounted for by resampling its ordinates in a neighborhood around each of the Fourier frequencies. The range of the neighborhood is defined by the resampling width k_n that needs to be user-chosen, depending on the shape of the initial local periodogram and the resulting MSE. For each bootstrapped scaled periodogram, the long memory structure is then reintegrated via $\lambda_j^{-2\hat{d}}\hat{v}(\lambda_j)$, and the result is used for local Whittle estimation on a range of bandwidths. Comparing these bootstrapped memory estimates with the initial \hat{d} yields the MSE that is minimized to obtain the best bandwidth. As the result still depends on a possibly biased \hat{d} input, these steps are embedded in an iterative procedure where the estimates \hat{d} and

⁵ As stressed by Baillie et al. (2012), directly estimating the ARFIMA(p, d, q) model by Granger and Joyeux (1980) and Hosking (1981) can be advantageous over semiparametric methods like the local Whittle estimator. However, this approach is not followed here for two reasons. First, the comparison of Baillie et al. (2012) is based on the outdated optimal bandwidth by Henry (2001) that is rarely used by practitioners, and an analysis of the bootstrap technique by Arteche and Orbe (2017) is still pending. Second, in an attempted use of the ARFIMA model, the nonstationarity of some of the detrended power series caused misspecification issues that questioned the adequacy of a fully parametric approach.

\hat{v} are constantly updated with respect to the newest best bandwidth, stopping when the decrease of MSE compared to the previous best bandwidth is negligible.

4.4.2 Memory estimates for the energy mix

The need for a sophisticated choice of bandwidth when applying the local Whittle estimator to the detrended power generation and consumption series becomes apparent from Figure 4.5. There, local Whittle estimates are plotted for a range of commonly used bandwidths $m \in \{\lfloor T^{0.50} \rfloor = 50, \dots, \lfloor T^{0.75} \rfloor = 359\}$, with $\lfloor \cdot \rfloor$ returning the integer part of its argument. Especially for the *Nuclear.Energy* and *Biomass* series, different bandwidths result in a broad range of local Whittle estimates, from around 0.32 to 0.78 and from 0.33 to 0.62 for the two series, respectively, that would lead to very different conclusions on their memory properties.

Hence, to obtain reliable estimates for the memory of the power series, the optimal bandwidth selection as described in Section 4.4.1 is applied. Starting with an initial \hat{d} estimation based on the smallest bandwidth $m = \lfloor T^{0.50} \rfloor$, the MSE-optimal estimate \hat{d}^* is obtained from 1000 bootstrap replications. Since the choice of a suitable resampling width for each series is not obvious from the work of [Arteche and Orbe \(2017\)](#), the procedure is carried out for $k_n \in \{10, 20, 35, 50, 50, 75, 100, 150, \dots, 850\}$. The resulting local Whittle estimates \hat{d}^* for each k_n and their 90% bootstrap confidence intervals are displayed in Figure 4.6. For most series, the optimal-bandwidth memory estimate is stable

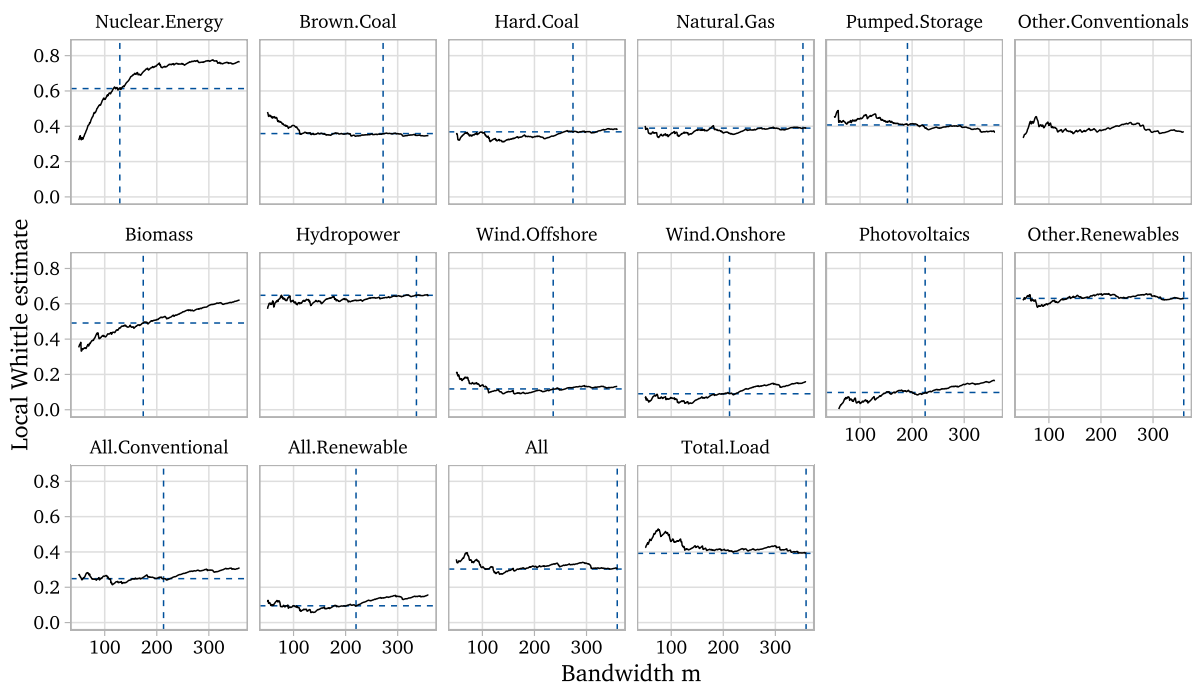


Figure 4.5: Local Whittle estimation as in (4.5) for different bandwidths m . Blue dashed lines indicate m^* and \hat{d}^* from the bootstrap bandwidth selection.

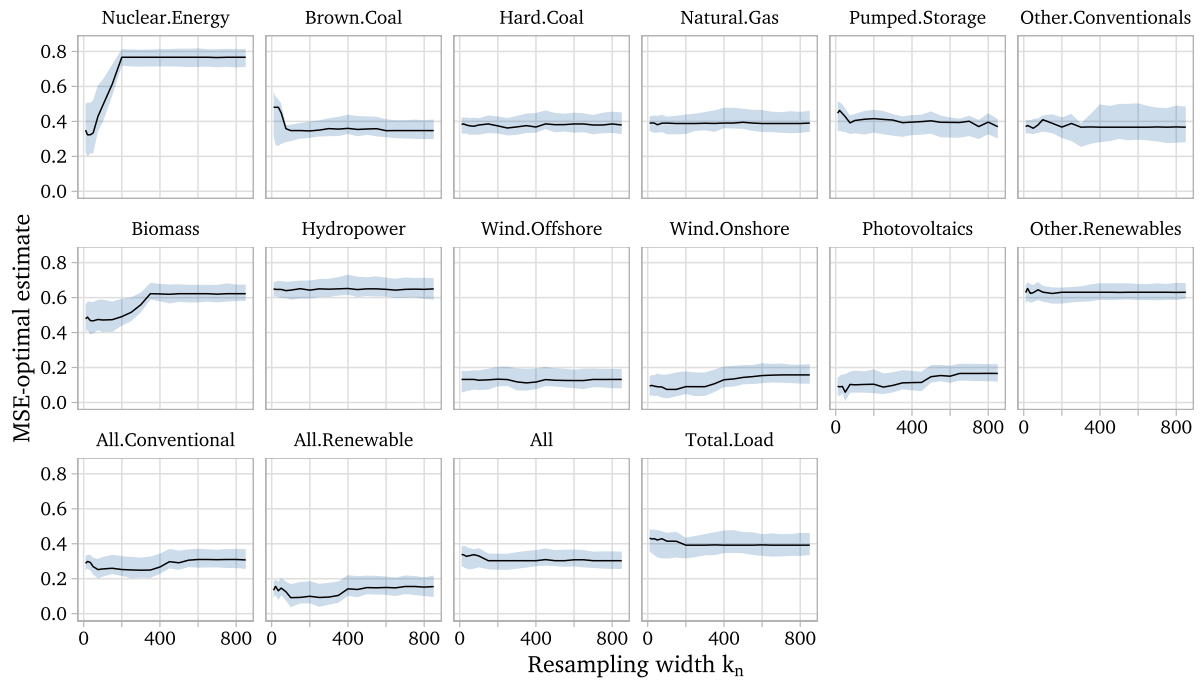


Figure 4.6: MSE-optimal local Whittle estimates for different resampling widths k_n according to the bandwidth selection strategy by [Arteche and Orbe \(2017\)](#). Blue bands represent the 90% bootstrap confidence interval.

across the range of resampling widths, except for the lower values of $k_n \leq 75$ that seem to be rather inappropriate for the given sample size and compared to the considered range of bandwidths. The series where the basic local Whittle estimate varied most with respect to the bandwidth, i.e. *Nuclear.Energy* and *Biomass*, are the most influenced by the choice of k_n .

For the final selection of k_n for each series, the resulting MSE of the last iteration is depicted in Figure 4.7 (for a reasonable choice of k_n values). First, the irregular shape of the MSE of *Other.Conventionals* for all resampling widths catches the eye, indicating that the applied procedure is not suited for the series. Judging from the appearance of the detrended series, it is subject to a persistence change or another form of structural break which prevents proper estimation of a single memory parameter, and is therefore dropped for the rest of the analysis. For most of the other series, a medium value of $k_n = 300$ produces a throughout reasonable shape of MSE and falls into the range of stable \hat{d}^* estimates, and is therefore fixed. However, confirming the picture from the previous plots, the two series *Nuclear.Energy* and *Biomass* require a more careful choice of the resampling width. In particular, their MSE shapes suggest lower values of k_n to obtain reasonable MSE minima, for which the reasons will be examined in Section 4.4.3. Considering the concurrent increase in MSE when reducing the resampling width, the respective values $k_n = 150$ and $k_n = 200$ are fixed as a trade-off.

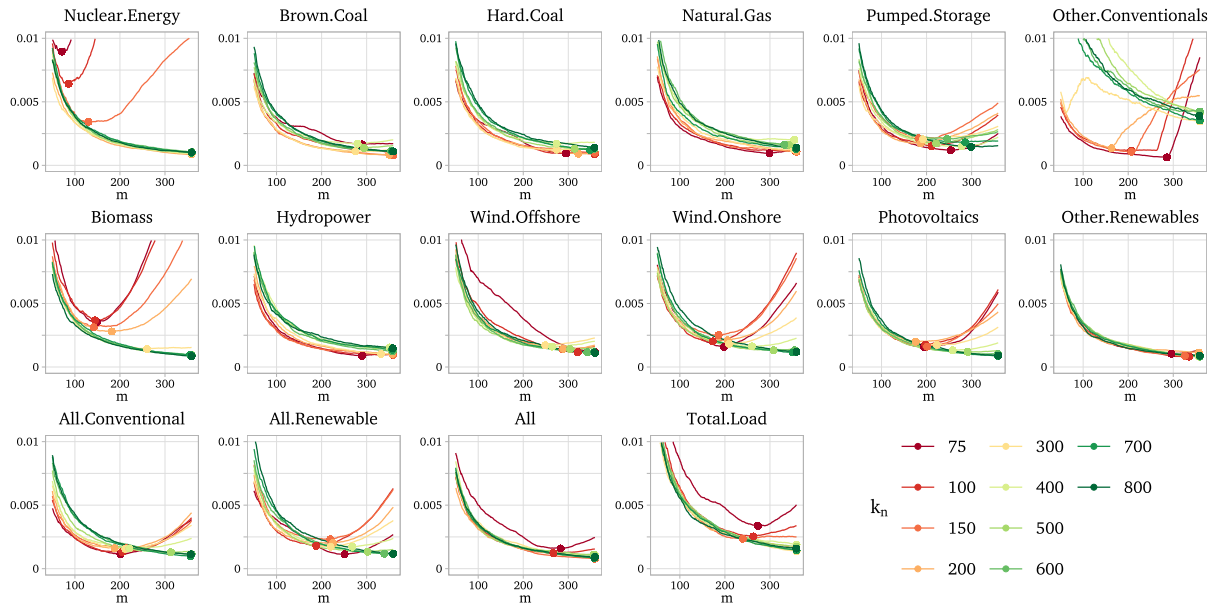


Figure 4.7: Bootstrap MSE of the bandwidth selection strategy by Arteche and Orbe (2017) depending on the bandwidth m and resampling width k_n .

Table 4.1 then summarizes the MSE-optimal bandwidths and the corresponding local Whittle estimates. For comparison, the naive local Whittle estimate for a fixed high bandwidth of $m = \lfloor T^{0.75} \rfloor$ is stated. In general, the estimates applying the MSE-optimal bandwidth are rather close to this naive local Whittle estimate. However, especially for *Nuclear.Energy* and *Biomass*, the choice of bandwidth has the expected large impact on the resulting memory estimate. To obtain a better understanding of the dynamics of the underlying process that complicate the local Whittle estimation and bandwidth selection, the following subsection addresses the possibility of spurious long memory and bias from short-range ARMA noise. An interpretation of the memory parameters is provided below in Section 4.4.4.

4.4.3 Spurious long memory and ARMA noise

As the local Whittle estimator is based on periodogram ordinates close to the origin, it can be upward biased in case of so-called spurious long memory, where low frequency contaminations such as level shifts or smooth trends falsely indicate long-range dependence. The distinction of true stationary long memory processes with spectral density as defined in equation (4.4) against the alternative of a process with low frequency contaminations can be achieved by means of the test of Qu (2011). Its test statistic compares periodogram ordinates close to the origin to the spectral density that would apply under a specific local Whittle estimate \hat{d} . Following the recommendations of Qu (2011), the applied bandwidth for the test is set to $m = \lfloor T^{0.70} \rfloor$. This results in four detections of spurious long memory that question the estimated memory parameters from Table 4.1: for the series

Table 4.1: Results of the MSE-optimal bandwidth selection and corresponding local Whittle estimates.

	k_n	m^*	$\hat{d}_{m^*}^*$	$CI_{0.95}(\hat{d}^*)$	$\hat{d}_{\lfloor T^{0.75} \rfloor}$
Nuclear.Energy	150	129 $\approx [T^{0.62}]$	0.6135	[0.5245, 0.7367]	0.7669
Brown.Coal	300	272 $\approx [T^{0.71}]$	0.3587	[0.3060, 0.4340]	0.3474
Hard.Coal	300	274 $\approx [T^{0.72}]$	0.3685	[0.3129, 0.4391]	0.3792
Natural.Gas	300	353 $\approx [T^{0.75}]$	0.3894	[0.3326, 0.4623]	0.3879
Pumped.Storage	300	191 $\approx [T^{0.67}]$	0.4075	[0.3032, 0.4562]	0.3675
Biomass	200	174 $\approx [T^{0.66}]$	0.4912	[0.4253, 0.6046]	0.6224
Hydropower	300	336 $\approx [T^{0.74}]$	0.6481	[0.5929, 0.7171]	0.6428
Wind.Offshore	300	236 $\approx [T^{0.70}]$	0.1179	[0.0569, 0.2055]	0.1320
Wind.Onshore	300	212 $\approx [T^{0.68}]$	0.0904	[0.0287, 0.1812]	0.1579
Photovoltaics	300	225 $\approx [T^{0.69}]$	0.0978	[0.0434, 0.1849]	0.1661
Other.Renewable	300	359 $\approx [T^{0.75}]$	0.6306	[0.5666, 0.6720]	0.6306
All.Conventional	300	213 $\approx [T^{0.68}]$	0.2488	[0.1947, 0.3321]	0.3101
All.Renewable	300	220 $\approx [T^{0.69}]$	0.0950	[0.0400, 0.1866]	0.1555
All	300	359 $\approx [T^{0.75}]$	0.3031	[0.2445, 0.3583]	0.3031
Total.Load	300	359 $\approx [T^{0.75}]$	0.3919	[0.3188, 0.4646]	0.3919

Nuclear.Energy, *Brown.Coal*, *Biomass*, and *Wind.Offshore*. Two of these four series stood out before due to a large variation of the local Whittle estimate and its bootstrap MSE with respect to the choices of bandwidth m and resampling width k_n .

However, as the test of Qu (2011) only detects deviations from the standard long memory spectral density, it can be distorted by short-range noise within the series, just like the local Whittle estimator. Qu (2011) therefore suggests to apply the test to pre-whitened series, where ARMA components for $p, q \leq 1$ are identified via estimation of an ARFIMA(p, d, q) model (Granger and Joyeux, 1980; Hosking, 1981) and the Akaike information criterion, and then removed from the series by using the corresponding ARMA(p, q) residuals. After pre-whitening, *Nuclear.Energy* and *Biomass* are no longer identified to exhibit spurious long memory. The evident presence of short-range noise components in these two series explains their particular shapes of MSE for different resampling widths and the need for low bandwidths, as were found by the bandwidth selection procedure. Consequently, their memory estimates as stated in Table 4.1 are assumed to be reliable. In contrast, spurious long memory in the two series *Brown.Coal* and *Wind.Offshore* is still confirmed after pre-whitening, suggesting a level shift or another form of structural break.

With both the pre-processed and detrended series in view (Figures 4.11 and 4.12), the presence of a level shift in *Brown.Coal* and a variance break in *Wind.Offshore* is quite possible (although it has to be noted that other series could similarly be subject to structural breaks, merely judging from their plots). For *Brown.Coal*, a decline of the electricity generation is apparent for the years 2019 and especially 2020, which can partially be linked to the Covid-19 crisis and the associated lockdown periods, resulting in a lower

electricity demand that apparently caused strong deviations from the regular use of brown coal. However, two tests for detecting potential level shifts in the presence of long memory (Shao, 2011; Iacone et al., 2014) denied the presence of mean breaks in any of the detrended power series. For *Wind.Offshore*, the plots instead suggest an increase of variance over time, which can be related to the general gain of importance of offshore wind parks, resulting in a higher absolute variation from the changed level.

For both series, relying on a different memory estimator that can account for low frequency contaminations would be an obvious choice. However, the allegedly suitable estimator by Hou and Perron (2014), which introduces a low-frequency component to the spectral density representation, involves the same or aggravated bandwidth selection problems as the local Whittle approach.⁶ Hence following the bandwidth recommendation of Hou and Perron (2014) with $m = \lfloor T^{0.80} \rfloor$ results in slightly higher memory estimates than d^* (0.3730 for *Brown.Coal* and 0.1826 for *Wind.Offshore*), which generally questions the benefits of increasing the flexibility in estimation by the additional low-frequency component. Furthermore, the effect of spurious long memory on the optimal bandwidth selection for the local Whittle estimator, i.e. on the local periodogram and the applied local bootstrap procedure, is yet to be assessed, which leaves the possibility that rather mild findings of spurious long memory have only negligible impact on the local Whittle estimation when selecting a suitable bandwidth. Based on the lack of evidence and alternatives for spurious long memory in this scenario, the optimal-bandwidth local Whittle estimates as stated in Table 4.1 are also maintained for these two series.

4.4.4 Implications of the memory estimates

Having a reliable estimate for the memory of power generation and consumption is not only relevant for proper fractional differencing as needed in Section 4.5, or for selecting suitable models in potential future research, but it can also provide valuable insights to the German energy mix, as the degree of long-range dependence reflects the stability and the effect of short-term adjustments of each energy source. Table 4.2 summarizes the estimated memory parameters for the power generation series, and three groups of persistence can be identified based on \hat{d}^* and their 95% bootstrap confidence intervals. The mildest form of long-range dependence is found for the three renewable energy sources that directly depend on the weather circumstances, i.e. both wind energy types and solar energy. Detrending with respect to temporal trends and seasonal patterns reveals an

⁶ An attempt to modify the strategy of Arteche and Orbe (2017), such that the low-frequency contaminations are included in the local periodogram, was not successful. Apparently, the greater flexibility caused by the additional parameter in the estimation by Hou and Perron (2014) causes irregular behavior of the MSE and therefore prevents a reliable minimization in the bootstrap procedure. Finding an elaborate bandwidth selection strategy for their estimator would therefore be an interesting subject for future research.

Table 4.2: Classification of the power sources according to the estimated memory parameter \hat{d}^* after MSE-optimal bandwidth selection.

	Conventional	Renewable
$0 < \hat{d}^* < 0.2$		Wind.Offshore Wind.Onshore Photovoltaics
$0.2 < \hat{d}^* < 0.5$	Brown.Coal Hard.Coal Natural.Gas Pumped.Storage	Biomass
$0.5 < \hat{d}^* < 0.7$	Nuclear.Energy	Hydropower Other.Renewable

underlying process with low but existing autocorrelation over distant observations. Compared to the higher persistence of the other generation series, this matches the general characteristic of those three sources to be intermittent and rather unreliable. While providing a valuable contribution to the German energy mix and the transition to renewable energies, this emphasizes the need for careful replacement of the conventional energy sources in order to guarantee a secure energy supply.

In contrast, the majority of energy sources can be assigned to the range of medium to high stationary long memory. This is explained by the comparably higher stability of energy supply from the conventional sources but also from *Biomass*, which confirms its potential role as a base load source and thus its importance in the transition towards renewable energies. Showing an even higher degree of persistence, three series were identified to lie in the nonstationary range of long memory.⁷ Regarding *Hydropower* and *Other.Renewables*, the considerably higher memory estimate can presumably be attributed to aggregation or mixture effects, as both series are built from combinations of very different energy sources. For *Hydropower* in particular, water-storage power generation plants are rather used for peak load energy supply and therefore reasonably associated with a lower memory parameter, while run-of-river plants provide base load energy and are likely linked to the commonly known high memory of rivers themselves. In contrast, the high memory estimate of *Nuclear.Energy* can be explained by its low short-term variations and its appearance to be almost piecewise constant, which is related to complicated control systems of nuclear power plants and the associated rare adjusting to demand fluctuations. Thus, a more sophisticated model with, for example, nonlinear components might be worth considering for this series.

⁷ Note that consistency and asymptotic normality of the local Whittle estimation is still proven for the given nonstationary values of \hat{d}^* (Velasco, 1999; Phillips and Shimotsu, 2004; Shao and Wu, 2007) and confirmed for its bootstrap characteristics (Arteche and Orbe, 2016).

The memory parameters of the aggregated power generation series and the total consumption are estimated to substantially lower values than the separate power sources. However, with $\hat{d}^* = 0.0950$ for the renewables and $\hat{d}^* = 0.2488$ for the conventional energy sources, the renewable energies seem to have a lower persistence overall, driven by the high share of intermittent wind and solar energy sources. The higher memory estimates for total consumption and the demand are likely explained by the effect of aggregation within the whole German electricity market. As a general implication from long memory in the underlying processes of the power generation series, one can conclude that external events have a persisting effect on the energy mix. Consequently, this suggests that in the transformation towards renewable energies, even small or temporary steps in replacing the conventional energy sources might have a lasting effect on the German energy mix and support the shutdown of high emission power generation.

4.5 Interdependencies and a multivariate perspective

So far, this paper provided a solely univariate analysis of the trends and memory properties of the different power generation series. The contribution of each energy source to the German energy mix is hardly managed univariately, though, but subject to a complex supply planning system. In this section, a first step in the multivariate direction is made, in order to assess the interdependencies of the energy sources and to give directions for future research on the German energy mix. As all series feature fractional integration, a multivariate model allowing for fractional cointegration could be suitable, where time series of equal memory possibly follow a common trend of lower fractional integration order (for overviews, see, e.g., [Leschinski et al., 2021](#); [Hualde and Nielsen, 2022](#)). However, there are several difficulties involved in this approach. First, established semiparametric models as, e.g., the one introduced by [Souza et al. \(2018\)](#) require a common bandwidth in the memory estimation, which contradicts the results of Section 4.4. Then, even when relying on a uniform bandwidth of $m = \lfloor T^{0.75} \rfloor$ for the cointegration model, no fractional cointegration relation could be detected within those power generation series of equal integration order with the applied methodology. Restricting the scope of this paper, the search for a suitable model involving fractional cointegration or another type of interdependencies between the different fractionally integrated power sources is left for future research.

Nevertheless, in order to gain first insights on the multivariate structures of the power data set, the cross-correlation of the series is examined. More precisely, cross-correlograms of all combinations of the remaining eleven energy sources were generated, as they provide insights on the linear interdependencies of the series across different points in time. Interestingly, the univariate detrending and adjacent fractional differencing with the esti-

mated memory parameters \hat{d}^* result in almost all autocorrelations and cross-correlations for lags greater than zero being fully erased. The remaining basic correlations without temporal shifts are visualized in Figure 4.8.

Noticeably, the direction of correlations is divided into two groups. While the intermittent and lower-persistence wind energy sources are positively correlated with each other, they show strong negative dependencies with all other series. Similarly, the third intermittent source *Photovoltaics* shows no or negative correlation to all other energy sources, reflecting its anticyclic role in the energy mix. As these three energy types form the main contributors to the renewable energies, the same holds for the aggregated series *All.Renewables*. The remaining renewable sources, i.e. *Biomass*, *Hydropower*, and *Other.Renewables*, show positive correlations with the conventional energies, suggesting that these energy types are more likely able to mimic the supply pattern of the conventionals. Hence, they can make a valuable contribution to the general transition towards a renewable energy mix, whereas wind and solar energy have limitations in this regard. It has to be noted, however, that this conclusion is drawn only from daily time series, while considering intraday patterns could further add to understanding the possible substitutions in the energy market. Turning to the conventionals, the strongest correlations are found in the main sources *Brown.Coal*, *Hard.Coal*, and *Natural.Gas*. Amongst these, *Brown.Coal* has the highest correlation with *Nuclear.Energy*, which can be related to their

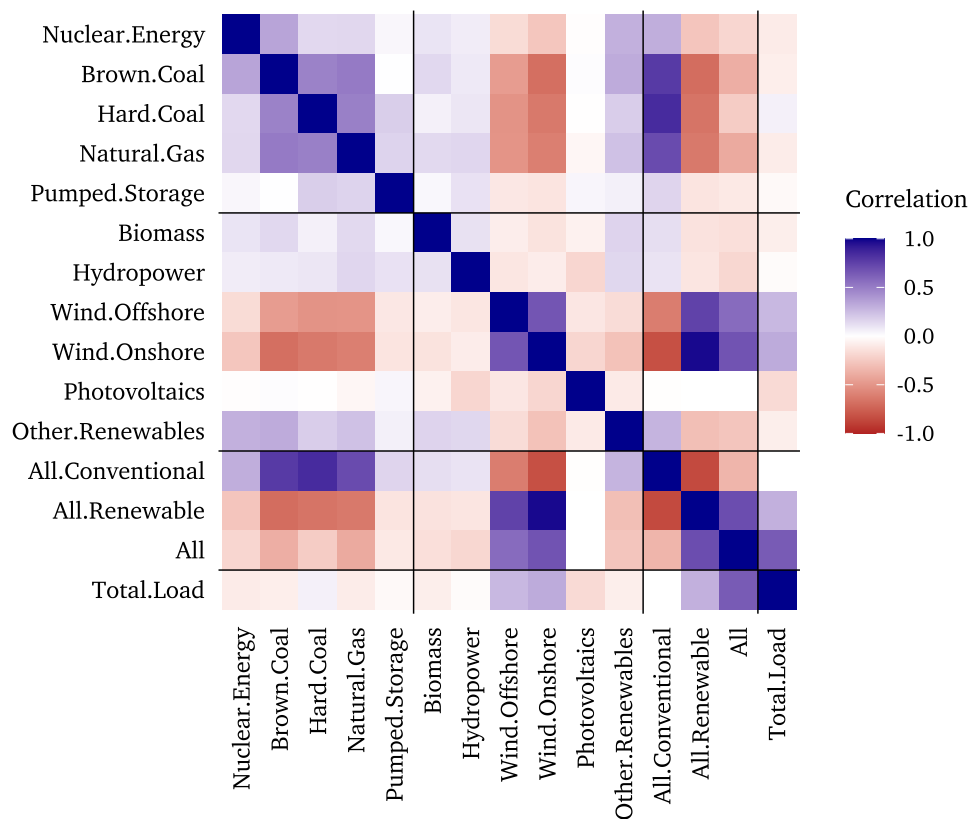


Figure 4.8: Correlation coefficients for the detrended and fractionally differenced series.

roles as base load power sources. Unexpectedly, there is a strong positive linear dependence of *Natural.Gas* with *Brown.Coal* and *Hard.Coal*, which contradicts its role as a peak load and bridge technology, as both would involve a stable or increasing use of power from *Natural.Gas* during the gradual shutdown of coal-powered plants. Considering the energy demand, the picture is more heterogeneous. Positive correlations are found with *Hard.Coal*, *Wind.Offshore* and *Wind.Onshore*, whereas the other energy sources are slightly negatively correlated to the *Total.Load* series. However, an explanation for these findings is yet to be found. Additionally, a more sophisticated approach to assessing the interdependencies of the power generation series is still required to allow for more reliable interpretations of the multivariate properties.

To illustrate the impact of trends, seasons and univariate autocorrelation, Figure 4.10 in the appendix additionally shows the correlations for the pre-processed series. Mainly driven by the seasonal trends of the energy sources, these correlations paint a slightly different picture of their linear interdependencies. In particular, the shared seasonal pattern of *Hydropower* and *Photovoltaics* gives the appearance of a stronger positive correlation between the two series and a more distinct separation from all other energy sources. Similarly, deviations in the results for *Biomass* and *Other.Renewables* cause a generally more heterogeneous picture within the renewable energies, and *Nuclear.Energy* appears to be disrupt the homogeneity of the conventional sources. Most striking, however, is the seemingly different role of the conventional and renewable energies for the total power generation: when only considering the pre-processed series, the correlations for the overall generation suggest a positive link with all sources that actually just share a more or less similar summer-winter pattern in the seasonal structure. The differences in the results compared to the detrended and fractionally differenced series highlight the relevance of the applied univariate modeling strategy and the importance of incorporating its findings into a multivariate model.

4.6 Conclusion

In this paper, the daily power generation from Germany's twelve energy sources and total consumption in the years 2016 to 2022 is investigated, in order to contribute to the understanding of the German energy mix and its implications for the transition towards renewable energies. In a univariate setting, each power source is analyzed with respect to seasonal patterns and temporal trends based on a detrending scheme that was specifically tailored to the German energy market. As the detrended series feature long-range dependence, a reliable memory estimate for each of the series is provided, which is based on the well-established local Whittle approach and accounts for estimation uncertainty regarding the choice of bandwidth and possible bias from spurious long memory and ARMA noise.

Seeing behind the univariate seasons, trends, and fractional integration, a first step in the multivariate direction is made, where the interdependencies of the twelve energy sources are explained based on simple correlations of the detrended and differenced series.

The applied methods outline a modeling approach that handles the peculiarities of each of the power generation and consumption series, and thereby provide insights into the composition of the German energy mix over time. As the conventional energy sources show a characteristic annual and weekly pattern that is closely linked to the demand, the need for a careful combination of renewable energies in order to guarantee a secure and reliable power supply in Germany becomes apparent. This is confirmed by three ranges of long-range dependence that drive the twelve energy sources and reflect their stability in the power generation: low persistence for the major renewable sources that provide an intermittent supply ($0 < \hat{d}^* < 0.2$), pronounced long memory properties for the base load and peak load sources ($0.2 < \hat{d}^* < 0.5$), and nonstationary long memory for the rarely adjustable base load or aggregated power sources ($0.5 < \hat{d}^* < 0.7$). The unique role of the intermittent wind and solar energy sources is further highlighted in the multivariate setting, as these are found to be negatively correlated with the other series, despite of their importance in the transition towards renewable energies. In summary, this emphasizes the difficulties in replacing the conventional energy sources with a system of renewables that provides the same capacity, reliability and controllability as the current energy mix.

While the obtained results convincingly reflect the dynamics of the German energy mix, each step of the methodology bears potential for future work. First, the energy supply is generally regulated at a higher frequency than what the daily data covers. Basing a similar analysis on 15 minute interval data and accounting for intraday seasonality could further contribute to understanding the substitution effects between conventional and renewable energies. Similarly, the proposed detrending scheme does not consider any variations in the seasonality and trends, although the ongoing transformation of the energy market and potential introduction of new technologies to the energy mix will likely contradict the validity of a fixed-parameter setting when future data is added to the sample. Considering the memory estimation, the application to the power generation series recalled well-known challenges regarding the bandwidth selection, and revealed the need for extending the framework of [Arteche and Orbe \(2017\)](#) to spurious long memory. Finally, the correlation analysis was only a first step towards a multivariate framework. A model that incorporates the findings on seasonality and persistence of the univariate series and simultaneously captures their interdependencies could offer further insights on the peculiarities of the German energy mix and opportunities for replacing conventional energies in the long run. For instance, the multivariate unobserved components approach as described by [Hartl and Jucknewitz \(2022\)](#) could capture the different degrees of fractional integration and allow for cointegration between the energy sources, while verifying the different characteristics of the power sources with help of a factor model formulation.

4.A Appendix

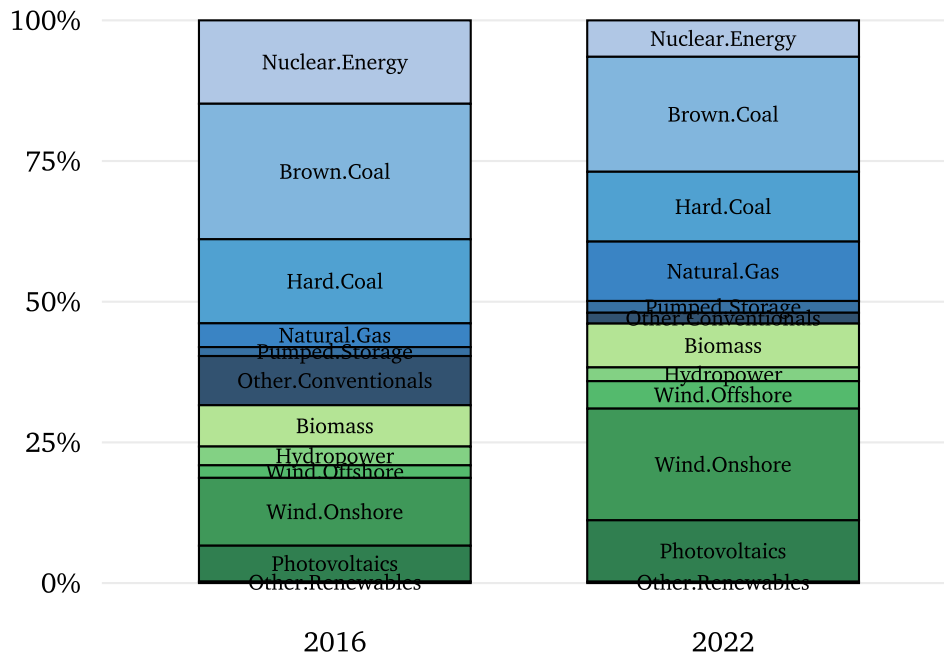


Figure 4.9: Composition of the German energy mix in 2016 and 2022.

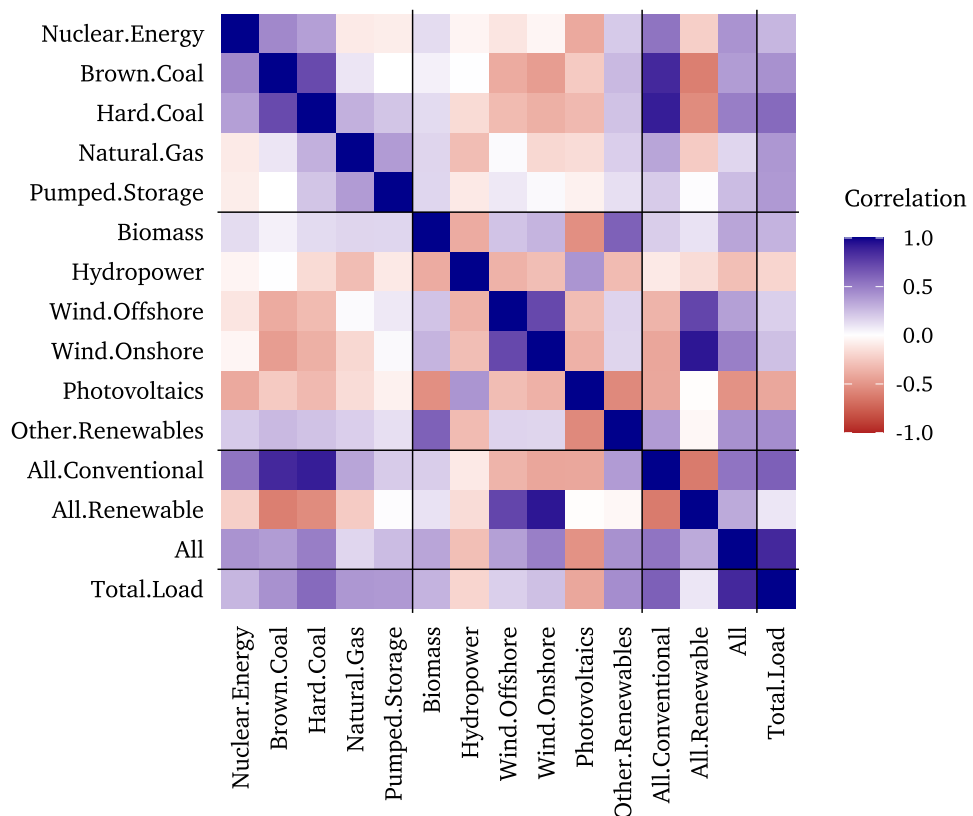


Figure 4.10: Correlation coefficients for the pre-processed series.

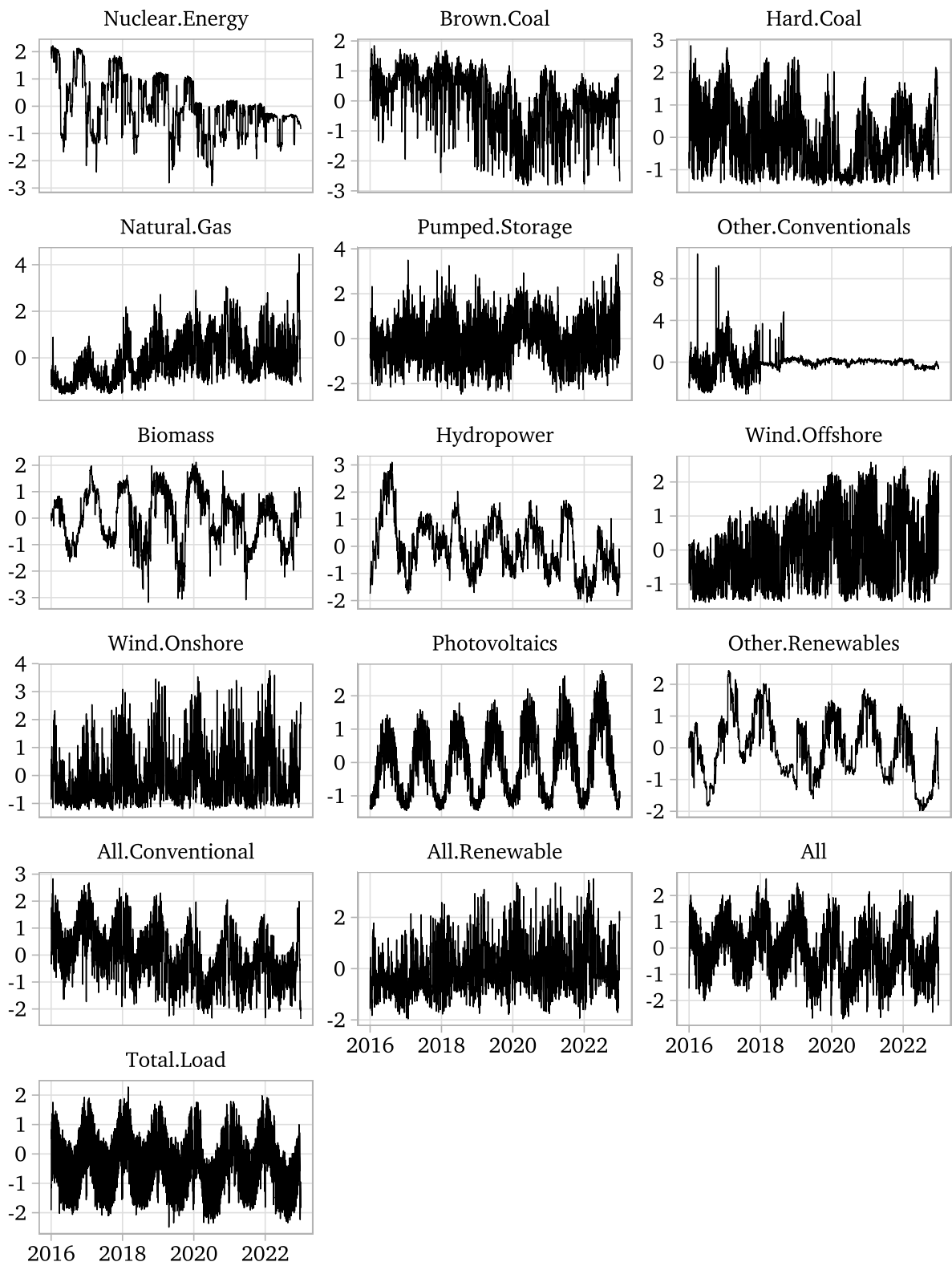


Figure 4.11: Power consumption and generation time series after pre-processing.

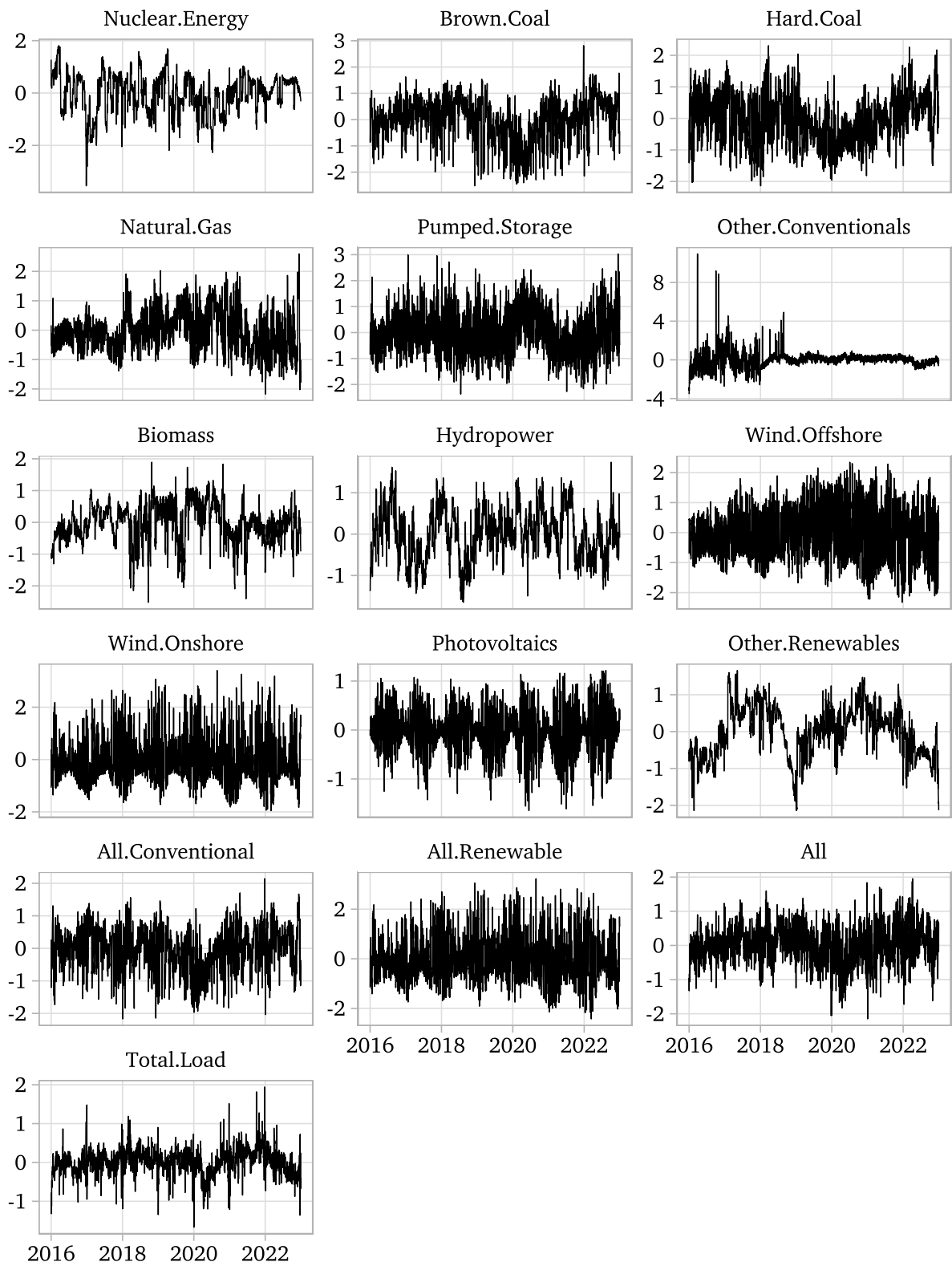


Figure 4.12: Power consumption and generation time series after detrending.

Table 4.3: Estimated coefficients for the trend and cycle components in the detrending regression (4.1). The close-to-zero coefficient estimates for the trend and its interaction terms are due to the large number of observations $T = 2557$ and the corresponding high values of the trend variable t , but are significantly different from zero.

	constant	trend	annual cycle				semi-annual cycle			
	$\hat{\beta}_0$	$\hat{\beta}_1$	$\hat{\alpha}_{\sin,1}$	$\hat{\alpha}_{\cos,1}$	$\hat{\gamma}_{\sin,1}$	$\hat{\gamma}_{\cos,1}$	$\hat{\alpha}_{\sin,2}$	$\hat{\alpha}_{\cos,2}$	$\hat{\gamma}_{\sin,2}$	$\hat{\gamma}_{\cos,2}$
Nuclear.Energy	0.88	-0.00065	-0.85	0.77	0.00035	-0.00020	0.19			
Brown.Coal	1.01	-0.00063		0.30	-0.00018				-0.00004	0.00007
Hard.Coal	0.75	-0.00034		0.53	-0.00013					0.00006
Natural.Gas	-0.58	0.00067	-0.18	0.46	0.00013					0.00017
Pumped.Storage	0.11	0.00025	0.29	0.22	-0.00013					
Other.Conventionals	0.14		-0.28	1.09	0.00018	-0.00050				
Biomass	0.09	-0.00010	0.57	0.94			-0.22			
Hydropower	0.69	-0.00051		-1.25	-0.00004	0.00024		0.19		
Wind.Offshore	-0.53	0.00042		0.24		0.00022				
Wind.Onshore	-0.22	0.00018		0.44	0.00013	0.00010			0.00006	
Photovoltaics	-0.38	0.00030	0.13	-0.90	0.00007	-0.00022				-0.00008
Other.Renewables	0.37	-0.00027	0.38	0.70		0.00015	-0.15	-0.28	0.00011	0.00014
All.Conventional	1.05	-0.00058	-0.23	0.59						0.00010
All.Renewable	-0.42	0.00034			0.00019	0.00011			0.00006	-0.00006
All	0.68	-0.00033	-0.10	0.86	0.00010			0.07	0.00006	
Total.Load	0.61	-0.00014		0.71	0.00012			0.12	0.00004	

Table 4.4: Estimated coefficients for the binary weekday and holiday indicators in the detrending regression (4.1).

	Tuesday $\hat{\phi}_1$	Wednesday $\hat{\phi}_2$	Thursday $\hat{\phi}_3$	Friday $\hat{\phi}_4$	Saturday $\hat{\phi}_5$	Sunday $\hat{\phi}_6$	Neujahr $\hat{\eta}_1$	Karfreitag $\hat{\eta}_2$	Ostermontag $\hat{\eta}_3$	Tag der Arbeit $\hat{\eta}_4$	Christi Himmelfahrt $\hat{\eta}_5$	Pfingstmontag $\hat{\eta}_6$	
Nuclear.Energy						-0.16	-0.86						
Brown.Coal					-0.44	-0.65	-1.39		-1.22		-0.95	-1.28	
Hard.Coal				-0.13	-0.74	-1.00	-1.56		-1.26		-1.00	-1.03	
Natural.Gas					-0.67	-0.86	-1.18		-0.92		-0.82	-1.00	
Pumped.Storage		-0.21	-0.24	-0.16	-1.00	-1.35			-1.40	-0.98		-0.94	
Other.Conventionals					-0.41	-0.53							
Biomass				0.13	0.13								
Hydropower						-0.21							
Wind.Offshore													
Wind.Onshore													
Photovoltaics													
Other.Renewables						-0.14							
All.Conventional					-0.74	-1.01	-1.77	-0.73	-1.29		-1.09	-1.27	
All.Renewable													
All	0.17	0.20	0.20		-0.79	-1.08	-2.21	-1.08	-0.85	-0.82	-1.28	-0.86	
Total.Load	0.18	0.20	0.20		-1.18	-1.72	-2.58	-1.78	-2.02	-1.21	-1.77	-1.88	
	Fronleichnam $\hat{\eta}_7$	Tag der Deutschen Einheit $\hat{\eta}_8$	Reformationstag $\hat{\eta}_9$	Allerheiligen $\hat{\eta}_{10}$	Dec 23 $\hat{\eta}_{11}$	Heiligabend $\hat{\eta}_{12}$	1. Weihnachtstag $\hat{\eta}_{13}$	2. Weihnachtstag $\hat{\eta}_{14}$	Dec 27 $\hat{\eta}_{15}$	Dec 28 $\hat{\eta}_{16}$	Dec 29 $\hat{\eta}_{17}$	Dec 30 $\hat{\eta}_{18}$	Silvester $\hat{\eta}_{19}$
Nuclear.Energy													
Brown.Coal		-1.09		-0.85	-0.83	-1.57	-1.75	-1.88	-1.45	-1.11	-0.93	-1.65	-1.67
Hard.Coal		-1.04		-1.25	-1.02	-1.56	-1.54	-1.59	-1.38	-1.27	-1.21	-1.40	-1.34
Natural.Gas				-0.88	-1.02	-1.50	-1.52	-1.63	-1.43	-1.17	-1.18	-1.38	-1.41
Pumped.Storage								-0.94					
Other.Conventionals													
Biomass													
Hydropower													
Wind.Offshore													
Wind.Onshore													
Photovoltaics													
Other.Renewables								-0.73					
All.Conventional		-1.04		-1.09	-1.05	-1.76	-1.81	-1.94	-1.58	-1.33	-1.22	-1.66	-1.67
All.Renewable													
All	-0.65		-0.70	-0.81	-1.08	-1.45	-2.14	-1.82	-1.45	-1.72	-1.33	-0.93	-1.48
Total.Load	-1.09	-1.13	-0.75	-0.99	-1.29	-1.96	-2.27	-2.40	-1.76	-1.81	-1.73	-1.70	-1.99

CHAPTER 5

Real Exchange Rates and Fundamentals in a New Markov-STAR Model

Co-authored with Philip Bertram, Jun Ma, and Philipp Sibbertsen.

Published in Oxford Bulletin of Economics and Statistics (2021), 84(2):356–379.

<https://doi.org/10.1111/obes.12467>

References

- Adedoyin, F., Ozturk, I., Abubakar, I., Kumeka, T., Folarin, O. and Bekun, F. V. (2020). Structural breaks in CO₂ emissions: Are they caused by climate change protests or other factors?, *Journal of Environmental Management* **266**: 110628.
- Adler, R. F., Gu, G., Sapiano, M., Wang, J.-J. and Huffman, G. J. (2017). Global precipitation: Means, variations and trends during the satellite era (1979–2014), *Surveys in Geophysics* **38**(4): 679–699.
- Ailliot, P. and Monbet, V. (2012). Markov-switching autoregressive models for wind time series, *Environmental Modelling & Software* **30**: 92–101.
- Allan, R. P., Liu, C., Zahn, M., Lavers, D. A., Koukouvagias, E. and Bodas-Salcedo, A. (2014). Physically consistent responses of the global atmospheric hydrological cycle in models and observations, *Surveys in Geophysics* **35**(3): 533–552.
- Anghileri, D., Pianosi, F. and Soncini-Sessa, R. (2014). Trend detection in seasonal data: From hydrology to water resources, *Journal of Hydrology* **511**: 171–179.
- Antweiler, W. and Muesgens, F. (2021). On the long-term merit order effect of renewable energies, *Energy Economics* **99**: 105275.
- Arteche, J. and Orbe, J. (2016). A bootstrap approximation for the distribution of the local Whittle estimator, *Computational Statistics & Data Analysis* **100**: 645–660.
- Arteche, J. and Orbe, J. (2017). A strategy for optimal bandwidth selection in local Whittle estimation, *Econometrics and Statistics* **4**: 3–17.
- Auguie, B. and Antonov, A. (2017). gridExtra: Miscellaneous functions for “grid” graphics, <https://cran.r-project.org/package=gridExtra>.
- Bacro, J.-N., Gaetan, C., Opitz, T. and Toulemonde, G. (2020). Hierarchical space-time modeling of asymptotically independent exceedances with an application to precipitation data, *Journal of the American Statistical Association* **115**(530): 555–569.
- Baillie, R. T. and Kapetanios, G. (2009). Semi parametric estimation of long memory: Comparisons and some attractive alternatives. Unpublished Manuscript.
- Baillie, R. T., Kongcharoen, C. and Kapetanios, G. (2012). Prediction from ARFIMA models: Comparisons between MLE and semiparametric estimation procedures, *International Journal of Forecasting* **28**(1): 46–53.
- Belda, M., Holtanová, E., Halenka, T. and Kalvová, J. (2014). Climate classification revisited: From Köppen to Trewartha, *Climate Research* **59**(1): 1–13.
- Beran, J. (1994). *Statistics for long-memory processes*, Vol. 61 of *Monographs on Statistics and Applied Probability*, Chapman & Hall, New York.

- Beran, J. and Feng, Y. (2002). SEMIFAR models – A semiparametric approach to modelling trends, long-range dependence and nonstationarity, *Computational Statistics & Data Analysis* **40**(2): 393–419.
- Beran, J., Feng, Y., Ghosh, S. and Kulik, R. (2013). *Long-Memory Processes: Probabilistic Properties and Statistical Methods*, Springer, Berlin Heidelberg.
- Bergman, U. M. and Hansson, J. (2005). Real exchange rates and switching regimes, *Journal of International Money and Finance* **24**: 121–138.
- Berrocal, V. J., Raftery, A. E. and Gneiting, T. (2008). Probabilistic quantitative precipitation field forecasting using a two-stage spatial model, *The Annals of Applied Statistics* **2**(4): 1170–1193.
- Bertolacci, M., Cripps, E., Rosen, O., Lau, J. W., Cripps, S. et al. (2019). Climate inference on daily rainfall across the Australian continent, 1876–2015, *The Annals of Applied Statistics* **13**(2): 683–712.
- Bhend, J. and von Storch, H. (2008). Consistency of observed winter precipitation trends in northern Europe with regional climate change projections, *Climate Dynamics* **31**(1): 17–28.
- Bindoff, N. L., Stott, P. A., AchutaRao, K. M., Allen, M. R., Gillett, N., Gutzler, D., Hansingo, K., Hegerl, G., Hu, Y., Jain, S. et al. (2013). Detection and attribution of climate change: From global to regional. Chapter 10, *Climate Change 2013: The Physical Science Basis. Contribution of Working Group I to the Fifth Assessment Report of the Intergovernmental Panel on Climate Change*, Cambridge University Press.
- Bivand, R. S., Pebesma, E. and Gómez-Rubio, V. (2013). *Applied Spatial Data Analysis with R*, Second Edition, Springer, New York.
- Böhringer, C., Cantner, U., Costard, J., Kramkowski, L.-V., Gatzert, C. and Pietsch, S. (2020). Innovation for the German energy transition – Insights from an expert survey, *Energy Policy* **144**: 111611.
- Bonato, M., Cepni, O., Gupta, R. and Pierdzioch, C. (2023). Climate risks and realized volatility of major commodity currency exchange rates, *Journal of Financial Markets* **62**: 100760.
- Bopp, G. P., Shaby, B. A. and Huser, R. (2021). A hierarchical max-infinitely divisible spatial model for extreme precipitation, *Journal of the American Statistical Association* **116**(533): 93–106.
- Breslin, M. and Belward, J. (1999). Fractal dimensions for rainfall time series, *Mathematics and Computers in Simulation* **48**(4-6): 437–446.
- Buechler, E., Powell, S., Sun, T., Astier, N., Zanocco, C., Bolorinos, J., Flora, J., Boudet, H. and Rajagopal, R. (2022). Global changes in electricity consumption during COVID-19, *IScience* **25**(1): 103568.
- Buishand, T. (1978). Some remarks on the use of daily rainfall models, *Journal of Hydrology* **36**(3-4): 295–308.

- Bunde, A., Büntgen, U., Ludescher, J., Luterbacher, J. and Von Storch, H. (2013). Is there memory in precipitation?, *Nature Climate Change* **3**(3): 174–175.
- Bundesregierung (2022). EEG 2023 - “We’re tripling the speed of the expansion of renewable energies”, retrieved June 1, 2023, from <https://www.bundesregierung.de/breg-de/themen/klimaschutz/amendment-of-the-renewables-act-2060448>.
- Bundesregierung (2023). Maßnahmen zum Energiesparen, retrieved June 12, 2023, from <https://www.bundesregierung.de/breg-de/themen/klimaschutz/energiesparmassnahmen-2078224>.
- Büntgen, U., Tegel, W., Nicolussi, K., McCormick, M., Frank, D., Trouet, V., Kaplan, J. O., Herzig, F., Heussner, K.-U., Wanner, H. et al. (2011). 2500 years of European climate variability and human susceptibility, *Science* **331**(6017): 578–582.
- Busch, M. and Sibbertsen, P. (2018). An overview of modified semiparametric memory estimation methods, *Econometrics* **6**(1): 13.
- Castle, J. L., Hendry, D. F. et al. (2020). Climate econometrics: An overview, *Foundations and Trends in Econometrics* **10**(3-4): 145–322.
- Chavez-Demoulin, V., Davison, A. C. and McNeil, A. J. (2005). Estimating value-at-risk: A point process approach, *Quantitative Finance* **5**(2): 227–234.
- Cohn, T. A. and Lins, H. F. (2005). Nature’s style: Naturally trendy, *Geophysical Research Letters* **32**(23).
- Dagum, E. B. and Bianconcini, S. (2016). *Seasonal Adjustment Methods and Real Time Trend-Cycle Estimation*, Springer Series in Statistics, Springer International Publishing Switzerland.
- Davidson, J. and Sibbertsen, P. (2005). Generating schemes for long memory processes: Regimes, aggregation and linearity, *Journal of Econometrics* **128**(2): 253–282.
- Di Lorenzo, P. (2022). usmap: US maps including Alaska and Hawaii, <https://cran.r-project.org/package=usmap>.
- Dickey, D. A. and Fuller, W. A. (1981). Likelihood ratio statistics for autoregressive time series with a unit root, *Econometrica* **49**(4): 1057–1072.
- Diebold, F. X. and Inoue, A. (2001). Long memory and regime switching, *Journal of Econometrics* **105**(1): 131–159.
- Dissanayake, P., Brown, J., Wisse, P. and Karunaratna, H. (2015). Effects of storm clustering on beach/dune evolution, *Marine Geology* **370**: 63–75.
- Distaso, W. (2008). Testing for unit root processes in random coefficient autoregressive models, *Journal of Econometrics* **142**: 581–609.
- Dore, M. H. (2005). Climate change and changes in global precipitation patterns: What do we know?, *Environment International* **31**(8): 1167–1181.

- Dupuis, D. J. and Trapin, L. (2023). Mixed-frequency extreme value regression: Estimating the effect of mesoscale convective systems on extreme rainfall intensity, *Annals of Applied Statistics* **17**(2): 1398–1418.
- Eagleson, P. S. (1994). The evolution of modern hydrology (from watershed to continent in 30 years), *Advances in Water Resources* **17**(1-2): 3–18.
- Edelbuettel, D. (2020). anytime: Anything to ‘POSIXct’ or ‘Date’ converter, <https://cran.r-project.org/package=anytime>.
- Efstathiou, M. N. and Varotsos, C. A. (2012). Intrinsic properties of Sahel precipitation anomalies and rainfall, *Theoretical and Applied Climatology* **109**(3-4): 627–633.
- Engel, C. and Hamilton, J. D. (1990). Long swings in the dollar: Are they in the data and do markets know it?, *American Economic Review* **80**: 689–713.
- EPA (2022). United States Environmental Protection Agency. Climate change indicators: U.S. and global precipitation, retrieved April 4, 2023, from <https://www.epa.gov/climate-indicators/climate-change-indicators-us-and-global-precipitation>.
- Farhi, E. and Gabaix, X. (2016). Rare disasters and exchange rates, *The Quarterly Journal of Economics* **131**(1): 1–52.
- Fatichi, S., Ivanov, V. Y. and Caporali, E. (2012). Investigating interannual variability of precipitation at the global scale: Is there a connection with seasonality?, *Journal of Climate* **25**(16): 5512–5523.
- Fraunhofer ISE (2021). *Levelized Cost of Electricity – Renewable Energy Technologies*, Kost, C., Shammugam, S., Fluri, V., Peper, D., Memar, A.D., Schlegl, T. (eds). Fraunhofer-Institut für Solare Energiesysteme ISE. <https://www.ise.fraunhofer.de/en/publications/studies/cost-of-electricity.html>.
- Garnier, S., Noam, R., Rudis, B., Sciaini, M., Camargo, A. and Scherer, C. (2021). viridis: Colorblind-friendly color maps for R, <https://sjmgarnier.github.io/viridis/>.
- Gehne, M., Hamill, T. M., Kiladis, G. N. and Trenberth, K. E. (2016). Comparison of global precipitation estimates across a range of temporal and spatial scales, *Journal of Climate* **29**(21): 7773–7795.
- Gil-Alana, L. A. (2012). UK rainfall data: A long-term persistence approach, *Journal of Applied Meteorology and Climatology* **51**(10): 1904–1913.
- Gil-Alana, L. A. (2017). Alternative modelling approaches for the ENSO time series: Persistence and seasonality, *International Journal of Climatology* **37**(5): 2354–2363.
- Gil-Alana, L. A., Cunado, J. and Gupta, R. (2017). Persistence, mean-reversion and nonlinearities in CO2 emissions: Evidence from the BRICS and G7 countries, *Environmental and Resource Economics* **67**(4): 869–883.
- Gil-Alana, L. A., Gupta, R., Sauci, L. and Carmona-González, N. (2022). Temperature and precipitation in the US states: Long memory, persistence, and time trend, *Theoretical and Applied Climatology* **150**(3): 1731–1744.

- Gil-Alana, L. A., Yaya, O. S. and Fagbamigbe, A. F. (2019). Time series analysis of quarterly rainfall and temperature (1900-2012) in sub-Saharan African countries, *Theoretical and Applied Climatology* **137**(1-2): 61–76.
- Granger, C. W. J. and Joyeux, R. (1980). An introduction to long-memory time series models and fractional differencing, *Journal of Time Series Analysis* **1**(1): 15–29.
- Graves, T., Gramacy, R., Watkins, N. and Franzke, C. (2017). A brief history of long memory: Hurst, Mandelbrot and the road to ARFIMA, 1951–1980, *Entropy* **19**(9): 437.
- Greene, W. H. (2012). *Econometric Analysis*, Seventh Edition, Pearson Education, England.
- Grolemund, G. and Wickham, H. (2011). Dates and times made easy with lubridate, *Journal of Statistical Software* **40**(3): 1–25.
- Guidolin, M. and Guseo, R. (2016). The German energy transition: Modeling competition and substitution between nuclear power and renewable energy technologies, *Renewable and Sustainable Energy Reviews* **60**: 1498–1504.
- Haan, C., Allen, D. and Street, J. (1976). A Markov chain model of daily rainfall, *Water Resources Research* **12**(3): 443–449.
- Halkos, G. E. and Gkampoura, E.-C. (2020). Reviewing usage, potentials, and limitations of renewable energy sources, *Energies* **13**(11): 2906.
- Hall, P., Li, Q. and Racine, J. S. (2007). Nonparametric estimation of regression functions in the presence of irrelevant regressors, *The Review of Economics and Statistics* **89**(4): 784–789.
- Hansen, K., Mathiesen, B. V. and Skov, I. R. (2019). Full energy system transition towards 100% renewable energy in germany in 2050, *Renewable and Sustainable Energy Reviews* **102**: 1–13.
- Hartl, T. and Jucknewitz, R. (2022). Approximate state space modelling of unobserved fractional components, *Econometric Reviews* **41**(1): 75–98.
- Hastie, T. J. (1990). Generalized additive models, in J. M. Chambers and T. J. Hastie (eds), *Statistical Models in S*, Chapman & Hall.
- Hayfield, T. and Racine, J. S. (2008). Nonparametric econometrics: The np package, *Journal of Statistical Software* **27**(5).
- Hees, K., Nayak, S. and Straka, P. (2021). Statistical inference for inter-arrival times of extreme events in bursty time series, *Computational Statistics & Data Analysis* **155**: 107096.
- Henderson, D. J. and Parmeter, C. F. (2015). *Applied Nonparametric Econometrics*, Cambridge University Press, New York.
- Henry, M. (2001). Robust automatic bandwidth for long memory, *Journal of Time Series Analysis* **22**(3): 293–316.
- Hijmans, R. J., Bivand, R., Pebesma, E. and Sumner, M. D. (2023). terra: Spatial data analysis, <https://cran.r-project.org/package=terra>.

- Hijmans, R. J. et al. (2023). raster: Geographic data analysis and modeling, <https://cran.r-project.org/package=raster>.
- Hillebrand, E., Pretis, F., Proietti, T. et al. (2020). Econometric models of climate change: Introduction by the guest editors, *Journal of Econometrics* **214**(1): 1–5.
- Hosking, J. R. M. (1981). Fractional differencing, *Biometrika* **68**(1): 165–176.
- Hou, J. and Perron, P. (2014). Modified local Whittle estimator for long memory processes in the presence of low frequency (and other) contaminations, *Journal of Econometrics* **182**(2): 309–328.
- Hsiao, C., Li, Q. and Racine, J. S. (2007). A consistent model specification test with mixed discrete and continuous data, *Journal of Econometrics* **140**(2): 802–826.
- Hualde, J. and Nielsen, M. Ø. (2022). Fractional integration and cointegration. Unpublished Manuscript.
- Hurst, H. E. (1956). The problem of long-term storage in reservoirs, *Hydrological Sciences Journal* **1**(3): 13–27.
- Hurst, H. E. (1957). A suggested statistical model of some time series which occur in nature, *Nature* **180**: 494–494.
- Iacone, F., Leybourne, S. J. and Robert Taylor, A. (2014). A fixed-b test for a break in level at an unknown time under fractional integration, *Journal of Time Series Analysis* **35**(1): 40–54.
- Illiopoulou, T., Papalexiou, S. M., Markonis, Y. and Koutsoyiannis, D. (2018). Revisiting long-range dependence in annual precipitation, *Journal of Hydrology* **556**(10): 891–900.
- IPCC (2013). *Climate Change 2013: The Physical Science Basis. Contribution of Working Group I to the Fifth Assessment Report of the Intergovernmental Panel on Climate Change*, Stocker, T. F., Qin, D., Plattner, G.-K., Tignor, M., Allen, S. K., Boschung, J., Nauels, A., Xia, Y., Bex, V., Midgley, P. M. (eds). Cambridge University Press. <https://www.ipcc.ch/report/ar5/wg1/>.
- IPCC (2021). *Climate Change 2021: The Physical Science Basis. Contribution of Working Group I to the Sixth Assessment Report of the Intergovernmental Panel on Climate Change*, Masson-Delmotte, V., Zhai, P., Pirani, A., Connors, S. L., Péan, C., Berger, S., Caud, N., Chen, Y., Goldfarb, L., Gomis, M. I., Huang, M., Leitzell, K., Lonnoy, E., Matthews, J. B. R., Maycock, T. K., Waterfield, T., Yelekçi, O., Yu, R., Zhou, B. (eds). Cambridge University Press. <https://www.ipcc.ch/report/ar6/wg1>.
- IPCC (2023). *AR6 Synthesis Report: Climate Change 2023*, Arias, P., Bustamante, M., Elgizouli, I., Flato, G., Howden, M., Méndez, C., Pereira, J., Pichs-Madruga, R., Rose, S.K., Saheb, Y., Sánchez, R., Ürge-Vorsatz, D., Xiao, C.m Yassaa, N. (eds). Cambridge University Press. <https://www.ipcc.ch/report/ar6/syr/>.
- IRENA (2015). *From Baseload to Peak: Renewables Provide a Reliable Solution*, Ueckerdt, F and Kempener, R (eds). International Renewable Energy Agency. <https://www.irena.org/publications/2015/Jun/From-Baseload-to-Peak-Renewables-provide-a-reliable-solution>.

- James, G., Witten, D., Hastie, T. and Tibshirani, R. (2013). *An Introduction to Statistical Learning with Applications in R*, Springer New York.
- Kahle, D. and Wickham, H. (2013). ggmap: Spatial visualization with ggplot2, *The R Journal* **5**(1): 144–161.
- Kleiber, W., Raftery, A. E. and Gneiting, T. (2011). Geostatistical model averaging for locally calibrated probabilistic quantitative precipitation forecasting, *Journal of the American Statistical Association* **106**(496): 1291–1303.
- Klemeš, V. (1974). The hurst phenomenon: A puzzle?, *Water Resources Research* **10**(4): 675–688.
- Knaus, J. (2013). snowfall: Easier cluster computing (based on ‘snow’), <https://cran.r-project.org/package=snowfall>.
- Köppen, W. (1884). Die Wärmezonen der Erde, nach der Dauer der heissen, gemässigten und kalten Zeit und nach der Wirkung der Wärme auf die organische Welt betrachtet, *Meteorologische Zeitschrift* **1**(21): 5–226.
- Köppen, W. (1900a). Versuch einer Klassifikation der Klimate, vorzugsweise nach ihren Beziehungen zur Pflanzenwelt, *Geographische Zeitschrift* **6**(11): 593–611.
- Köppen, W. (1900b). Versuch einer Klassifikation der Klimate, vorzugsweise nach ihren Beziehungen zur Pflanzenwelt. (Schluss), *Geographische Zeitschrift* **6**(12): 657–679.
- Köppen, W. (1918). Klassifikation der Klima nach Temperatur, Niederschlag und Jahreslauf, *Petermanns Geographische Mitteilungen* **64**: 243–248.
- Köppen, W. (1936). *Das geographische System der Klimate: Mit 14 Textfiguren*, Handbuch der Klimatologie in fünf Bänden, Borntraeger, Berlin.
- Kottek, M., Grieser, J., Beck, C., Rudolf, B. and Rubel, F. (2006). World map of the Köppen-Geiger climate classification updated, *Meteorologische Zeitschrift* **15**(3): 259–263.
- Kotz, M., Levermann, A. and Wenz, L. (2022). The effect of rainfall changes on economic production, *Nature* **601**: 223–227.
- Koutsoyiannis, D. (2000). A generalized mathematical framework for stochastic simulation and forecast of hydrologic time series, *Water Resources Research* **36**(6): 1519–1533.
- Koutsoyiannis, D. (2003). Climate change, the Hurst phenomenon, and hydrological statistics, *Hydrological Sciences Journal* **48**(1): 3–24.
- Künsch, H. R. (1987). Statistical aspects of self-similar processes, in Y. A. Prohorov and V. V. Sazonov (eds), *Probability Theory and Applications*, Vol. 1 of *Proceedings of the 1st World Congress of the Bernoulli Society*, VNU Science Press, Utrecht.
- Kwiatkowski, D., Phillips, P. C., Schmidt, P. and Shin, Y. (1992). Testing the null hypothesis of stationarity against the alternative of a unit root: How sure are we that economic time series have a unit root?, *Journal of Econometrics* **54**(1-3): 159–178.

- Le Cam, L. (1961). A stochastic description of precipitation, in J. Neyman (ed.), *Proceedings of the Fourth Berkeley Symposium on Mathematical Statistics and Probability*, Vol. 3, University of California Press, Berkeley.
- Leschinski, C., Voges, M. and Sibbertsen, P. (2021). A comparison of semiparametric tests for fractional cointegration, *Statistical Papers* **62**: 1997–2030.
- Leschinski, C., Voges, M. and Wenger, K. (2019). LongMemoryTS: Long memory time series, <https://cran.r-project.org/package=LongMemoryTS>.
- Li, Q. and Racine, J. S. (2007). *Nonparametric Econometrics: Theory and Practice*, Princeton University Press.
- Liu, S. C., Fu, C., Shiu, C.-J., Chen, J.-P. and Wu, F. (2009). Temperature dependence of global precipitation extremes, *Geophysical Research Letters* **36**(17).
- Liu, Y., Zhao, Q., Yao, W., Ma, X., Yao, Y. and Liu, L. (2019). Short-term rainfall forecast model based on the improved BP-NN algorithm, *Scientific Reports* **9**: 19751.
- Longobardi, A. and Villani, P. (2010). Trend analysis of annual and seasonal rainfall time series in the Mediterranean area, *International Journal of Climatology* **30**(10): 1538–1546.
- Mandelbrot, B. B. and Wallis, J. R. (1968). Noah, Joseph, and Operational Hydrology, *Water Resources Research* **4**(5): 909–918.
- Manne, A. S., Richels, R. G. and Edmonds, J. A. (2005). Market exchange rates or purchasing power parity: Does the choice make a difference to the climate debate?, *Climatic Change* **71**(1-2): 1–8.
- Marinucci, D. and Robinson, P. M. (1999). Alternative forms of fractional Brownian motion, *Journal of Statistical Planning and Inference* **80**(1-2): 111–122.
- Markonis, Y. and Koutsoyiannis, D. (2016). Scale-dependence of persistence in precipitation records, *Nature Climate Change* **6**(4): 399–401.
- McNeil, A. J., Frey, R. and Embrechts, P. (2015). *Quantitative Risk Management: Concepts, Techniques and Tools*, Revised Edition, Princeton University Press.
- Menne, M. J., Durre, I., Korzeniewski, B., McNeal, S., Thomas, K., Yin, X., Anthony, S., Ray, R., Vose, R. S., Gleason, B. E. and Houston, T. G. (2020). Global Historical Climatology Network - Daily, Version 3.26, <https://doi.org/10.7289/V5D21VHZ>.
- Menne, M. J., Durre, I., Vose, R. S., Gleason, B. E. and Houston, T. G. (2012). An overview of the Global Historical Climatology Network-Daily database, *Journal of Atmospheric and Oceanic Technology* **29**(7): 897–910.
- Naegler, T., Sutardio, C., Weidlich, A. and Pregger, T. (2021). Exploring long-term strategies for the German energy transition – A review of multi-sector energy scenarios, *Renewable and Sustainable Energy Transition* **1**: 100010.
- Netztransparenz.de (2020). Bericht der Deutschen Übertragungsnetzbetreiber gem. § 34 (1) KVBG, <https://www.netztransparenz.de/Weitere-Veroeffentlichungen/Studie-zum-Kohleausstieg>.

- Nicholls, R. J., Wong, P. P., Burkett, V., Codignotto, J., Hay, J., McLean, R., Ragoonaden, S. and Woodroffe, C. (2007). Coastal systems and low-lying areas, *Climate Change 2007: Impacts, Adaptation and Vulnerability. Contribution of Working Group II to the Fourth Assessment Report of the Intergovernmental Panel on Climate Change*, Cambridge University Press.
- O'Connell, P., Koutsoyiannis, D., Lins, H., Markonis, Y., Montanari, A. and Cohn, T. (2016). The scientific legacy of Harold Edwin Hurst (1880-1978), *Hydrological Sciences Journal* **61**(9): 1571–1590.
- O'Connell, P., O'Donnell, G. and Koutsoyiannis, D. (2022). The spatial scale dependence of the Hurst coefficient in global annual precipitation data, and its role in characterising regional precipitation deficits within a naturally changing climate, *Hydrology* **9**(11): 199.
- Paraschiv, F., Erni, D. and Pietsch, R. (2014). The impact of renewable energies on EEX day-ahead electricity prices, *Energy Policy* **73**: 196–210.
- Paul, R. K., Mitra, D., Paul, A. and Bhar, L. (2019). Long memory and structural break in seasonal rainfall in India, *Special Proceeding of the 21st Annual Conference of SSCA held at SV Agricultural College (ANGRAU)*, pp. 83–92.
- Pebesma, E. J. and Bivand, R. S. (2005). Classes and methods for spatial data in R, *R News* **5**(2): 9–13.
- Pegels, A. and Lütkenhorst, W. (2014). Is Germany's energy transition a case of successful green industrial policy? Contrasting wind and solar PV, *Energy Policy* **74**: 522–534.
- Phillips, P. C. and Shimotsu, K. (2004). Local Whittle estimation in nonstationary and unit root cases, *The Annals of Statistics* **32**(2): 656–692.
- Pickands, J. (1975). Statistical inference using extreme order statistics, *The Annals of Statistics* **3**(1).
- Polson, D., Hegerl, G. C., Zhang, X. and Osborn, T. J. (2013). Causes of robust seasonal land precipitation changes, *Journal of Climate* **26**(17): 6679–6697.
- Potter, K. W. (1979). Annual precipitation in the northeast United States: Long memory, short memory, or no memory?, *Water Resources Research* **15**(2): 340–346.
- Poveda, G. (2011). Mixed memory, (non) Hurst effect, and maximum entropy of rainfall in the tropical Andes, *Advances in Water Resources* **34**(2): 243–256.
- Proietti, T. and Maddanu, F. (2022). Modelling cycles in climate series: The fractional sinusoidal waveform process, *Journal of Econometrics* (in press).
- Qu, Z. (2011). A test against spurious long memory, *Journal of Business & Economic Statistics* **29**(3): 423–438.
- R Core Team (2022). R: A language and environment for statistical computing, R Foundation for Statistical Computing, Vienna. <http://www.R-project.org/>.
- Racine, J. S. (1997). Consistent specification testing for nonparametric regression, *Journal of Business & Economic Statistics* **15**(3): 369–378.

- Racine, J. S. (2019). *An Introduction to the Advanced Theory and Practice of Nonparametric Econometrics: A Replicable Approach Using R*, Cambridge University Press.
- Racine, J. S., Hart, J. and Li, Q. (2006). Testing the significance of categorical predictor variables in nonparametric regression models, *Econometric Reviews* **25**(4): 523–544.
- Racine, J. S. and Li, Q. (2004). Nonparametric estimation of regression functions with both categorical and continuous data, *Journal of Econometrics* **119**: 99–130.
- Ramirez-Meyers, K., Mann, W. N., Deetjen, T. A., Johnson, S. C., Rhodes, J. D. and Webber, M. E. (2021). How different power plant types contribute to electric grid reliability, resilience, and vulnerability: A comparative analytical framework, *Progress in Energy* **3**(3): 033001.
- Rao, A. R. and Bhattacharya, D. (1999). Hypothesis testing for long-term memory in hydrologic series, *Journal of Hydrology* **216**(3-4): 183–196.
- Richards, J., Tawn, J. A. and Brown, S. (2022). Modelling extremes of spatial aggregates of precipitation using conditional methods, *The Annals of Applied Statistics* **16**(4): 2693–2713.
- Rocheta, E., Sugiyanto, M., Johnson, F., Evans, J. and Sharma, A. (2014). How well do general circulation models represent low-frequency rainfall variability?, *Water Resources Research* **50**(3): 2108–2123.
- Sánchez-Murillo, R., Durán-Quesada, A. M., Birkel, C., Esquivel-Hernández, G. and Boll, J. (2017). Tropical precipitation anomalies and d-excess evolution during El Niño 2014–16, *Hydrological Processes* **31**(4): 956–967.
- Sansó, B. and Guenni, L. (2000). A nonstationary multisite model for rainfall, *Journal of the American Statistical Association* **95**(452): 1089–1100.
- Schlosser, L., Hothorn, T., Stauffer, R. and Zeileis, A. (2019). Distributional regression forests for probabilistic precipitation forecasting in complex terrain, *The Annals of Applied Statistics* **13**(3): 1564–1589.
- Serinaldi, F., Kilsby, C. G. and Lombardo, F. (2018). Untenable nonstationarity: An assessment of the fitness for purpose of trend tests in hydrology, *Advances in Water Resources* **111**: 132–155.
- Shao, X. (2011). A simple test of changes in mean in the possible presence of long-range dependence, *Journal of Time Series Analysis* **32**(6): 598–606.
- Shao, X. and Wu, W. B. (2007). Local Whittle estimation of fractional integration for nonlinear processes, *Econometric Theory* **23**(5): 899–929.
- SMARD.de (2023). Bundesnetzagentur für Elektrizität, Gas, Telekommunikation, Post und Eisenbahnen, retrieved March 13, 2023, from <https://www.smard.de/home>.
- South, A. (2011). rworldmap: A new R package for mapping global data, *The R Journal* **3**(1): 35–43.

- Souza, I. V. M., Reisen, V. A., Franco, G. d. C. and Bondon, P. (2018). The estimation and testing of the cointegration order based on the frequency domain, *Journal of Business & Economic Statistics* **36**(4): 695–704.
- Sun, Q., Miao, C., Duan, Q., Ashouri, H., Sorooshian, S. and Hsu, K.-L. (2018). A review of global precipitation data sets: Data sources, estimation, and intercomparisons, *Reviews of Geophysics* **56**(1): 79–107.
- Sutcliffe, J., Hurst, S., Awadallah, A. G., Brown, E. and Hamed, K. (2016). Harold Edwin Hurst: The Nile and Egypt, past and future, *Hydrological Sciences Journal* **61**(9): 1557–1570.
- Tapiador, F. J. (2010). A joint estimate of the precipitation climate signal in Europe using eight regional models and five observational datasets, *Journal of Climate* **23**(7): 1719–1738.
- Tapiador, F. J., Turk, F. J., Petersen, W., Hou, A. Y., García-Ortega, E., Machado, L. A., Angelis, C. F., Salio, P., Kidd, C., Huffman, G. J. et al. (2012). Global precipitation measurement: Methods, datasets and applications, *Atmospheric Research* **104**: 70–97.
- Teräsvirta, T. (1994). Specification, estimation, and evaluation of smooth transition autoregressive models, *Journal of the American Statistical Association* **89**: 208–218.
- Tyralis, H., Dimitriadis, P., Koutsoyiannis, D., O’Connell, P. E., Tzouka, K. and Iliopoulou, T. (2018). On the long-range dependence properties of annual precipitation using a global network of instrumental measurements, *Advances in Water Resources* **111**: 301–318.
- UBA (2021). Umweltbundesamt. Erneuerbare-Energien-Gesetz, retrieved June 11, 2023, from <https://www.umweltbundesamt.de/themen/klima-energie/erneuerbare-energien/erneuerbare-energien-gesetz#erfolg>.
- UBA (2023a). Umweltbundesamt. Erneuerbare Energien in Zahlen, retrieved June 11, 2023, from <https://www.umweltbundesamt.de/themen/klima-energie/erneuerbare-energien/erneuerbare-energien-in-zahlen#uberblick>.
- UBA (2023b). Umweltbundesamt. Treibhausgas-minderungsziele Deutschlands, retrieved June 11, 2023, from <https://www.umweltbundesamt.de/daten/klima/treibhausgas-minderungsziele-deutschlands#internationale-vereinbarungen-weisen-den-weg>.
- Ubilava, D. and Helmers, C. G. (2013). Forecasting ENSO with a smooth transition autoregressive model, *Environmental Modelling & Software* **40**: 181–190.
- UN (2023a). United Nations. What is climate change?, retrieved May 29, 2023, from <https://www.un.org/en/climatechange/what-is-climate-change>.
- UN (2023b). United Nations. What is renewable energy?, retrieved June 1, 2023, from <https://www.un.org/en/climatechange/what-is-renewable-energy>.
- van Dijk, D., Teräsvirta, T. and Franses, P. H. (2002). Smooth transition autoregressive models – A survey of recent developments, *Econometric Reviews* **21**: 1–47.

- Vanem, E. and Walker, S.-E. (2013). Identifying trends in the ocean wave climate by time series analyses of significant wave height data, *Ocean Engineering* **61**: 148–160.
- Veenstra, J. Q. and McLeod, A. I. (2015). arfima: Fractional ARIMA (and other long memory) time series modeling, <https://cran.r-project.org/package=arfima>.
- Velasco, C. (1999). Gaussian semiparametric estimation of non-stationary time series, *Journal of Time Series Analysis* **20**(1): 87–127.
- Wenger, K., Leschinski, C. and Sibbertsen, P. (2019). Change-in-mean tests in long-memory time series: A review of recent developments, *AStA Advances in Statistical Analysis* **103**(2): 237–256.
- Werner, R., Valev, D., Danov, D. and Guineva, V. (2015). Study of structural break points in global and hemispheric temperature series by piecewise regression, *Advances in Space Research* **56**(11): 2323–2334.
- Wickham, H. (2016). *ggplot2: Elegant Graphics for Data Analysis*, Second Edition, Springer.
- Wickham, H., François, R., Henry, L., Müller, K. and Vaughan, D. (2017). dplyr: A grammar of data manipulation, <https://cran.r-project.org/package=dplyr>.
- Wood, S. N. (2017). *Generalized Additive Models: An Introduction with R*, Second Edition, CRC Press.
- Yajima, Y. (1988). On estimation of a regression model with long-memory stationary errors, *The Annals of Statistics* **16**(2): 791–807.
- Yaya, O. S., Gil-Alana, L. A. and Akomolafe, A. A. (2015). Long memory, seasonality and time trends in the average monthly rainfall in major cities of Nigeria, *CBN Journal of Applied Statistics* **6**(2): 39–58.
- Yuan, N., Huang, Y., Duan, J., Zhu, C., Xoplaki, E. and Luterbacher, J. (2019). On climate prediction: How much can we expect from climate memory?, *Climate Dynamics* **52**: 855–864.
- Yusof, F., Kane, I. L. and Yusop, Z. (2013). Structural break or long memory: An empirical survey on daily rainfall data sets across Malaysia, *Hydrology & Earth System Sciences* **17**(4).
- Zhang, X., Vincent, L. A., Hogg, W. and Niitsoo, A. (2000). Temperature and precipitation trends in Canada during the 20th century, *Atmosphere-Ocean* **38**(3): 395–429.
- Zhang, X., Zwiers, F. W., Hegerl, G. C., Lambert, F. H., Gillett, N. P., Solomon, S., Stott, P. A. and Nozawa, T. (2007). Detection of human influence on twentieth-century precipitation trends, *Nature* **448**: 461–465.